Swirl Recovery Vanes for Propeller Propulsion Systems

An Aerodynamic and Aeroacoustic Investigation by Lattice Boltzmann Method

Luc van den Ende

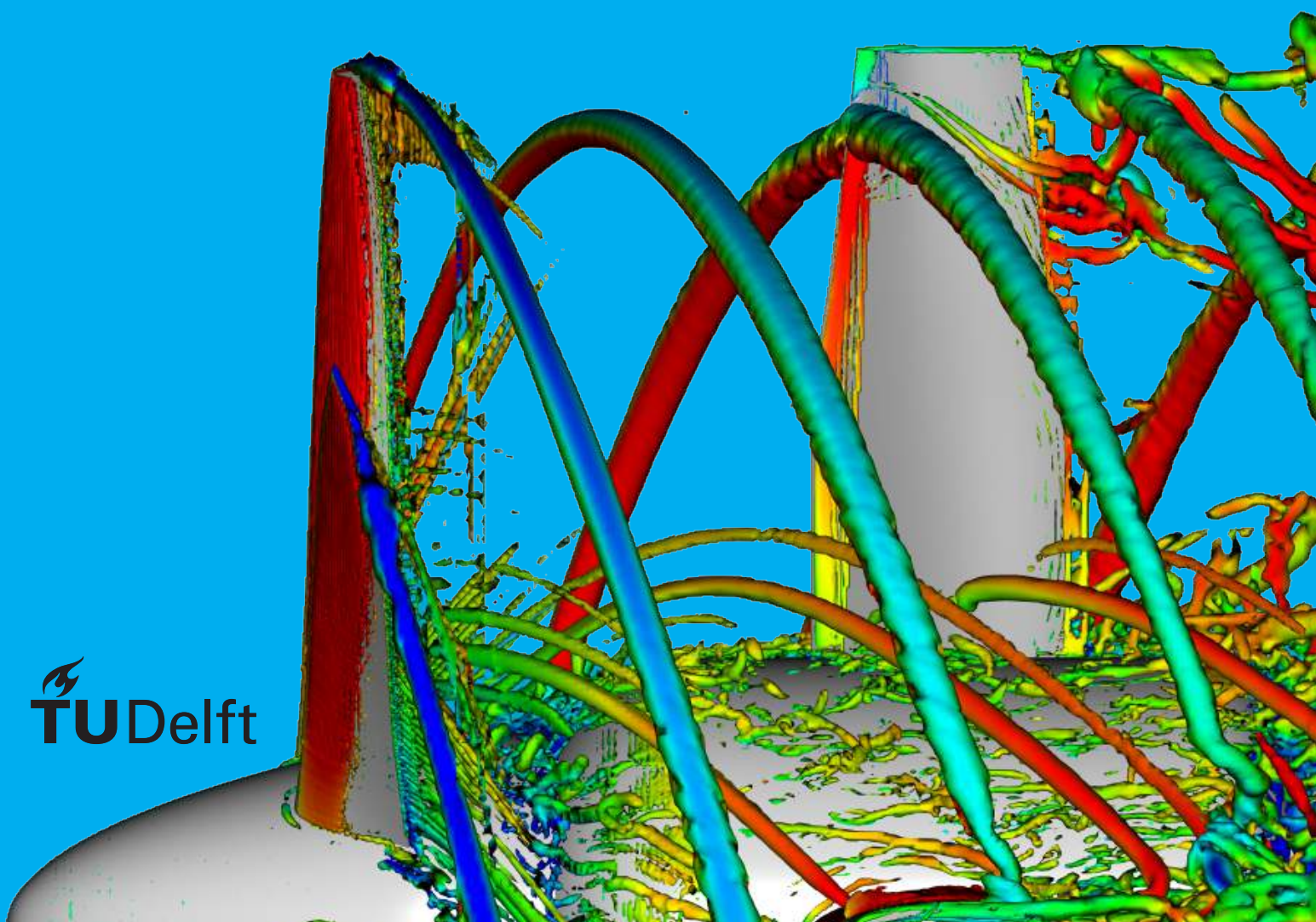

TU Delft

Swirl Recovery Vanes for Propeller Propulsion Systems

An Aerodynamic and Aeroacoustic Investigation by Lattice Boltzmann Method

by

Luc van den Ende

Student number:	4227360	
Project duration:	January, 2018 – October, 2018	
Thesis committee:	Ir. Q. Li,	TU Delft, daily supervisor
	Dr.ir. F. Avallone,	TU Delft, daily supervisor
	Prof.dr.ir. D. Casalino,	TU Delft
	Prof.dr.ir. L.L.M. Veldhuis,	TU Delft, chair

TU Delft

Summary

The high propulsive efficiency of propellers makes them an attractive propulsion system. It has been demonstrated that a properly designed stationary second stage, consisting of swirl recovery vanes (SRVs), can further increase the propulsive efficiency by recovering part of the slipstream swirl. Although the propeller slipstream causes a fluctuating inflow into the SRVs, unsteady effects are neglected in the design process. A better understanding of these unsteady effects could help us improve the design. Furthermore, incongruities are reported in literature about the impact that SRVs have on the far-field noise. The current numerical study is aimed at examining the unsteady aerodynamic and aeroacoustic effects of SRV installation to explore possible improvements to the design.

Propellers generate thrust which accelerates the flow in axial direction. Torque has to be delivered to the propeller which causes the flow to rotate in the direction of propeller rotation. This tangential motion is called swirl with a swirl angle which relates directly to the inflow angle of the SRVs. The SRVs are lifting surfaces on which a resultant force acts with a forward component, or thrust. The inflow is deflected as a consequence such that the swirl in the slipstream is reduced.

A lattice Boltzmann method (LBM) is chosen to be applied in this research. In contrast to conventional aerodynamic solvers based on macroscopic differential equations, LBM is based on the motion of mesoscopic particle distributions. Space and velocity are discretised by means of a lattice and collision, turbulence and wall models are adopted. Due to its time-dependent and compressible nature, assessment of unsteady aerodynamics and the far-field sound is possible using a hybrid method including the Ffowcs Williams-Hawkings equation.

A grid refinement study is performed for several reference variables using four grids with increasing resolution. Validity of the aerodynamic results obtained from LBM is confirmed by comparing to computational and experimental data obtained in previous studies. The aeroacoustics are assessed by qualitatively comparing against literature.

The aerodynamic performance of the SRVs is investigated in detail first. The high swirl angle within the blade wakes and rotor tip vortices (RTVs) is seen to be the cause of a fluctuating thrust production by the SRVs. These two effects impinge successively on the SRVs causing double peaks in the time history of thrust. After the RTVs are split by the SRVs, an opposing spanwise motion occurs on the pressure and suction side of the vane.

In terms of aeroacoustics, the SRVs produce noise at frequencies equal to multiples of the blade passing frequency with a relatively uniform distribution in all directions. This results in the observation that the SRVs have no effect on the maximum noise level, which is located in the plane of the propeller. The SRVs are however a dominant noise source up- and downstream of the propeller for a range of $\Delta\theta = 90^\circ$ upstream and $\Delta\theta = 130^\circ$ downstream. The SRVs cause the sound pressure to increase by up to 20 dB in these regions, noting that low-turbulence axial inflow into the propeller is considered.

The tip region of the vanes is a topic of special interest due to impingement of the RTVs. The average thrust generated by the tip, defined as $r/R > 0.84$, is equal to only 1.9% of the total vane thrust while the tip constitutes to 19% of the surface area of the SRV. Moreover, it is expected in literature that the RTV impingement is a source of noise. It has therefore been decided to simulate a configuration with shortened vanes by removing the vane tips. No decrease in far-field noise is observed for the shorter vanes, while the vane thrust and swirl recovery decreased by 13%. The main cause of this reduced aerodynamic performance is the altered vane loading which is affected by the reduced span, with a stronger stator tip vortex as a result. When taking a combined aerodynamic and aeroacoustic standpoint, it can be concluded that it is detrimental to crop the vanes.

Contents

List of Symbols

B	Number of propeller blades [-]
C	Courant number [-]
c	Chord length [m]
C_D	Drag coefficient [-]
$C(f)$	Fourier transform of the pressure fluctuations [Pa/Hz]
$\vec{c}_i$	Discrete velocity [m/s]
C_L	Lift coefficient [-]
C_P	Power coefficient [-]
C_Q	Torque coefficient [-]
c_r	Propeller root chord [m]
c_s	Speed of sound [m/s]
C_T	Thrust coefficient [-]
D	Propeller diameter [m]
d	Number of spatial dimensions [-]
dD	Drag of one element [N]
dF_R	Resultant force of one element [N]
dL	Lift of one element [N]
dQ	Torque of one element [Nm]
dT	Thrust of one element [N]
f	Frequency [Hz]
F_D	Drag force [N]
f_i	Particle distribution function [-]
F_L	Lift force [N]
f_L	Length scale of the unresolved near-wall region [m]
F_R	Resultant force [N]
I	Turbulence intensity [-]
J	Advance ratio [-]
k	Turbulent kinetic energy [J/kg]
L	Characteristic length [m]
l	Vane length [m]
$\dot{m}$	Mass flow rate through the propeller [kg/s]
n	Rotational speed [rev/s]
n_i	Boolean to indicate the presence of a particle in LGA [-]
N_{rot}	Number of propeller rotations [-]
P	Power [W]
p	Static pressure [Pa]
p'	Pressure fluctuation [Pa]
p_e	Effective sound pressure [Pa]
$P(f)$	Power spectral density [Pa^2/Hz]
Q	Torque [Nm]
R	Propeller radius [m]
r	Local radius [m]
$\overline{R}$	Gas constant [J/(mol·K)]
S	Wing surface area [m^2]
T	Thrust [N]
t	Time [s]
T_K	Temperature [K]
T_s	Duration [s]
$\vec{u}$	Fluid velocity [m/s]
U	Inflow velocity [m/s]
u	Velocity parallel to the wall [m/s]
u'	Root mean square of turbulent velocity fluctuations [m/s]
u^+	Non-dimensional velocity parallel to the wall [-]
u_τ	Friction velocity [m/s]
V_a	Axial velocity [m/s]
V_e	Velocity at an infinite distance downstream [m/s]
V_t	Tangential velocity [m/s]

V_∞	Free-stream velocity [m/s]
w_i	Weights [−]
$\vec{x}$	Location [m]
y	Wall distance [m]
y^+	Non-dimensional wall distance [-]
α	Angle of attack [°]
β	Pitch angle [°]
Δ	Difference operator [-]
ϵ	Turbulent dissipation rate [J/(kg·s)]
ζ	Location [m]
η	Propulsive efficiency [-]
θ	Angle of emitted sound [°]
λ	Wavelength [m]
ν	Kinematic viscosity [m^2/s]
$\vec{\xi}$	Particle velocity [m/s]
ρ	Air density [kg/m^3]
σ	Viscous stress tensor [MPa]
τ	Relaxation time [s]
τ_w	Wall shear stress [MPa]
ϕ	Phase angle [°]
φ	Swirl/Inflow angle [°]
ω	Angular velocity [rad/s]
Ω_i	Collision operator [-]

List of Abbreviations

ATP	Advanced Turboprop Project
BGK	Bhatnagar-Gross-Krook
BPF	Blade passing frequency [Hz]
CFD	Computational fluid dynamics
CFL	Courant-Friedrichs-Lewy
FHP	Frisch-Hasslacher-Pomeau
FW-H	Ffowcs Williams-Hawkings
LBM	Lattice Boltzmann method
LE	Leading edge
LES	Large eddy simulation
LGA	Lattice gas automata
LLT	Lifting line theory
NASA	National Aeronautics and Space Administration
OSPL	Overall sound pressure level [dB]
PBL	Pressure band level [dB]
PGE-WM	Pressure-gradient-extended wall-model
PIV	Particle image velocimetry
PS	Pressure side
PWL	Power watt level [dB/Hz]
RANS	Reynolds-averaged Navier-Stokes
RHS	Right-hand side
RMSE	Root mean square error
RNG	Renormalization group
RTV	Rotor tip vortex
SPL	Sound pressure level [dB]
SRV	Swirl recovery vane
SS	Suction side
STV	Stator tip vortex
TE	Trailing edge
VLES	Very large eddy simulation
VR	Variable resolution

1 Introduction

The National Aeronautics and Space Administration (NASA) started the Aircraft Energy Efficiency Program in 1976 as a response to high fuel prices caused by the Middle East oil embargo [5]. As part of this program, the launch of the Advanced Turboprop Project (ATP) followed in 1978 after initial tests had shown that fuel savings of 15 to 30 percent were attainable by using propellers instead of the turbofans of that time [23]. The idea of using swirl recovery vanes (SRVs) to exploit the swirl energy present in the slipstream of propellers was introduced by Groeneweg & Bober [23]. SRVs are stationary and therefore lighter and cheaper than their rotating counterpart, the contra-rotating open rotor. Full-scale experiments at a Mach number of 0.80 followed in which promising results were attained with a 2% increase in total efficiency at cruise [22]. No additional noise was measured by Dittmar & Hall [18] and even a slight reduction was observed at the optimal vane angle setting as the SRVs unloaded the propeller. Due to decreasing oil prices, the ATP program was ended in 1987 [5].

Decades later, renewed interest in turboprop engines exists for their high propulsive efficiency, causing Delft University of Technology and the Northwestern Polytechnical University to continue the research on SRVs. Wang et al. [53] performed a computational and experimental assessment of SRVs build up of circular arc airfoils. An increase in thrust was measured together with an increase in required propeller power, lowering the total efficiency. The axial distance between propeller and vanes was found to have a small influence on the performance, especially at advance ratios lower than 1. Stokkermans [50] designed SRVs by lifting line theory, which resulted in an increase of experimentally obtained propulsive efficiency of 0.3% at cruise ($J = 1.6$) and 2.8% at high thrust setting ($J = 0.95$). These improvements diminished when including a trailing wing, such that it was recommended to include the wing in the optimisation. Similar improvements in efficiency were attained by Wang et al. [54] by applying a high-fidelity design approach. Experimental studies performed by Sinnige et al. [49] show an increase of total sound pressure of 2 to 6 dB when installing the SRVs, although interaction noise could have been reduced by using a different number of blades for the propeller and the SRVs [32]. An unsteady computational study showed that vanes with a length equal to the propeller blades outperform shorter vanes in terms of aerodynamics [32]. The unsteady effects on the stator are found to be larger than on the rotor such that a good stall margin is required for the SRVs. The present study will build further on work from Li et al. [33] in which SRVs are designed by lifting line theory. Experimental results show an increase of 0.8% in thrust and efficiency for cruise condition and 2.6% at a high loading design condition ($J = 0.6$).

Careful design of the SRVs is required in order to increase the propulsive efficiency [33, 53]. Steady flow is assumed in the low-fidelity design process although the SRVs are exposed to highly turbulent and unsteady inflow [32]. Studying the unsteady effects on the SRVs could result in recommendations for improvements to the design. Besides the benefit of providing extra thrust, the SRVs may also generate additional noise due to the unsteady loading and impingement of propeller tip vortices. Acoustic measurements performed by NASA [18] show no additional noise production by the SRVs. On the other hand, it is observed by Sinnige et al. [49] that the sound pressure level increases by 2 to 6 dB compared to the isolated propeller when the SRVs are installed. Taking into account that both experiments were performed at distinct flow conditions using different geometry, the discrepancy may be clarified by a computational campaign.

Having identified two research areas, it is now possible to formulate a research topic and research questions. The research topic is formulated as follows:

"Aerodynamic and Aeroacoustic Investigation of Swirl Recovery Vanes for Propeller Propulsion System by Lattice Boltzmann Method"

The main research question and accompanying sub-questions are:

- *Are SRVs a feasible option to enhance performance of propeller propulsion systems?*
    1. Is LBM a suitable method to be used in this project?
    2. Do SRVs offer aerodynamic performance benefits?
    3. What improvements to the current configurations in terms of aerodynamic performance can be suggested?
    4. What are the noise effects of SRVs?
    5. Which noise sources can be identified?
    6. What improvements to the current configurations in terms of noise can be suggested?

A lattice Boltzmann method (LBM) coupled with a very large eddy simulation (VLES) turbulence model has been chosen to simulate four geometries. A configuration with SRVs (SRVs ON), designed by Li et al. [33], will be compared to an isolated propeller (SRVs OFF). Subsequently, a configuration with shortened vanes is analysed since it is expected in literature [49] that the impingement of the propeller tip vortices is a source of noise. Moreover, it is observed that the vane tips have a low contribution to the total thrust production. In the Appendix, the first results of a configuration including a wing and SRV are presented. This is of interest as the wing has a large influence on the slipstream swirl [51] and since tractor propeller configurations are common in industry.

The manuscript is organised such that background information is presented first in Chapter 2. Following, the methodology is described in Chapter 3 including the main numerical method and the methods used for validation. The grid refinement study and the validation are included in Chapter 4 before getting to the results in Chapter 5. The main findings of the work are summarised in the final section.

2

Theoretical Background

2.1. Attractiveness of propeller propulsion systems

The main benefit of propellers as thrust-generating devices can be demonstrated by a simple calculation based on momentum theory. The propeller can be modelled as an actuator disk, see Figure 2.1, over which the velocity is assumed to be constant and the pressure uniform. The flow is considered to be incompressible and irrotational and the streamtube is assumed to be well-defined such that the flow through the propeller is separated from the rest of the flow [38].

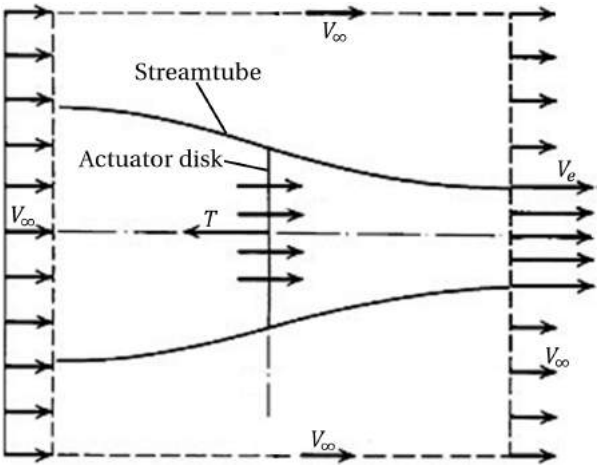

Figure 2.1: Visualisation of the streamtube and actuator disk used in momentum theory. Adapted from [38].

The propulsive efficiency is defined as [17] :

$$\eta = \frac{TV_\infty}{P} \tag{2.1}$$

where T and P are the thrust and power respectively and V_∞ is the free-stream velocity.

The thrust and power can be calculated using the following relations [38]:

$$T = \dot{m}(V_e - V_\infty) \tag{2.2}$$

$$P = \frac{1}{2}\dot{m}(V_e^2 - V_\infty^2) \tag{2.3}$$

where $\dot{m}$ is the mass flow rate through the propeller and V_e is the velocity at an infinite distance downstream.

The propulsive efficiency thus becomes:

$$\eta = \frac{TV_\infty}{P} = \frac{\dot{m}(V_e - V_\infty)V_\infty}{\frac{1}{2}\dot{m}(V_e^2 - V_\infty^2)} = \frac{2(V_e - V_\infty)V_\infty}{(V_e - V_\infty)(V_e + V_\infty)} = \frac{2V_\infty}{(V_e + V_\infty)} = \frac{2}{1 + \frac{V_e}{V_\infty}} \tag{2.4}$$

which indicates that the efficiency increases when the difference between inflow and outflow velocity decreases. This displays the benefit of a propeller over a turbofan or turbojet. Propellers accelerate a larger amount of air to a lesser extent than turbofan or turbojet engines such that the exhaust velocity is decreased.

The reason that turbojet engines, and later turbofan engines, became the new standard in the 1950's was their ability to offer high-speed flight at high altitude with reasonable noise production [40]. The high fuel consumption was acceptable because of the low oil prices. However, advanced turboprop engines can nowadays attain flight at Mach 0.8 at high altitude with a substantial reduction in fuel consumption, see Figure 2.2.

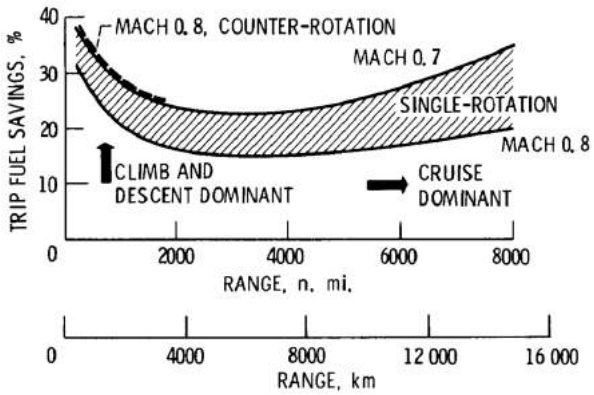

Figure 2.2: Fuel savings trends of advanced turboprop aircraft over comparable turbofan aircraft [40].

2.2. Working principle of a propeller

In order to demonstrate the working principle of a propeller, blade element theory is applied. The propeller blades are divided into elements such that the 3D geometry becomes a summation of non-interacting 2D strips. The cross section of such a 2D element is shown in Figure 2.3, where ω is the angular velocity, r the local radius of the blade element, V_∞ the free-stream velocity and U the inflow velocity. The included angles are defined such that β is the pitch angle, φ the inflow angle and α the angle of attack.

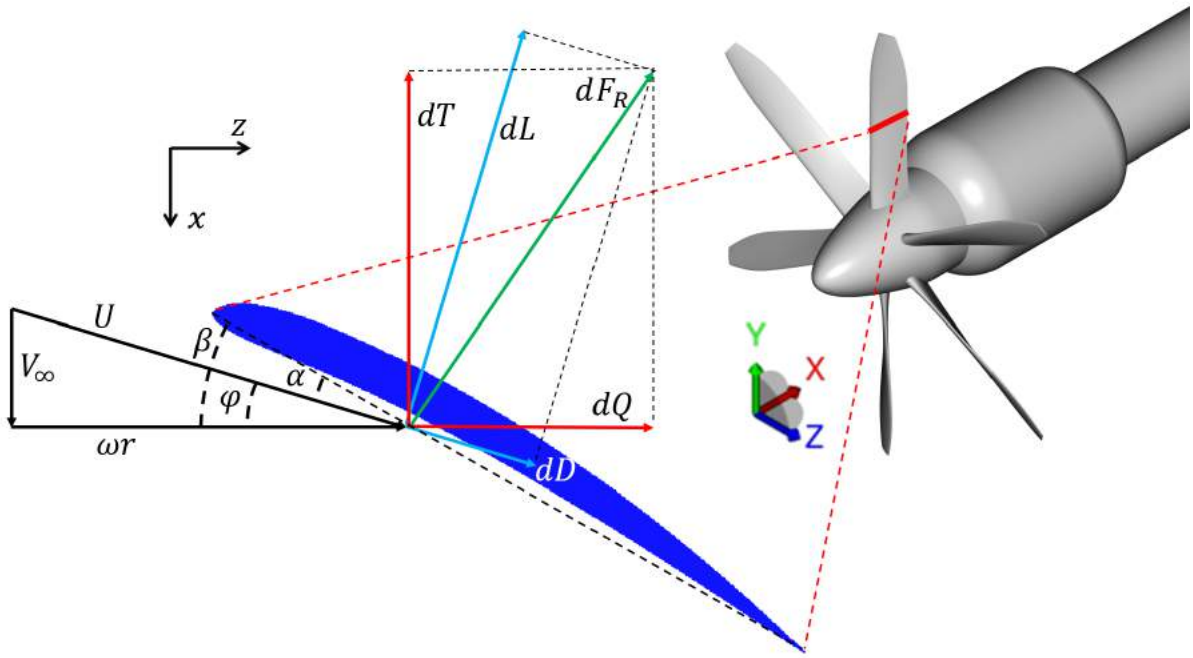

Figure 2.3: Cross section of a propeller blade element including forces and velocities.

The incoming flow U causes a resultant force on the element dF_R which can be decomposed into a component perpendicular and parallel to the inflow, the lift (dL) and drag (dD) force respectively. When the

decomposition is performed into the axial and circumferential direction, a thrust (dT) and torque (dQ) force are formed. These two forces can be calculated from the lift and drag as:

$$dT = dLcos(\varphi) - dDsin(\varphi) \tag{2.5}$$

$$dQ = dLsin(\varphi) + dDcos(\varphi) \tag{2.6}$$

where dL and dD are the lift and drag force acting on one element, respectively.

As the thrust and torque act on the blade, by the third law of Newton, the blade exerts equal but opposite forces on the fluid. The counterpart of the thrust is an accelerating force on the flow, resulting in an increase in axial velocity V_a and a contracting streamtube (Figure 2.1). The counterpart of the torque is a tangential force that causes a tangential velocity V_t or swirl. The wake thus rotates in the same direction as the propeller blades. It is practical to define a swirl angle φ as [10]:

$$\varphi = tan^{-1}\left(\frac{V_t}{V_a}\right) \tag{2.7}$$

2.3. Propeller performance coefficients

Several non-dimensionalised performance coefficients will be used throughout this manuscript, for which the definition used by Brandt & Selig [6] and Li, Wang & Eitelberg [32] is used.

The advance ratio is defined as:

$$J = \frac{V_\infty}{nD} \tag{2.8}$$

where n is the rotational velocity in revolutions per second and D the diameter of the propeller.

The thrust and power coefficients are as follows:

$$C_T = \frac{T}{\rho n^2 D^4} \tag{2.9}$$

$$C_P = \frac{P}{\rho n^3 D^5} \tag{2.10}$$

with ρ the density of the air.

And since $P = 2\pi nQ$:

$$C_Q = \frac{Q}{\rho n^2 D^5} \tag{2.11}$$

such that $C_Q = \frac{C_P}{2\pi}$ where Q is the torque on the propeller.

Finally, the propulsive efficiency can be written as:

$$\eta = \frac{TV_\infty}{P} = \frac{C_T J}{C_P} \tag{2.12}$$

2.4. Swirl recovery by SRVs

Swirl recovery vanes (SRVs) exploit the swirl energy present in the slipstream of propellers in order to produce additional thrust and increase the propulsive efficiency [18, 22, 32, 33, 49, 53, 54]. In Figure 2.4 a typical configuration with propeller and SRVs is shown and a cross section of a SRV is taken. Relevant velocities and forces are included.

As explained, the inflow velocity has a tangential component and therefore a swirling motion with swirl angle φ. This swirl angle relates directly to the inflow angle of the vane, as can be deducted from Figure 2.4. As with any aerodynamic surface, the incoming velocity generates a resultant force dF_R, presented in green. This force can be decomposed in a force perpendicular and parallel to the incoming velocity, being the lift (dL) and drag (dD) on the element, respectively. Another possible decomposition is in axial and tangential direction, resulting in the thrust (dT) and torque (dQ) force respectively. An optimal vane produces maximum thrust which results in maximising the lift and minimising the drag component of the resultant force, as is demonstrated by the following equation:

$$dT = dLsin(\varphi) - dDcos(\varphi) \tag{2.13}$$

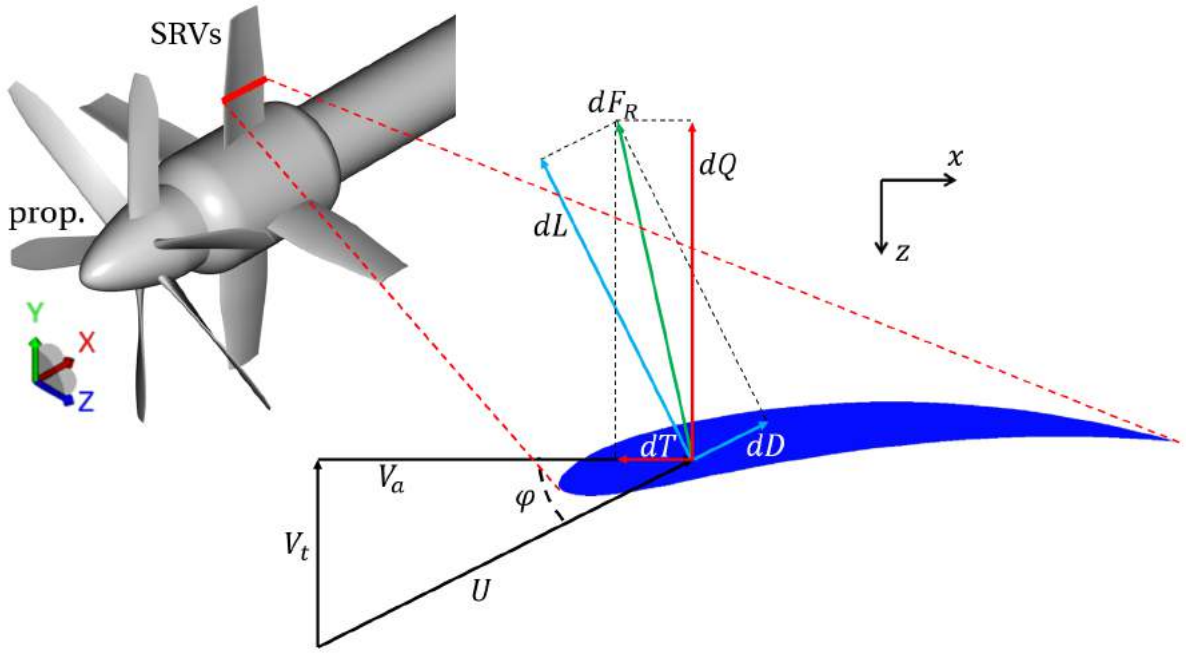

Figure 2.4: Cross section of a swirl recovery vane element including forces and velocities.

2.5. Unsteady effects in the propeller slipstream

Up to this point, the unsteadiness in the propeller slipstream has not been discussed. The slipstream is however seen to be highly periodic due to the presence of a finite number of propeller blades. Experimental data quantifying the propeller slipstream has been gathered by Roosenboom, Heider & Schröder [46]. The velocity magnitude is presented in Figure 2.5, which shows a small periodic variation in axial direction. This is caused by the relatively low velocity in the wakes trailing the propeller blades.

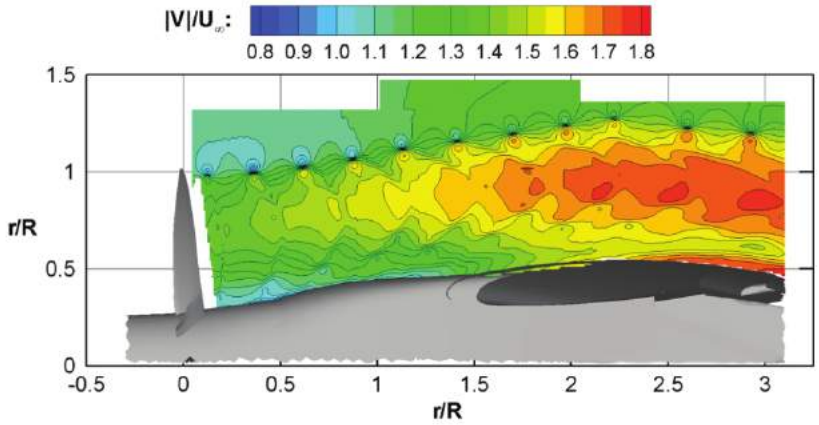

Figure 2.5: Instantaneous velocity magnitude in the wake of a propeller with a trailing wing. $C_T = 0.1$ and $\alpha = \alpha_{cruise}$ [46].

Vortices originate at the tip of propeller blades by the pressure difference between the pressure and suction side of the blade. These rotor tip vortices (RTVs) move downstream on the edge of the slipstream and are visible as blue circles in Figure 2.6 where the vorticity around the out-of-plane axis is plotted. As a consequence of the blade loading distribution, trailing vortices originate at the blade trailing edges [14]. These form regions of high vorticity with the vortices at the outboard region rotating in opposite direction as the ones at the inboard region. Additionally, the deformation of these regions shows the slipstream to have a higher axial velocity in the middle region compared to the in- and outboard regions.

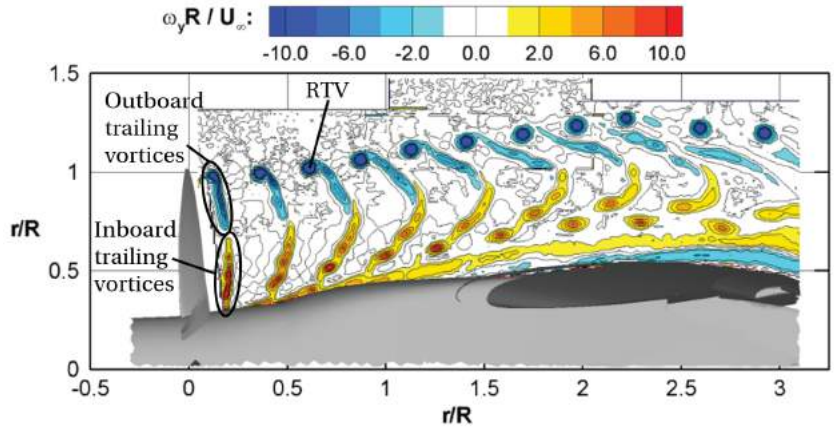

Figure 2.6: Instantaneous out-of-plane vorticity in the wake of a propeller with a trailing wing. PIV data at $C_T = 0.1$ and $\alpha = \alpha_{cruise}$. Adapted from [46].

2.6. Unsteady effects due to SRVs installation

As the propeller slipstream is seen to be unsteady, the SRVs will experience an unsteady inflow. Li et al. [32] performed a computational fluid dynamics (CFD) investigation into the unsteady interaction between a propeller and SRVs. Various vane lengths were inspected from which it was concluded that the vane length has a negligible effect on the propeller slipstream shape upstream of the vanes. Three effects have been identified. Firstly, the upstream potential effect of the SRVs on the propeller is seen to be relatively small, in agreement with observations made by Celik & Güner [11]. Together with unsteadiness, the upstream effect causes variations in propeller thrust of 0.55% with respect to the averaged value, see Figure 2.7 [32].

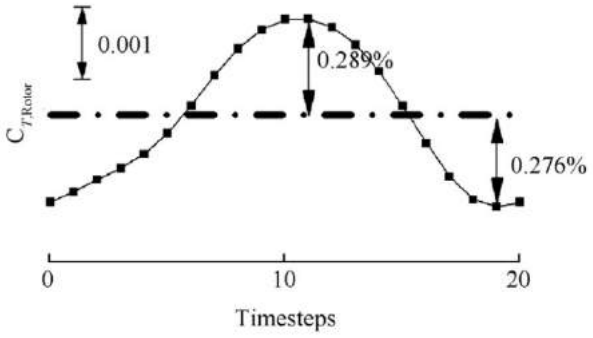

Figure 2.7: Variation of thrust coefficient of the propeller during one propeller blade passing period [32].

Secondly, as stated before, the wake effect behind the propeller results in a varying dynamic pressure behind the blade. This is displayed in Figure 2.8 in which the dynamic pressure is plotted for half of the circumferential for four time instants at three locations: in front of the propeller, in between the propeller and the SRVs and aft of the SRVs. At the location between propeller and the SRVs, two distinct effects can be observed. The narrow drops are caused by the velocity deficits in the wakes of the propeller blades, which are connected for the various time steps to form the "rotor wake". This causes a varying thrust generated by a SRV as shown in Figure 2.9, with larger variations in thrust than for the propeller in Figure 2.7. The upstream effect of the stationary vanes is marked by "vane blockage" and can be explained in potential flow theory by the notion of induced velocity. The upstream potential disturbances of the propeller blades are rotating which causes the peaks in dynamic pressure to move with time. The static wakes behind the vanes are also visible in Figure 2.8.

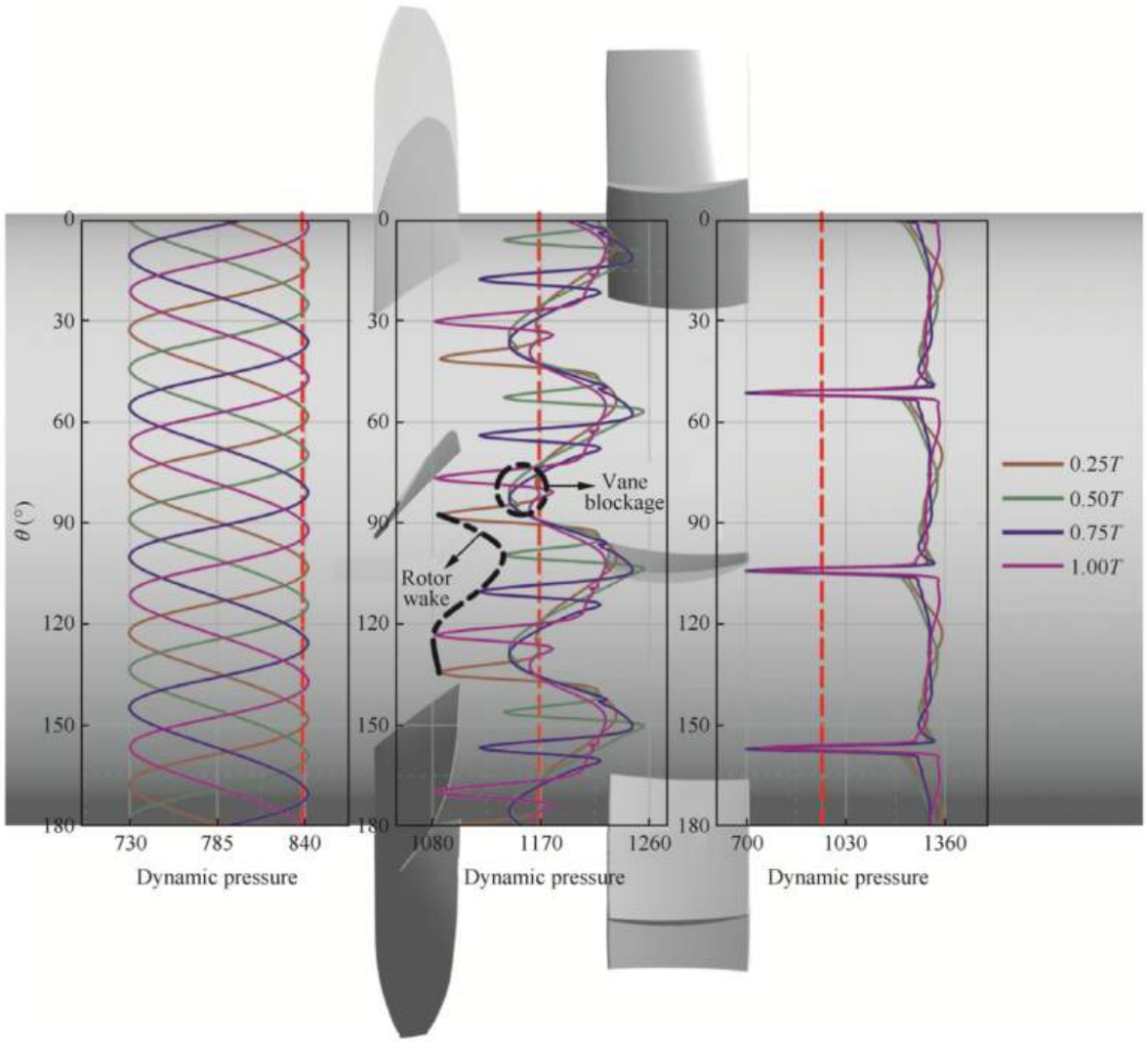

Figure 2.8: Variation of dynamic pressure at three locations indicated by red dashed lines [32].

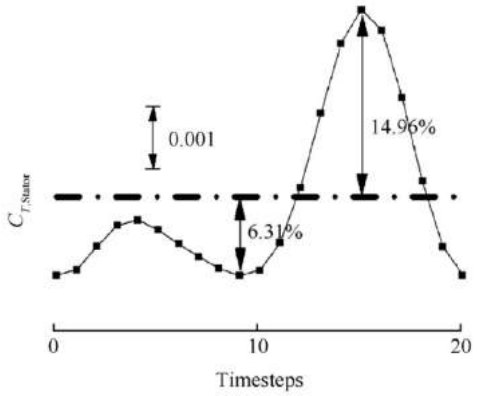

Figure 2.9: Variation of thrust coefficient of an SRV during one propeller blade passing period [32].

The third unsteady effect are the RTVs impinging on the vanes. The RTVs are visualised using a Q-criterion isosurface in Figure 2.10 for four time instants using a vane length equal to the propeller radius R. As can be seen, the RTV arrives at the leading edge (LE) of the stator vane, where viscous effects cause it to be split into two: one at the pressure side (PS) and one at the suction side (SS) of the vane. During the movement to

the trailing edge (TE), both vortices undergo an opposing spanwise motion. This motion can be explained following the same reasoning as for the interaction of a RTV with a trailing wing as done by Johnston and Sullivan [28].

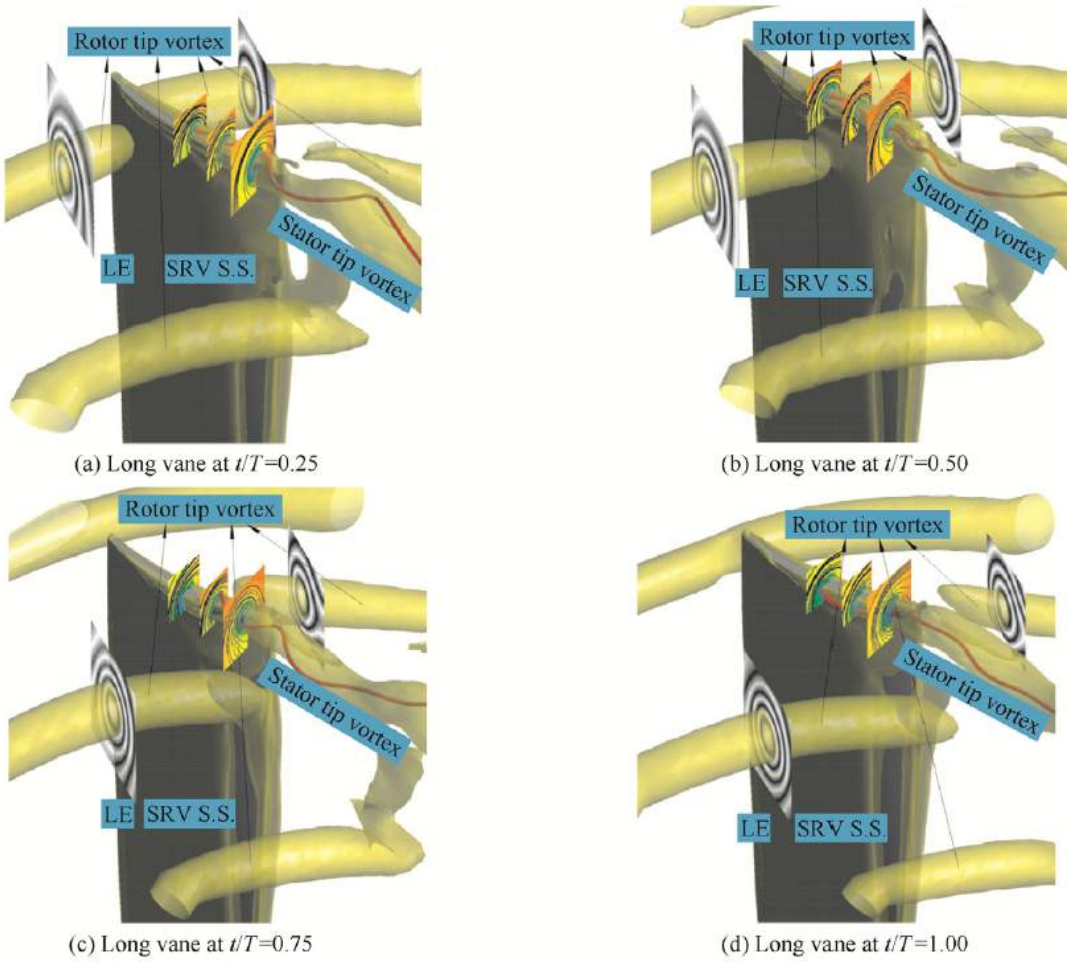

Figure 2.10: Isosurface of $Q = 0.00035$ for a vane of length R for four time instants [32].

The RTVs are propagated downstream in a helical structure, as visible in Figure 2.11. Therefore, the RTV impinges the SRV at an angle α, for which a cross section is shown in Figure 2.12. The RTV is represented by a double arrow, from which the rotation direction can be derived using the right-hand rule. The vorticity can be decomposed into a component perpendicular and tangential to the vane. The tangential component has an effect on the motion of the vortex, which is shown in the cross section B-B' in Figure 2.13. Image vortices are introduced inside the vane which rotate in an opposite direction as the actual vortices and are causing the lateral movement of the outside vortices. As can be seen, the vortices on the SS move in an opposite direction from the vortices on the PS. This effect is called shearing of the vortices and causes them to arrive in a misaligned fashion at the TE. Behind the vane, the vortices tend to reconnect again with various possible mechanisms, such as bridging, binding and threading [27].

Figure 2.11: Helical vortex system in the slipstream of the propeller [45].

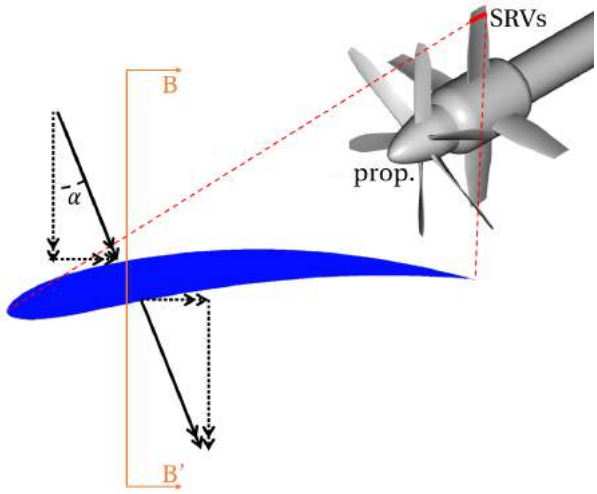

Figure 2.12: Cross section of a vane with a RTV, represented by a double arrow, impinging.

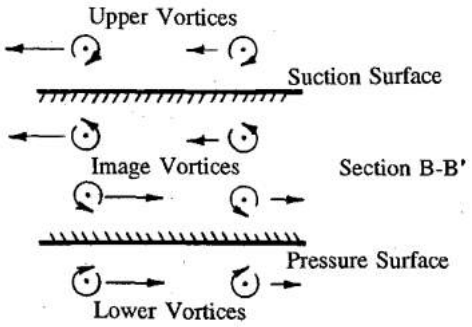

Figure 2.13: Cross section B-B' from Figure 2.12 with vortex components tangential to vane surface and image vortices [28].

Other effects observed when RTVs impinge on a trailing wing might to some extent be present in a configuration with propeller and SRVs. The vortices impinge on the SRV's surface with a low-pressure vortex core [28], which is a result of the required balance between the pressure force and the centrifugal force [26]. Pressure measurements along a wing have shown that viscous effects cause the pressure in the core to increase and the rotational velocity to decrease as the vortices travel along the wing [28]. It has been observed by Johnston & Sullivan [27] that the RTVs thicken on the advancing side of the wing (PS of the vane) and stretch on the retreating side of the wing (SS of the vane). There is a difference in flow velocity on the PS and SS of the vane which might cause the vortices to misalign in the chordwise direction [28]. Finally, both the the image vortices and the higher velocity inboard of the propeller slipstream compared to outboard can have an effect on the RTV shape [28].

2.7. Aeroacoustic effects of propeller with SRVs

2.7.1. Sound fundamentals

To investigate the noise effect of SRVs, a basic understanding of sound is required. Sound is a propagating pressure disturbance in the form of a longitudinal wave [48]. It has a certain wavelength and frequency which

are related using the following expression:

$$\lambda = \frac{c_s}{f} \tag{2.14}$$

where λ is the wavelength, c_s the speed of sound and f the sound frequency.

The pressure fluctuation causing the sound will be denoted as p'. Using the conservation of mass, momentum and energy, the wave equation can be formulated which dictates the propagation of sound waves through air [48]:

$$\frac{1}{c_s^2}\frac{\partial^2 p'}{\partial t^2} - \nabla^2 p' = 0 \tag{2.15}$$

The effective sound pressure p_e is an useful measure to quantify the strength of the sound, which can be determined by taking the root mean square of the pressure fluctuation p'. Following, the sound pressure level (SPL) in dB can be determined using the following expression [48]:

$$\text{SPL} = 10 \cdot \log\left(\frac{p_e^2}{p_{e0}^2}\right) \quad \text{[dB]} \tag{2.16}$$

where $p_{e0} = 2 \cdot 10^{-5}$ Pa. The SPL has a logarithmic scale such that it increases by 6 dB when doubling the effective sound pressure. Depending on the location of the receiver, either constructive or destructive interference can occur between multiple sources of same-frequency sound. Sound sources of different frequency can not interfere.

Real-life sound sources can be classified using various elementary sound sources. The first one is a monopole or harmonically pulsating sphere. A monopole produces homogeneous sound waves which results in an equal effective sound pressure around any sphere centred at the monopole's location [48]. A dipole consists of two closely-spaced monopoles of equal strength and frequency but opposite phase. This results in a non-uniform spatial sound intensity such as in Figure 2.16a, b and c. The same holds when placing two dipoles next to each other, forming a quadrupole (Figure 2.16d).

Representing sound in the frequency domain is an useful analysis method and can be obtained by applying the Fourier transformation to the sound signal in the time domain [48]:

$$C(f) = \int_{-\infty}^{\infty} p'(t) e^{-i2\pi f t} dt \tag{2.17}$$

The equivalent of the effective sound pressure p_e in the frequency domain is the power spectral density $P(f)$. It can be obtained from $C(f)$ as [48]:

$$P(f) = \frac{|C(f)|^2}{T_s} \tag{2.18}$$

where T_s is the duration of the signal in s. When multiplying this power spectral density with the size of the frequency bands, the pressure band level (PBL) is obtained which is equal to the SPL within the specific band. These two variables both have the unit of dB and are often used interchangeably. The PBL can be obtained from the power spectral density as [48]:

$$\text{PBL} = 10 \cdot \log\left(\frac{P(f)\Delta f}{p_{e0}^2}\right) \tag{2.19}$$

where Δf is the length of the specific frequency band. Common bands are the octave bands in which the frequency is doubled over the band such that the bandwidths increase with frequency. When reducing the bandwidth, $1/3^{rd}$ or $1/12^{th}$ octave band are obtained. A bandwidth has to be chosen such that the desired information becomes visible with minimal noise. Finally, when summing the PBL over all frequencies f_i, the overall sound pressure level (OSPL) is obtained as function of emission angle θ [48]:

$$\text{OSPL}(\theta) = 10 \cdot \log\left(\sum_{i=1}^{n} 10^{\text{SPL}(f_i,\theta)/10}\right) \tag{2.20}$$

The human ear has a varying sensitivity to sound from different frequencies, which can be accounted for by applying weighting functions. A-weighting is a common method to account for tonal noise. It is however

prescribed in aircraft legislation that a weighting function designed for broadband noise shall be used for propeller-powered transport aircraft [1], called the perceived noise level [31]. Lines of equal perceived noise levels, expressed in the unit of noy, are shown in Figure 2.14. A sound of 54 dB at 100 Hz has a level of 1 noy and is therefore perceived equally loud as a sound of 38 dB at 1000 Hz. The human ear can therefore be concluded to be sensitive to sounds with a frequency of 1000 Hz and upwards.

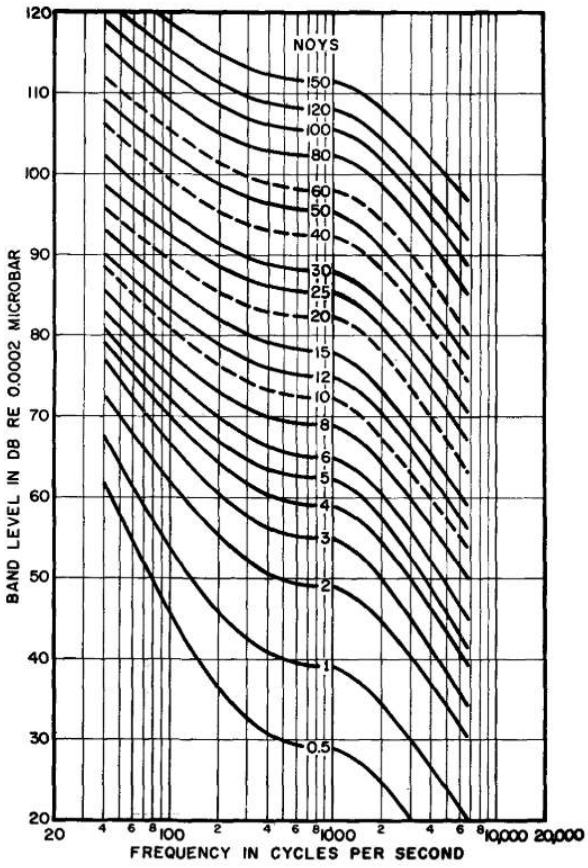

Figure 2.14: PBL versus frequency with lines of equal perceived noise levels in units of noy [31].

2.7.2. Isolated propeller noise sources

There are various noise generating mechanisms present in a propeller causing two different types of noise: harmonic and narrow-band noise on the one hand and broadband noise on the other [36]. The time and frequency representations for these types of noise are displayed in Figure 2.15.

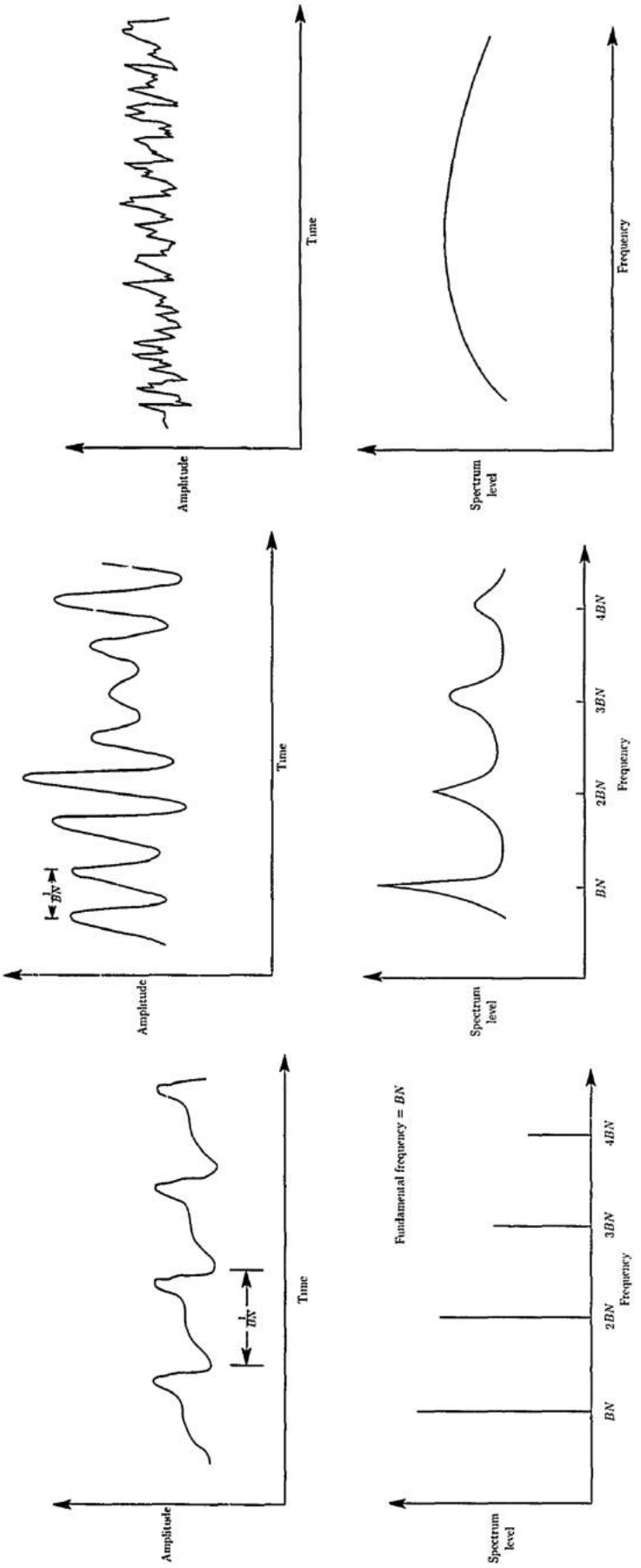

Figure 2.15: Characteristics of, from left to right, harmonic, narrow-band and broadband noise [36].

Harmonic and narrow-band noise

Harmonic noise has distinct peaks in the frequency domain representation, which occur at multiples of the fundamental frequency or first harmonic. In the case of a propeller, the first harmonic occurs at the blade passing frequency (BPF), which can be defined as:

$$BPF = B \cdot n \tag{2.21}$$

where B is the number of blades and n the rotational speed of the propeller in revolutions per second.

Narrow-band noise is similar to harmonic noise as peaks are present in the frequency domain. These peaks are however less distinct and more spread out, especially at higher frequencies. Narrow-band noise resembles reality closer, as can be concluded from the experimentally-obtained frequency domain in Figure 2.17. It is therefore decided to use the term narrow-band noise throughout this report.

In an ideal situation for an isolated propeller with uniform and non-turbulent inflow, there are three steady sources present [36]. Steady sources are constant within the propeller reference frame and cause narrow-band noise for an observer on the ground or in the aircraft. The first steady source is thickness noise, caused by a body moving through air. The amplitude of the noise increases with the volume of the propeller blades and the frequency is dictated by the blade shape and the propeller rotational speed. Secondly, the pressure surrounding the blades causes a periodic disturbance, called loading noise or torque noise. Thickness and torque noise show a radiation pattern of a dipole with maxima in the plane of rotation, see Figure 2.16. Finally, the thickness and loading noise are amplified when the propeller tip experiences transonic flow.

Broadband noise

Broadband noise is random and contains pressure fluctuations from all frequencies. Some frequencies might be better represented causing a varying level in the frequency domain. The vortex sheet shed from the propeller causes broadband noise radiating up- and downstream of the propeller (Figure 2.16c). The propeller slipstream, a consequence of the propeller's thrust, contains shear layers due to velocity gradients at the slipstream edge. These layers are a quadrupole-type broadband noise source, as depicted in Figure 2.16d. Apart from free turbulent flow causing noise, additional noise is generated when turbulent flow impinges a body [36]. This occurs when inflow turbulence hits a blade's leading edge and when turbulence along the blade arrives at the trailing edge. These effects are highly dependent on the boundary layer and therefore hard to predict computationally.

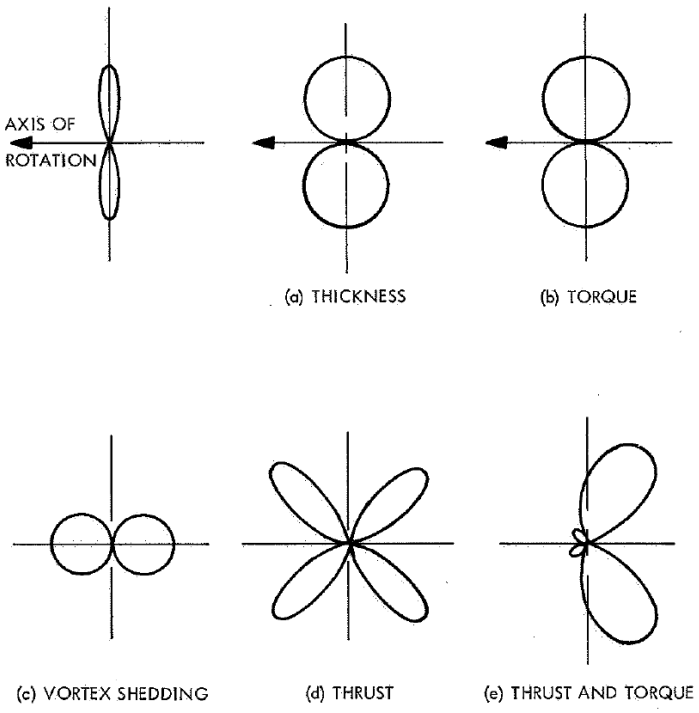

Figure 2.16: Theoretical noise patterns for different propeller noise sources [37].

2.7.3. Propeller + SRVs noise sources

Interaction noise occurs between propeller and SRVs for which the three unsteady aerodynamic effects presented in Section 2.6 are a main cause. Firstly, the upstream effect from the SRVs on the propeller creates a varying loading on the propeller causing narrow-band noise [36]. As this potential effect is seen to be small [32], it is expected to generate minimal noise [49]. Secondly, the wakes of the propeller blades cause a periodic velocity profile in the slipstream, causing a varying loading on the SRVs which is a source of loading noise [36]. As the SRVs are stationary, narrow-band noise is generated with peaks at frequencies equal to multiples of the BPF [49]. Thirdly, the propeller tip vortices impinge on the SRVs which is another cause of narrow-band noise. Additionally, an increased broadband noise level can be expected due to the high amount of turbulence in the propeller wake impinging on the SRVs' surface.

The noise generated by a propeller with SRVs is experimentally studied by Sinnige et al. [49], resulting in Figure 2.17. It can be seen that the SRVs add tonal noise, especially at higher harmonics of the BPF, which opposes results from earlier studies performed by Dittmar & Hall [18]. The difference can be explained by the higher tip Mach number, higher number of blades and larger spacing between propeller and SRVs used in that particular study. The effect of the RTV impingement is not included in Figure 2.17 as it was decided to cut the SRVs in order to avoid vane-vortex interaction noise.

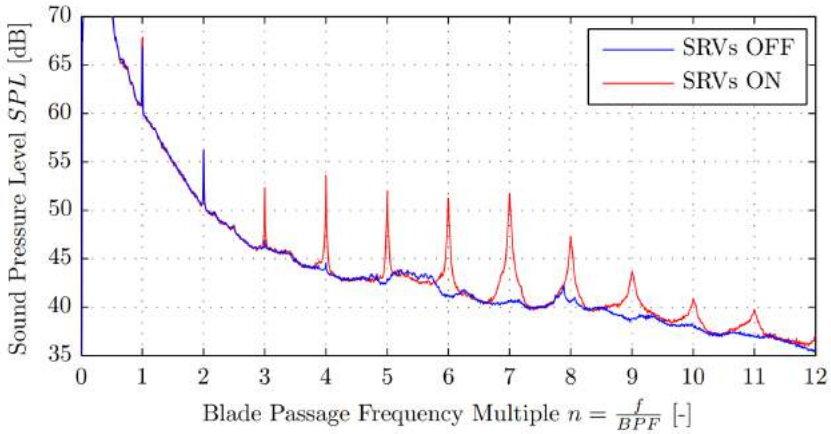

Figure 2.17: Frequency spectra for an isolated propeller (SRVs OFF) and propeller + SRVs (SRVs ON) [49]

3

Methodology

The main method used in the current study is explained, followed by a description of the methods used in preceding research.

3.1. Lattice Boltzmann method

A lattice Boltzmann method (LBM) is chosen for this study as it is widely validated for aerodynamic and aeroacoustic simulations of rotors [4, 9, 42]. Moreover, it is inherently time-dependent and suited for parallel computing [30]. The commercial software package 3DS-Simulia PowerFLOW 5.4a is adopted.

3.1.1. Flow solver

Lattice gas automata

The predecessor of LBM is the lattice gas automata (LGA) model, in which individual particles such as molecules are considered, making this a microscopic method [35]. The particles move over a lattice such that they have discrete velocities in certain directions. A common model has a 2D lattice with six directions and therefore six discrete velocities and is called the Frisch-Hasslacher-Pomeau (FHP) LGA model. As there can only be one particle at a certain node with a certain velocity, the maximum number of particles at a node is six.

The evolution equation of LGA dictates the motion of the particles and can be written as follows:

$$n_i(\vec{x} + \vec{c}_i \Delta t, t + \Delta t) = n_i(\vec{x}, t) + \Omega_i(\vec{x}, t) \tag{3.1}$$

where the Boolean $n_i(\vec{x}, t)$ indicates whether a particle is present at a node with location $\vec{x}$ at time t with a certain velocity $\vec{c}_i$. $\Omega_i(\vec{x}, t)$ denotes the collision operator, which is defined in the FHP LGA model such that the possible collision outcomes occur with equal probability. For example, three output states are possible when two particles collide head-on: equal to the input, rotated 60° clockwise and rotated 60° counterclockwise. This is illustrated in Figure 3.1, where the output states that equal the input states are omitted for brevity.

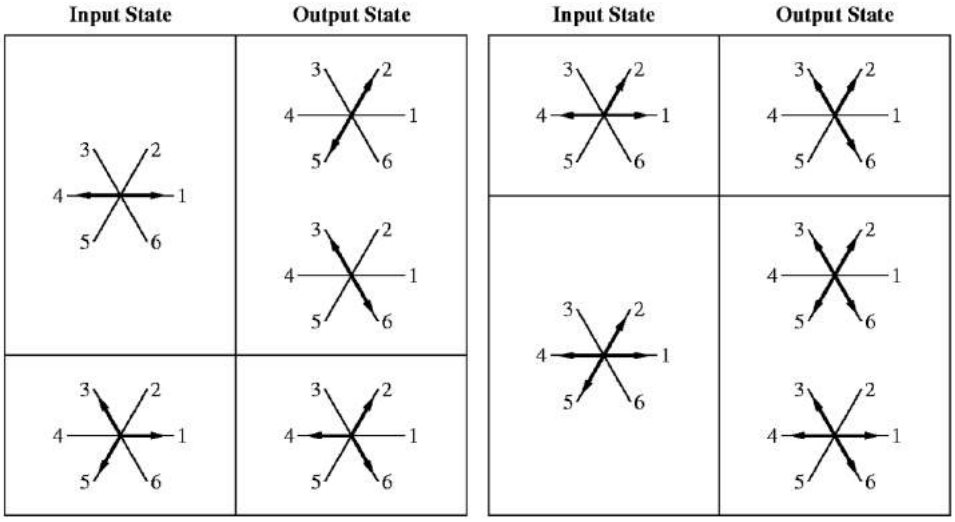

Figure 3.1: Illustration of collisions in the FHP LGA model. The output states which are equal to the input state are omitted [35]

Lattice Boltzmann method

LGA has a number of shortcomings which makes it unusable for fluid dynamic computations. Decisive is that simulations can be very noisy due to fluctuations in $n_i(\vec{x},t)$ induced by the Boolean nature of the method [35]. The lattice Boltzmann method (LBM) is a development from LGA and solves the noise issue by introducing a particle distribution function $f(\vec{x},\vec{\xi},t)$ [35]. This function represents the density of particles at a particular node at location $\vec{x}$ with velocity $\vec{\xi}$ at time t and is therefore continuous in nature. Computational functionality is guaranteed by a Hermite series expansion, which is an enabler of LBM as the first three terms are sufficient to recover the macroscopic hydrodynamic laws [30]. This results in a significant reduction in computational cost. Since no individual particles are considered but distributions of particles, the scale has moved from microscopic to mesoscopic.

For computational purposes, time, space and velocity are discretised. Time is split up into intervals of size Δt and space is discretised using a square lattice with a lattice spacing of Δx. f is defined at the nodes of this lattice. Since an explicit time integration method is used, the Courant number C in the Courant-Friedrichs-Lewy (CFL) condition is set to unity by the solver to ensure stable conditions. The Courant number is defined is:

$$C = \frac{|\vec{u}|\Delta t}{\Delta x} \tag{3.2}$$

with $\vec{u}$ the fluid velocity.

The velocities are discretised such that the distance travelled by a population (set of particles) during one time step Δt brings the population exactly to a neighbouring node [30]. The number of discrete velocities depends on the velocity set which is chosen to be used. These sets are denoted as DdQq where d is the number of dimensions and q is the number of discrete velocities per node. A higher number of discrete velocities results in a higher accuracy at a higher computational cost. In this study, the D3Q19 set is used which is visualised in Figure 3.2. Note that one of the velocities is the resting velocity which is equal to $\vec{0}$. The discrete velocities are defined as $\vec{c}_i$ with i ranging from 0 to 18. The distribution function can now be discretised using the discrete velocities $\vec{c}_i$ and becomes $f_i(\vec{x},t)$.

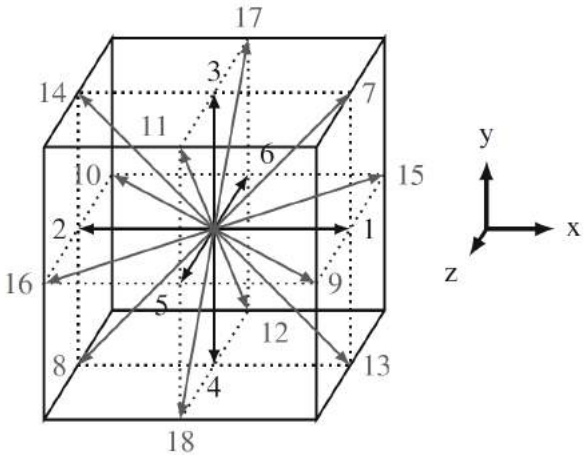

Figure 3.2: D3Q19 velocity set with 19 discrete velocities to neighbouring nodes [30].

At the core of LBM is the lattice Boltzmann equation which can be formulated as [30]:

$$f_i(\vec{x} + \vec{c}_i \Delta t, t + \Delta t) = f_i(\vec{x}, t) + \Omega_i(\vec{x}, t) \tag{3.3}$$

which denotes how a population of particles at location $\vec{x}$ at time t with velocity $\vec{c}_i$ (denoted by the subscript of f_i) traverses to another node during the subsequent time step. The collision operator Ω_i incorporates the collisions occurring between particles by applying a collision model. The Bhatnagar-Gross-Krook (BGK) collision model is adopted for its simplicity, which is defined as [30]:

$$\Omega_i(\vec{x}, t) = -\frac{f_i(\vec{x}, t) - f_i^{eq}(\vec{x}, t)}{\tau} \Delta t \tag{3.4}$$

which directs the population towards an equilibrium state f_i^{eq} at a rate depending on τ, the relaxation time. The equilibrium state is the state of the gas when it has been untouched for a sufficiently long period of time. It follows from the Maxwell-Boltzmann velocity distribution which is a probability function for the particle velocities in an equilibrium gas around the fluid velocity $\vec{u}$ [35]. It can be written in continuous form as [30]:

$$f^{eq} = \frac{\rho}{(2\pi \overline{R} T_K)^{d/2}} e^{-\frac{(\vec{\xi} - \vec{u})^2}{2\overline{R} T_K}} \tag{3.5}$$

with ρ the density of the gas, $\overline{R}$ the gas constant, T_K the temperature, d the number of spatial dimensions and $\vec{u}$ the fluid velocity. After non-dimensionalising the formula, a discrete approximation of f^{eq} is made using a Hermite polynomials expansion [30]. As stated before, it is proven that the first three terms of the Hermite series are sufficient to recover the macroscopic laws for hydrodynamics. When adopting the isothermal assumption for simplicity, the discrete equilibrium distribution function is as follows [30]:

$$f_i^{eq}(\vec{x}, t) = w_i \rho \left(1 + \frac{\vec{u} \cdot \vec{c}_i}{c_s^2} + \frac{(\vec{u} \cdot \vec{c}_i)^2}{2c_s^4} - \frac{\vec{u} \cdot \vec{u}}{2c_s^2}\right) \tag{3.6}$$

with weights w_i, density ρ , speed of sound c_s and fluid velocity $\vec{u}$. The weights w_i are inherent to the chosen velocity set and are displayed in Table 3.1 for the D3Q19 set. The speed of sound constant can be calculated as [30]:

$$c_s^2 = \frac{\Delta x^2}{3\Delta t^2} \tag{3.7}$$

Table 3.1: Weights for the D3Q19 velocity set [30].

Velocities $\vec{c}_i$	**Number**	**Length** $\lvert\vec{c}_i\rvert$	**Weight** w_i
(0,0,0)	1	0	1/3
(±1, 0, 0), (0, ±1, 0), (0, 0, ±1)	6	1	1/18
(±1, ±1, 0), (±1, 0, ±1), (0, ±1, ±1)	12	$\sqrt{2}$	1/36

The coefficients of the Hermite series expansion equal the conserved moments, e.g. density, momentum and energy. The mass and momentum density can be calculated as follows [30]:

$$\rho(\vec{x},t) = \sum_i f_i(\vec{x},t) = \sum_i f_i^{eq}(\vec{x},t) \tag{3.8}$$

$$\rho\vec{u}(\vec{x},t) = \sum_i \vec{c}_i f_i(\vec{x},t) = \sum_i \vec{c}_i f_i^{eq}(\vec{x},t) \tag{3.9}$$

from which the velocity simply follows by dividing the second by the first moment: $\vec{u}(\vec{x},t) = \rho\vec{u}(\vec{x},t)/\rho(\vec{x},t)$. An important criteria for the collision model is the conservation of the moments, which is verified by the fact that these moments can be calculated from both the regular as the equilibrium distribution function.

The operation of the LBM logarithm will now be explained with the aid of the following flow diagram.

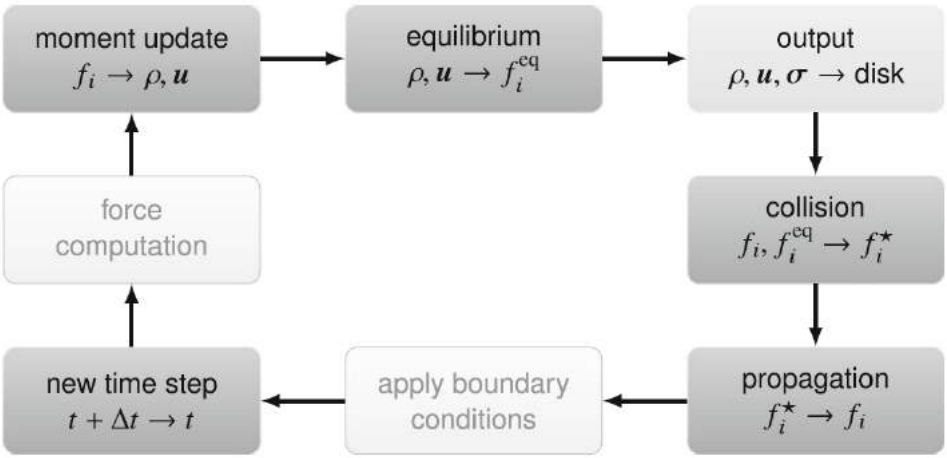

Figure 3.3: Steps taken in the LBM algorithm [30].

Starting from the top left corner, the following steps are performed:

1. The macroscopic variables ρ and $\vec{u}$ are calculated as in Equation 3.8 and 3.9.
2. The equilibrium distribution function is calculated with Equation 3.6.
3. The desired output macroscopic variables can be written to the disk. σ is the viscous stress tensor which can be deducted from f_i.
4. The collision model is executed which results in an intermediate distribution function $f_i^{\star}$.
5. The propagation is performed in which the particles stream towards neighbouring nodes or remain at the same node. This step can be combined with the collision step by using the lattice Boltzmann equation directly (Equation 3.3).
6. Boundary conditions can be applied such as velocity and pressure boundaries for the inflow and outflow.
7. The algorithm moves towards the next time step.
8. Possible external forces can be applied.

Turbulence modelling

LBM is capable of resolving all turbulence scales exactly [13], which is practically feasible up to a Reynolds number of 10,000 [21]. Since this is in the realm of moving insects, it is insufficient for the current application. To allow for higher Reynolds numbers, subgrid-scale turbulence models are needed [13]. The larger turbulence scales are called integral or anisotropic scales and are simulated as eddies. These scales are specific to the geometry, difficult to model and have a large effect on the flow. The smaller turbulence scales are called

inertial and dissipative scales and are modelled using universal models. This is illustrated in Figure 3.4 and relates to a Navier-Stokes method called large eddy simulation (LES). The method in LBM is called very large eddy simulation (VLES) accordingly.

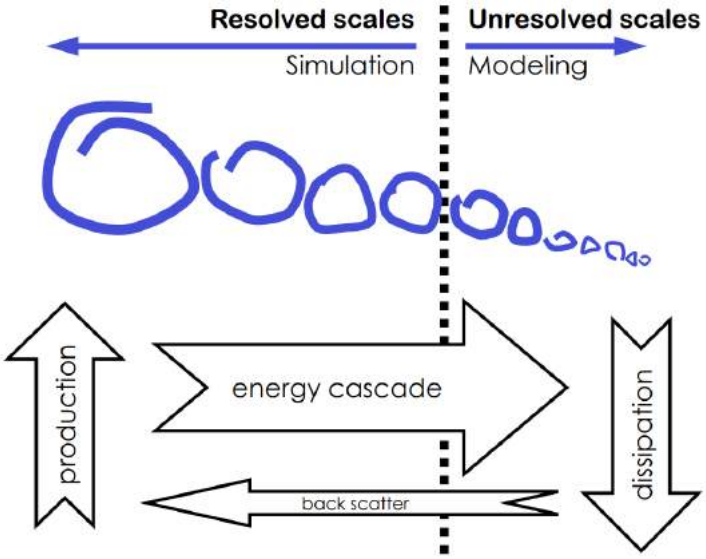

Figure 3.4: Simulated and modelled turbulence scales including energy flows. The dotted line indicates the grid size [25].

Yakhot & Orszag [56] developed the $k-\epsilon$ renormalization group (RNG) model which is used in LBM to compute a turbulent relaxation time that is added to the viscous relaxation time τ:

$$\tau_{\text{eff}} = \tau + C_\mu \frac{k^2/\epsilon}{(1+\eta^2)^{1/2}}, \tag{3.10}$$

with k the turbulent kinetic energy, ϵ the turbulent dissipation rate, $C_\mu = 0.09$ and η depending on factors such as the local strain and vorticity [4].

Following, the dimensionless kinematic viscosity ν is related to the relaxation time as [4]:

$$\nu = c_s^2(\tau - \frac{\Delta t}{2}). \tag{3.11}$$

The model includes a memory effect such that the solution is dependent on the results at an earlier time at an upstream location [12]. Nonlinear terms describe secondary flow structures in a similar way as higher-order turbulence transport models. Interestingly, a strong analogy is present between this turbulence model and Maxwell's kinetic theory of microscopic thermal fluctuations although both describe different physical processes [12].

Wall model

As LBM makes use of an automated Cartesian grid generation mechanism, a wall model is required to represent curved surfaces. Additionally, a high grid resolution is required to resolve the boundary layers adjacent to surfaces with a no-slip boundary condition. A wall model enables the use of a coarser grid by modelling the boundary layer which reduces the computational effort. A pressure-gradient-extended wall-model (PGE-WM) is used [4], which is an extension of the general law-of-the-wall model [52]. The PGE-WM can be formulated as

$$u^+ = \tfrac{1}{\kappa} \ln\left(\tfrac{y^+}{A}\right) + B \tag{3.12}$$

where $\kappa = 0.41$ and $B = 5.0$ are constants. y^+ and u^+ are the non-dimensionalised wall distance and velocity respectively, which can be expressed as:

$$y^+ = \frac{u_\tau y}{\nu}, \quad u^+ = \frac{u}{u_\tau}, \tag{3.13}$$

with u_τ the friction velocity, y the distance to the wall, ν the kinematic viscosity and u the velocity parallel to the wall. Finally, A incorporates the phenomenon that a positive stream-wise pressure gradient causes the flow in the boundary layer to slow down and expand. The expression of A is:

$$A = 1 + \frac{f_L |\frac{\mathrm{d}p}{\mathrm{d}s}|}{\tau_w}, \quad \text{when} \quad \vec{u}_s \cdot \frac{\mathrm{d}p}{\mathrm{d}s} > 0 \tag{3.14}$$

$$A = 1, \quad \text{otherwise} \tag{3.15}$$

where f_L is the length scale of the unresolved near-wall region, $\mathrm{d}p/\mathrm{d}s$ is the stream-wise pressure gradient, τ_w is the wall shear stress and $\vec{u}_s$ denotes the direction of the local flow. A method based on the bounce-back scheme [13] is used to solve the flow up to the nodes closest to the wall, which defines the boundary conditions for the wall model.

3.1.2. Computational aeroacoustics

It is possible to predict the propagation of sound pressure fluctuations using LBM as it is an inherently time-dependent and compressible method with low dissipation and dispersion properties [8]. However, as a resolution of 12 voxels per wavelength or more is required to accurately predict the sound waves [7], it is computationally expensive to directly estimate the far-field sound field. A hybrid method is adopted which is based on LBM to simulate the near-field noise and an acoustic analogy method to predict the far-field noise. This analogy method is based on an inhomogeneous wave equation, being the Ffowcs Williams-Hawkings (FW-H) equation [7]:

$$\frac{1}{c^2}\frac{\partial^2 p'}{\partial t^2} - \nabla^2 p' = \mathrm{RHS} \tag{3.16}$$

where the left-hand side is equal to the homogeneous wave equation (Equation 2.15) which predicts the propagation of sound through air. The right-hand side (RHS) consists of dipole sources [15], for which the strengths are obtained by integrating the pressure on the solid surfaces. As the unsteady pressure on the surface is the only input into the FW-H equation, any sound originating in the turbulent slipstream is neglected. The unsteady pressure is recorded at spatial intervals equal to $1/15^{th}$ of the wavelength of the 12^{th} harmonic of the BPF at a frequency equal to 15 times the 12^{th} harmonic.

3.1.3. Computational setup

The simulation volume is defined as a rectangle with a length of $25.7D$ and a width and height of $15D$, as visualised in Figure 3.6. The centre and origin are defined by the intersection of the propeller axis with the propeller plane. A velocity inlet is defined with a V_∞ of 29 m/s and a temperature of 293.15 K. The outlet is defined by a static pressure of 101,325 Pa and a free-flow direction. No-slip boundary conditions are applied on the propeller, SRVs, spinner and fairing, which are denoted in Figure 3.7a. A free-slip boundary condition is applied to the nacelle which extends to the outlet plane. A volume of revolution is generated containing the propeller and spinner with a clearance from the surfaces of 19 mm. This value has been selected to avoid errors caused by the boundary rings of the volume spanning more than two regions of variable resolution. A rotating sliding-mesh local reference frame is defined for this volume with an angular velocity n = 119 rev/s, corresponding to the operating condition of J = 0.6. An acoustic sponge is implemented by varying the kinematic viscosity per unit temperature from 0.005 m^2/sK close to the geometry to 0.5 m^2/sK in the farfield. An exponential transition region is present between a distance of $3.3D$ and $4.9D$ from the centre of the coordinate system, see Figure 3.6. Simulations are seeded with the end result of the preceding simulation with a coarser grid. Time convergence is reached after two propeller rotations (N_{rot}), as is concluded from Figure 3.5 where the instantaneous propeller thrust coefficient is plotted with time. The root mean square error (RMSE) is included which is calculated using the values from the start of the simulation to the particular time step. Results are subsequently stored for three propeller rotations.

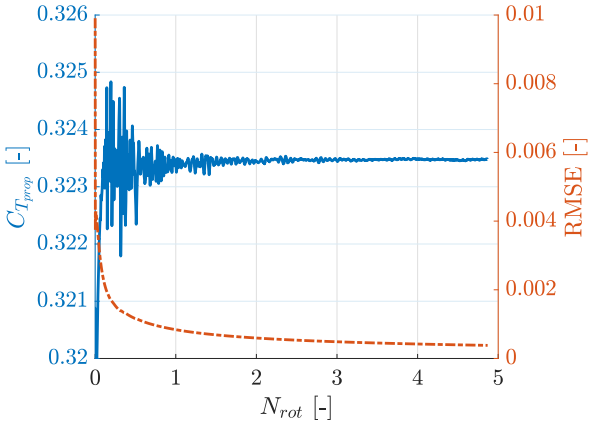

Figure 3.5: Instantaneous propeller thrust coefficient on the left vertical axis and the root mean square error (RMSE) on the right. Time is expressed as number of propeller rotations N_{rot} from the start of the simulation on the horizontal axis.

12 variable resolution (VR) regions are defined which are numbered increasing with resolution, as visualised in Figure 3.6 and 3.7. The resolution increases with a factor of two from one VR region to the next. The finest region (VR12) is defined by an offset of 0.030 times the propeller root chord c_r from regions around the leading edge (LE, displayed in orange in Figure 3.7), trailing edge (TE, green) and the tip (blue) of both the propeller and vanes. The regions around the LE and tip of the propeller are added in order to capture the high surface curvature and the accompanying high pressure gradients accurately, which are visualised by the static pressure contours around a blade in Figure 3.8. The region around the propeller TE has been added in order to capture the shape of the blunt trailing edge accurately. Similar regions are applied around the SRVs. The VR regions around the tip of the SRVs have been extended in spanwise direction to capture the propeller tip vortex development over the SRVs accurately, visible in blue in Figure 3.7a. For both the propeller and SRVs, the LE and TE regions are defined to be approximately 10% of the local chord. The propeller tip region has a similar size and the vane tip region has a spanwise length of $0.16R$.

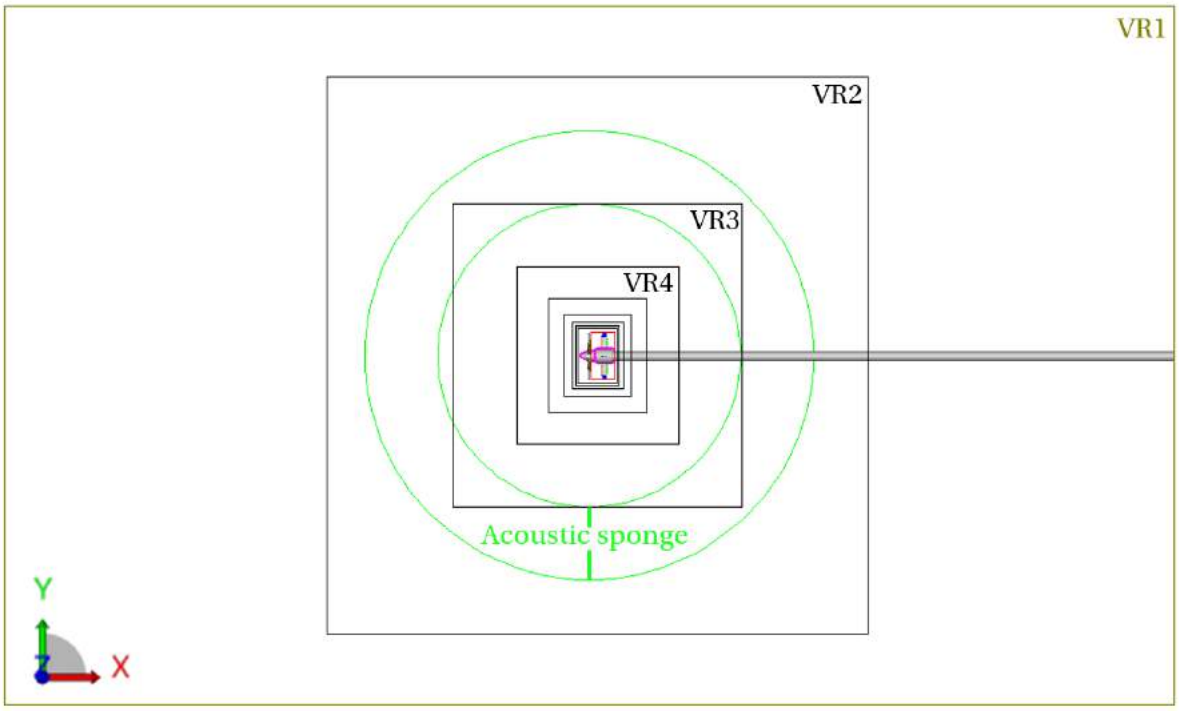

Figure 3.6: Visualisation of the VR regions in the far-field. The adopted axis system and the acoustic sponge are indicated.

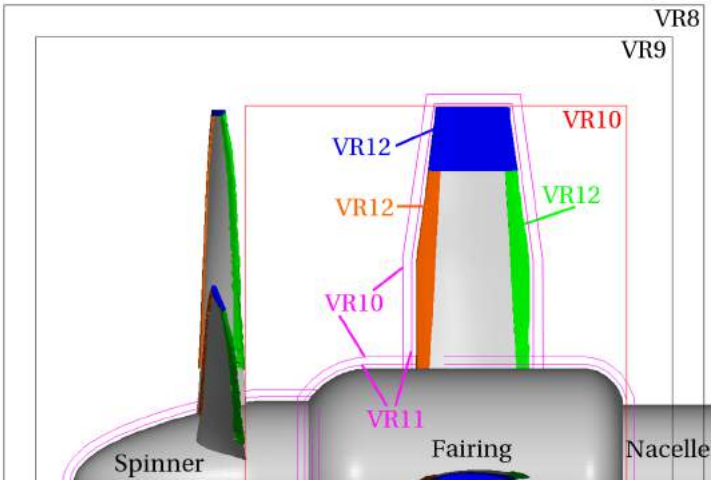

(a)

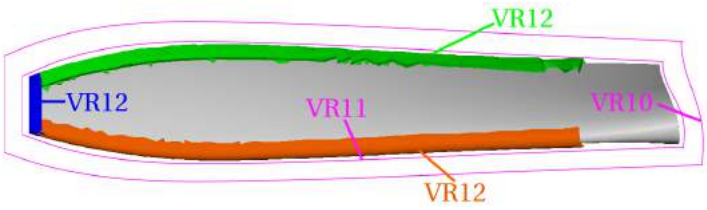

(b)

Figure 3.7: Visualisation of the VR regions in the near-field (a) and around a propeller blade (b).

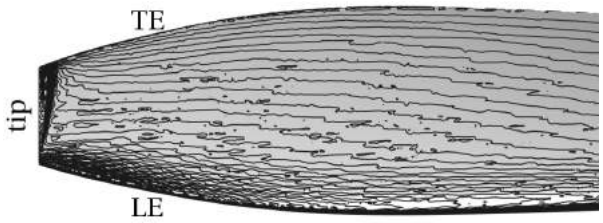

Figure 3.8: Time-averaged static pressure contour around a propeller blade with the leading edge (LE), trailing edge (TE) and tip indicated.

VR11 and VR10 consist of regions around all no-slip boundary surfaces with offsets of respectively $0.061c_r$ and $0.18c_r$. These regions are displayed in purple in Figure 3.7. Additionally, VR10 consists of a cylinder region (red in Figure 3.7a) aimed at capturing the propeller slipstream. This cylinder has a diameter of $1.0D$ and ranges from $x = 0.45c_r$ to $x = 6.8c_r$. VR9 (black in Figure 3.7a) consists of a cylinder of diameter $1.2D$, ranging from $x = -3.0c_r$ to $x = 7.6c_r$. VR8 to VR2 (also black in in Figure 3.6) are defined by an offset from this cylinder, sized such that there are 10 voxels present in between two cylinder boundaries. Finally, VR1 is the simulation volume, displayed in olive in Figure 3.6.

Slipstream and far-field VR

A comparison has been performed between two grids with different VR setup for the isolated propeller, called grid A and grid B. The cylinder region of VR10 is changed whereas the VR10 offset regions remain unaltered, see Figure 3.9 where the VR regions are presented. In grid A, a hollow cylinder is defined from $r/R = 0.7$ to $r/R = 1.2$ and from $x = 0.45c_r$ to $x = 6.1c_r$. In grid B, a solid cylinder is defined with outer radius $r/R = 1.1$ and the same axial dimensions. Additionally, 20 voxels are present between the cylinders constituting VR8 to VR2 in grid A, while this number is reduced to 10 in grid B. Grid B thus contains a higher resolution in the root region of the slipstream and a lower resolution in the far-field. The following results are obtained for a resolution of 100 voxels per c_r for VR11 as VR12 has not been implemented for neither grid A nor B.

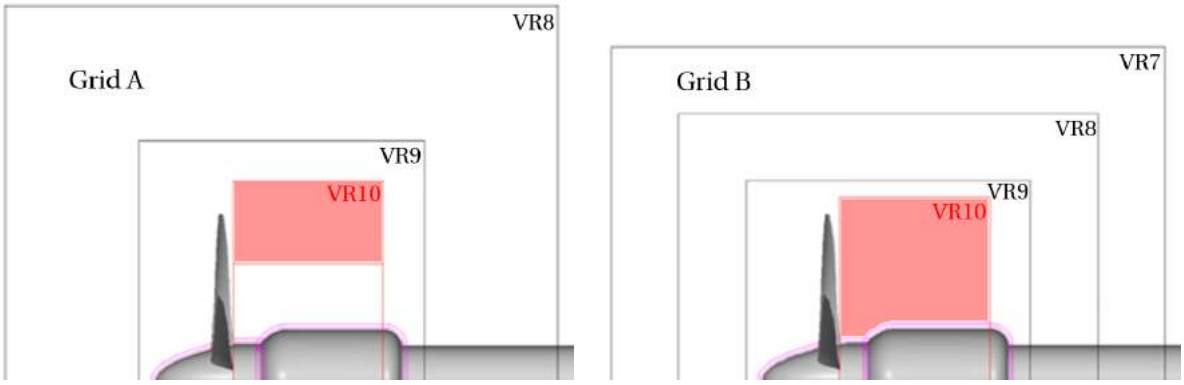

(a) (b)

Figure 3.9: Visualisation of the VR regions in the near-field for grid A in (a) and grid B in (b).

In Figure 3.10, the λ_2 criterion has been applied to the phase-averaged results to visualise the vortices. Isosurfaces are displayed in purple for a λ_2 value of $-3 \cdot 10^6$ s^{-2}. It can be seen that more root vortices are visible using mesh B, as the higher resolution in this regions allows for the smaller effects to be solved more accurately. The propeller C_T is equal for grid A and B. Further comparison is performed using the axial velocity V_a and tangential velocity V_t in two planes downstream of the propeller, i.e. at $x/D = 0.24$ and $x/D = 0.45$. The results are time-averaged over three propeller rotations and spatially-averaged into thirty radial segments. In Figure 3.11 and 3.12, the results are presented for the axial and tangential velocity respectively. A small difference in axial velocity is observed and a considerable difference is seen in tangential velocity in the region of $0.4 < r/R < 0.7$. Although the root vortices are lower in strength than the tip vortices, as can be concluded from the phase-averaged out-of-plane vorticity presented in Figure 3.13, they do have an impact on the flow. It is therefore decided to use a solid cylinder in VR10, as is done in grid B.

It can be concluded from the presented results that the use of less resolution in the far-field has a negligible impact on the results close to the propeller. It does reduce the computation time considerably as grid B has 15% less voxels than grid A although more voxels are present in the slipstream close to the propeller due to the solid VR10 cylinder. It is therefore decided to apply 10 voxels in between the far-field VR cylinders.

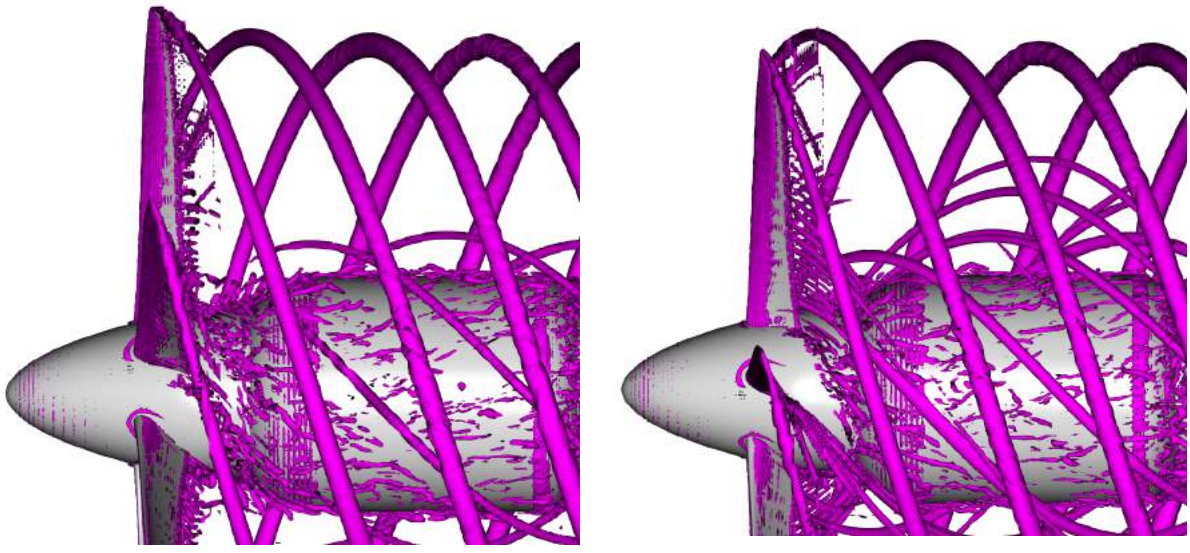

(a) (b)

Figure 3.10: Isosurface of $\lambda_2 = -3 \cdot 10^6$ s^{-2} for phase-averaged results obtained with grid A (a) and grid B (b).

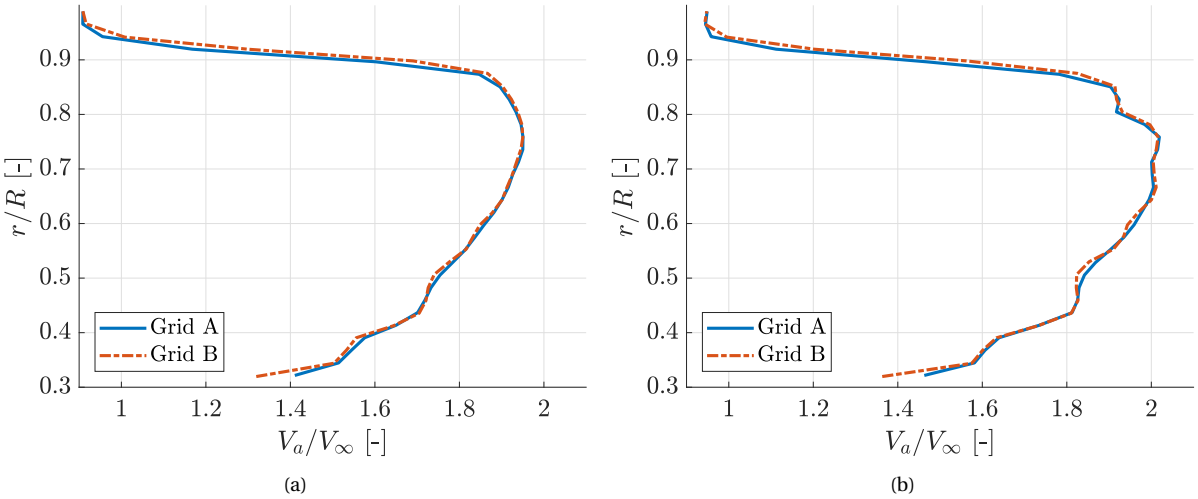

(a) (b)

Figure 3.11: Time- and spatially-averaged axial velocity in planes downstream of the propeller at $x/D = 0.24$ (a) and $x/D = 0.45$ (b) for grid A and B.

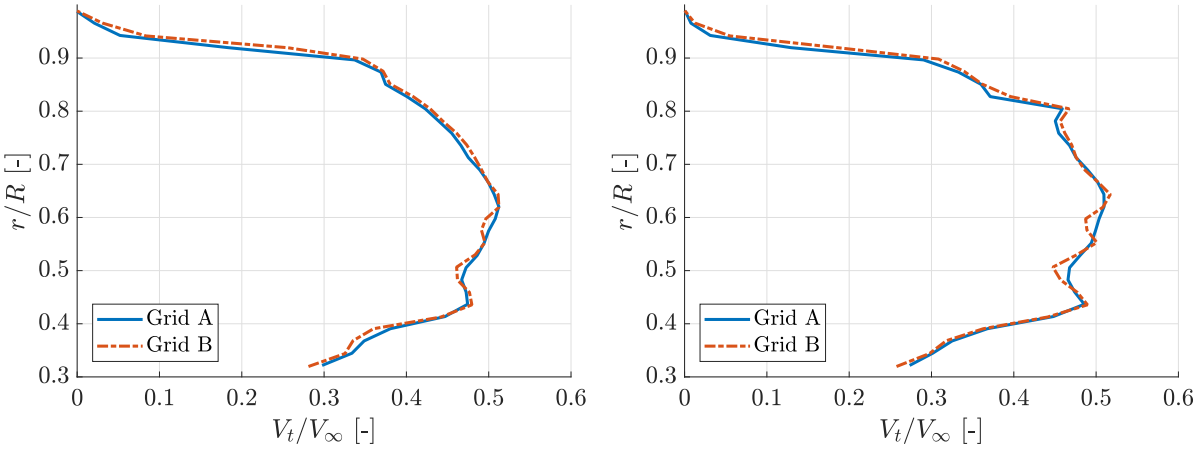

(a) (b)

Figure 3.12: Time- and spatially-averaged tangential velocity in planes downstream of the propeller at $x/D = 0.24$ (a) and $x/D = 0.45$ (b) for grid A and B.

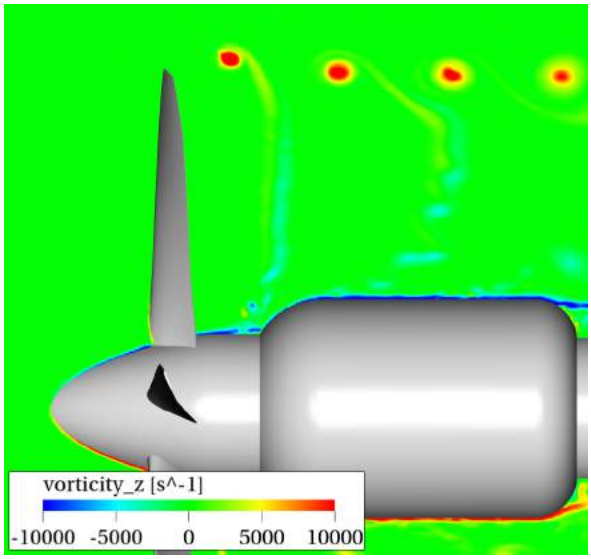

Figure 3.13: Phase-averaged out-of-plane vorticity in a plane containing the rotational axis. Results obtained using grid B.

Inflow turbulence intensity

A turbulence intensity I of 0.5% is required at the propeller plane to match the situation in the experiment and the RANS simulation [33]. The turbulence intensity is defined as [47]:

$$I = \frac{u'}{|\vec{u}|} = \frac{\sqrt{\frac{2}{3}k}}{|\vec{u}|} \tag{3.17}$$

where u' is the root mean square of the turbulent velocity fluctuations, $|\vec{u}|$ the magnitude of the mean flow velocity and k the turbulent kinetic energy. As the turbulent dissipation is unknown, the turbulence intensity at the inlet is first set to 0.5%. This results in a turbulence development from the inlet to the propeller plane as shown in blue in Figure 3.14. The value at $x/D = 0$ equals 0.3439%, which is used to adapt the inlet value to a value of $\frac{0.5}{0.3439} \cdot 0.5 = 0.727\%$. The resulting turbulence intensity development is shown in red in Figure 3.14. As the value at the propeller plane is close to the desired 0.5%, the approach is verified.

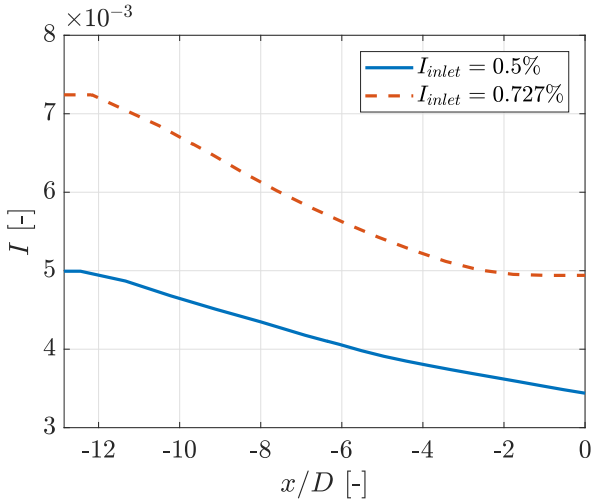

Figure 3.14: I from the inlet to the propeller plane for $y/D = 5$ and $z/D = 0$

3.1.4. Data reduction

As LBM is inherently time-dependent, results can be time-averaged, phase-averaged or displayed instantaneously. Results are only presented in an instantaneous fashion if a variable is plotted with respect to phase angle ϕ. Phase-averaging is performed by averaging values separated by an interval of $\phi = 60°$. As there are

six propeller blades present, the flowfield is similar every $\phi = 60°$. It is prescribed in the captions whether results are time- or phase-averaged.

Forces are obtained by integrating the total surface force on the body, summing the pressure and frictional force. The performance coefficients are deducted from the integrated values. In order to obtain thrust distributions, 474 segments are placed on the SRV and the force on each segment is obtained. As the raw signal shows excessive fluctuations, a moving average has been applied with an averaging span of 11. An interval of 11 segments is averaged, after which the interval is shifted by one segment to obtain the next value. This method has been repeated three times to obtain a sufficiently smooth signal.

Velocity and swirl distributions in the slipstream are obtained by retrieving the values on a 2D grid with a spacing of 0.001 m. The values are averaged over thirty annuli of same radial size for the range of $0.31 < R < 1$. In order to have a fair comparison with experimental results, the velocity components have not been averaged over the full circumference. Averaging is performed over a passage of 60° such that the location of the SRVs are not included, visualised in Figure 3.15. A separation of 10° is present between the averaging area and the SRV on the vane's suction side (SS) and 20° at the vane's pressure side (PS).

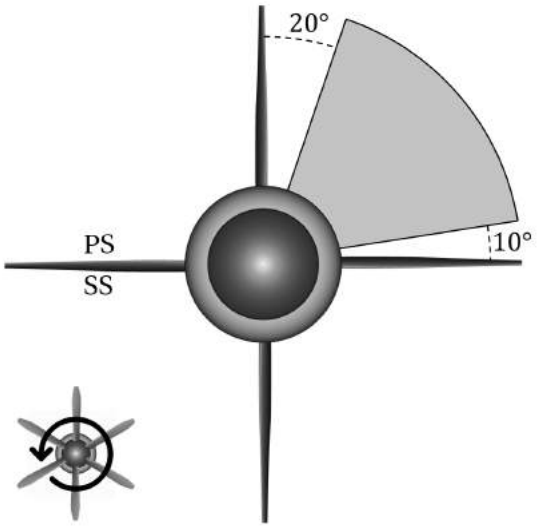

Figure 3.15: Front-view of the geometry with the averaging interval indicated. Suction and pressure side of a vane and the propeller rotation are indicated. The propeller has been hidden.

When the average swirl angle is plotted against the axial location, values are obtained on 2D grids with a spacing of 0.005 m. Averaging is performed over $0.31 < R < 1$ and a number of axially-spaced grids are used to obtain the axial swirl development.

The acoustic pressure at 72 equispaced points on a ring with a radius of $10D$ is calculated using the FW-H analogy using the unsteady pressure at the surface. The ring lies in the $y = 0$-plane and is centred around the midpoint between propeller and SRVs, see Figure 3.16. 72 pressure traces of each 5625 samples are obtained from the FW-H method. The rotation of the propeller blades is taking into account but no body or flow velocity is applied. Following, the Welch's method [55] is applied to transform to the power spectral density $P(f)$ in the frequency domain. This method reduces the numerical noise compared to a simple discrete Fourier transform by applying multiple transformations on overlapping segments. A segment length of 2048 is used as Hamming window length with 50% overlap and 8192 discrete Fourier transform points. The $P(f)$ is used to calculate the pressure band level (PBL) and the overall sound pressure level (OSPL), using the equations given in Section 2.7.1.

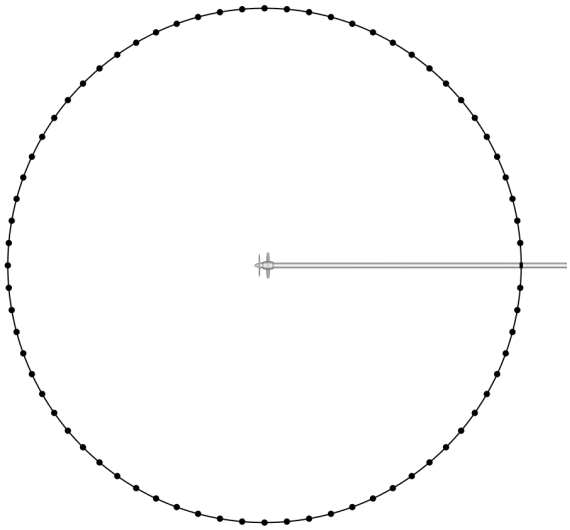

Figure 3.16: Top-view of the geometry with the acoustic pressure measurement ring.

3.2. Reynolds-averaged Navier-Stokes

A Reynolds-averaged Navier-Stokes (RANS) simulation of the isolated propeller has been performed in preceding research of Li et al. [33]. The results were used in the design process in that study and will be used for validation purposes in the current study. A short description will be given.

Due to symmetry, only one blade sector of 60° was modelled and periodic boundary conditions have been implemented. A structured mesh has been applied around the propeller and an unstructured mesh was used to resolve the slipstream. A velocity inlet of 29 m/s was applied with a turbulence intensity of 5% and an eddy viscosity ratio of 10 such that the turbulence intensity at the propeller plane equalled 0.5%, similar to the level in the wind tunnel. The undisturbed static pressure was defined at the outlet and the same boundary conditions as in the LBM model were applied to the surfaces.

The non-linear term in the Navier-Stokes equations, containing the influence of the small-scale fluctuations, is impossible to solve and therefore modelled with turbulence models [29]. Common turbulence models are the $k-\epsilon$ and $k-\omega$ model. The $k-\epsilon$ model is superior for external flows and the $k-\omega$ is better in predicting turbulence in boundary layers and more suitable for flows with high pressure gradients and possible separation [43]. The SST model combines the two which was the selected model to be used together with the automatic wall function.

A grid refinement study was performed using three different resolutions ($y^+ = 4$, 2 and 1) for which thrust coefficients C_T were obtained to be within 1% of the $C_{T_{y^+=1}} = 0.322$. The grid convergence was confirmed by applying the grid convergence index. Additionally, the convergence in slipstream velocity was verified.

3.3. Geometry

The adopted geometry follows directly from Li et al. [33] and is presented in Figure 3.18a together with the adopted axis system. The propeller (Figure 3.17) is a 1:9 scaled-model of a Dowty Rotol propeller, used on the IPTN N-250. This typical twin-engined regional turboprop aircraft was designed for 50 passengers and a cruise speed of 154 m/s at an altitude of 7620 m [2]. The propeller features six blades and a diameter D of 0.4064 m, see Figure 3.17. The hub of the propeller is 0.084 m in diameter, the root chord c_r 33 mm in length and the blade pitch angle β equals 30° at 70% of the radius.

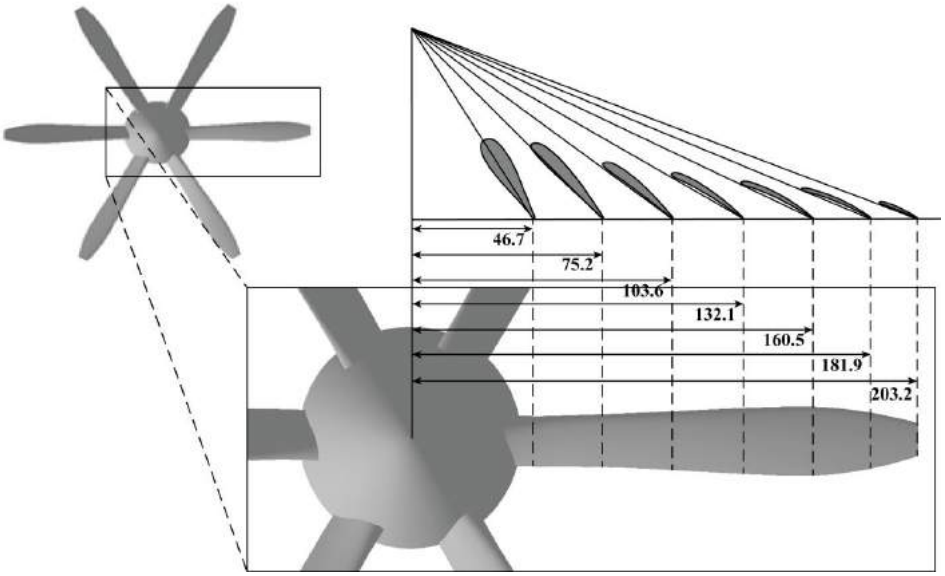

Figure 3.17: The scaled propeller model [33].

The vanes were modelled by circulation distributions using a model based on lifting line theory (LLT) [20]. The input velocity field followed from a RANS simulation as presented in Section 3.2. The optimum circulation distribution was determined by maximising the lift on the vanes. As the SRVs are relatively slender, 3D effects can be neglected and the assumption was made that the geometry is build from 2D sections [14]. The shape of the airfoils was determined using XFOIL, a 2D higher order panel method with a model for the influence of the viscous boundary layer [19]. The sectional drag is minimised while keeping an appropriate stall margin which is necessary for the vanes to perform well under a large range of inflow angles caused by the unsteady propeller slipstream.

Although the model suggested an optimum vane number of 9, 4 vanes with a radius equal to the propeller radius R were used due to a practical constraint in the experimental setup. The vanes were positioned on a fairing of diameter $0.31D$ with their leading edge 135 mm behind the propeller. The chord at the root measured 60 mm and at the tip 40 mm, see Figure 3.18a. The fairing radii have been implemented differently in RANS, which becomes evident when comparing Figure 3.18a to Figure 3.18b. The SRV shape is expressed in Figure 3.19 in terms of the radial distribution of five variables, explained in the caption.

The LLT model predicted the SRVs to produce an additional 3.4% of the propeller thrust at the design condition of $J = 0.6$ and $V_\infty = 29$ m/s. A high propeller loading condition was chosen to obtain a measurable thrust on each vane in the experimental campaign despite a low free-stream dynamic pressure.

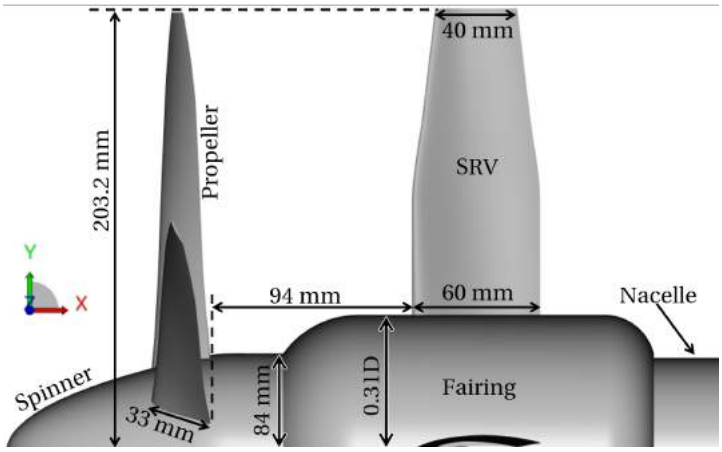

(a)

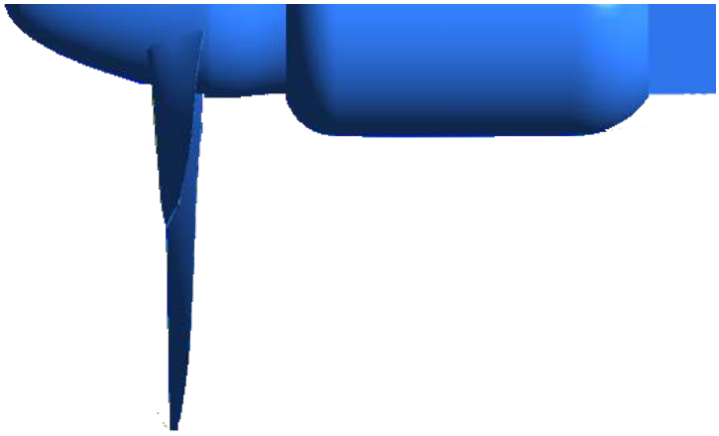

(b)

Figure 3.18: Geometry of propeller with SRVs which is used in LBM and experiment in (a) and in RANS in (b).

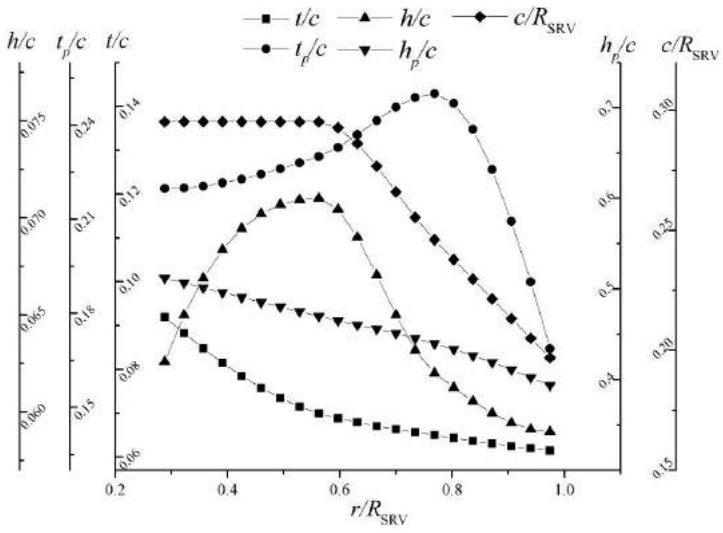

Figure 3.19: The shape of a vane expressed in terms of maximum thickness t, maximum thickness location t_p, maximum camber h, maximum camber location h_p and chord length c as function of radial location.

3.4. Experimental setup

Experiments were conducted with the designed SRVs and the propeller model in a low-speed open-jet wind tunnel at Delft University of Technology, visible in Figure 3.20. It has an octagonal nozzle with a width and height of 2.85 m or an equivalent diameter of 3 m and a 3:1 contraction ratio [33, 34]. A honeycomb flow rectifier along with five screens ensures a straight flow with relatively low turbulence level of about 0.5% and a maximum flow speed of 29 m/s. The flow contracts with a 4.75° semi-angle due to the development of the jet shear layer. Finally, a constant temperature of 20°C is achieved by a heat exchanger of 350 kW which extracts the heat added by the 500 kW fan.

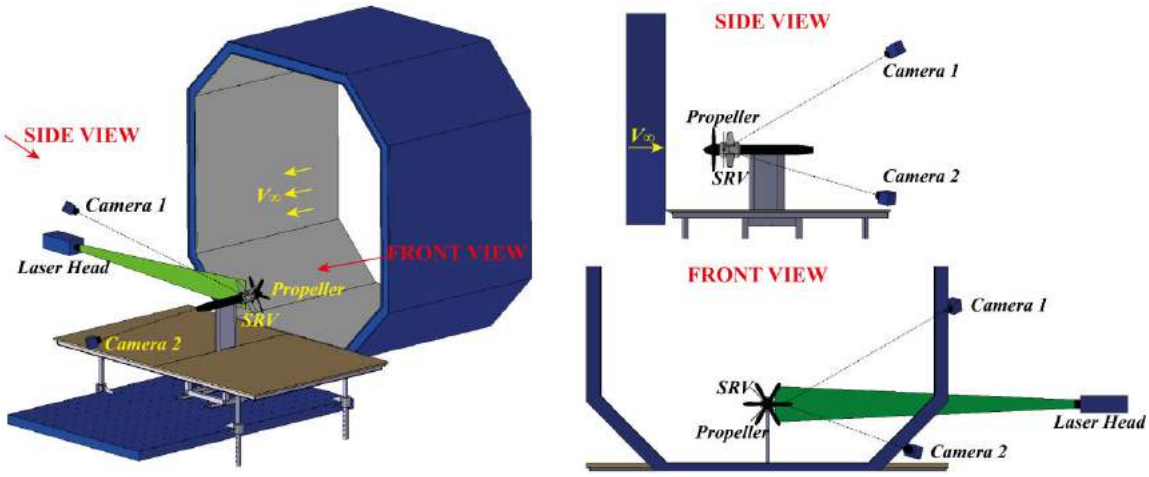

Figure 3.20: Visualisation of the wind tunnel setup including the PIV equipment [33].

The propeller was powered by a Tech Development Inc. Model 1999 pneumatic motor [33] and featured an integrated six-component rotating shaft balance to measure the propeller forces and moments during operation [41]. With an assumption of linear uncertainty propagation, the uncertainty of the thrust coefficient was calculated to be 0.0019 for the design condition.

The SRVs were mounted on sliding units, positioned on a track inside the fairing, providing freedom only to axial translation. A load cell was installed in front of the vane measuring the axial thrust per vane. It should be noted that a non-zero adhesion force of unknown magnitude due to the sliding system made the load cell readings indicate the lower bound of the thrust that the SRVs produced [33]. An uncertainty of 0.0012 in thrust coefficient for all vanes has been calculated using the rated accuracy of the load cell and the standard deviation of the measured thrust.

Measurements of the flowfield in two planes located $0.4c_r$ up- and downstream of the SRVs were taken using stereoscopic particle-image velocimetry (PIV). The benefit of stereoscopic PIV systems is that all three velocity components can be measured in a two-dimensional plane [44]. The PIV setup is visible in Figure 3.20. A smoke generator produced tracer particles of around 1 μm in diameter and a laser was used as a light source with a pulse duration of 9 ns [33]. Correlation was applied on small subframes, called interrogation spots, to determine the average particle velocity [44]. An overlap of 75% was used among adjacent spots to increase the number of velocity vectors by a factor of 16. The acquired spatial resolution was 0.55 mm and the measurement plane was 225x150 mm in size. Based on correlation statistics, the uncertainty in PIV results was calculated to be 0.85 m/s for the V_a and 0.73 m/s for V_t [33]. These uncertainties were determined for the instantaneous velocity components and will reduce after averaging.

4

Validation

The current method is validated using RANS and experimental data obtained by Li et al. [33].

4.1. Grid independence study

4.1.1. SRVs OFF

In order to have a grid-independent solution, a grid refinement study is performed. The time-averaged propeller thrust coefficient $C_{T_{prop}}$ of the isolated propeller (SRVs OFF case) is used as the first reference variable. Four grids are generated with increasing resolution, for which the obtained thrust coefficients are displayed in Figure 4.1. The resolution is expressed as voxels per propeller root chord c_r for the VR12 region. A clear converging trend is visible and an excellent match is obtained with the values obtained from RANS and experiment. These reference values are included in Figure 4.1 by two horizontal dashed lines.

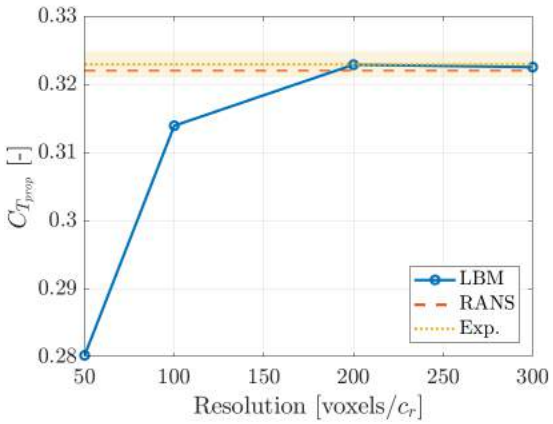

Figure 4.1: Averaged isolated propeller thrust coefficient obtained using grids with increasing resolution. Reference values from RANS and experiment (including uncertainty) are included.

The convergence of aeroacoustic results is displayed in Figure 4.2a using the overall sound pressure level (OSPL) around a ring at a distance $10D$ from the midpoint between propeller and SRVs, as described in Section 3.1.4. Use has been made of the FW-H equation to predict the sound pressure in the far-field. The OSPL at $\theta = 90°$ is displayed separately in Figure 4.2b as the convergence trend at this location of maximum sound is hard to deduct from Figure 4.2a. In both Figure 4.2a and 4.2b a clear converging trend is observed and the solutions for 200 voxels/c_r and 300 voxels/c_r overlap (with a maximum difference of 1.4 dB at $\theta = 205°$) such that the aeroacoustic results are concluded to be converged.

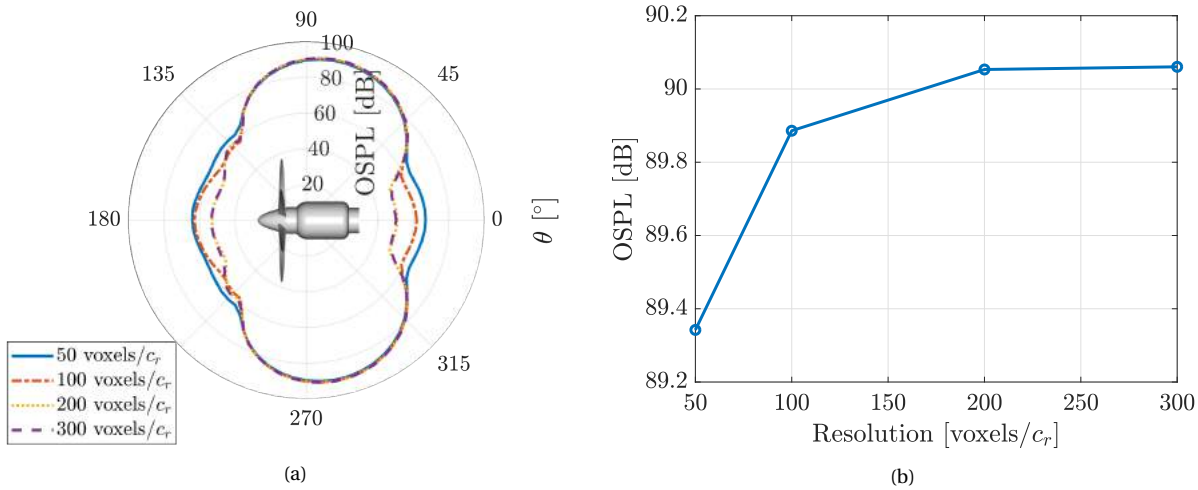

(a) (b)

Figure 4.2: Polar plot of the overall sound pressure level (OSPL) at a distance of $10D$ from the midpoint between propeller and SRVs in (a) and the OSPL at $\theta = 90°$ in (b). Obtained using grids with increasing resolution.

The convergence of the time-averaged axial and tangential velocity, circumferentially averaged into thirty radial intervals, at the location $x/D = 0.45$ in the isolated propeller slipstream is shown in Figure 4.3. The slipstream is not converged in the region of $0.4 < r/R < 0.5$ as the solutions of 200 and 300 voxels/c_r do not overlap in this region. The difference between the results obtained with the grid of 200 and 300 voxels/c_r becomes apparent when comparing the phase-averaged axial velocity in the plane $x/D = 0.45$, shown in Figure 4.4. A more detailed blade wake boundary is present in Figure 4.4b, which is concluded to be the cause of the difference between 200 and 300 voxels/c_r at $0.4 < r/R < 0.5$ in Figure 4.3. The notion that the smaller-scale structures are better resolved by the grid of resolution 300 voxels/c_r is confirmed by comparing the λ_2 isosurfaces in Figure 4.5.

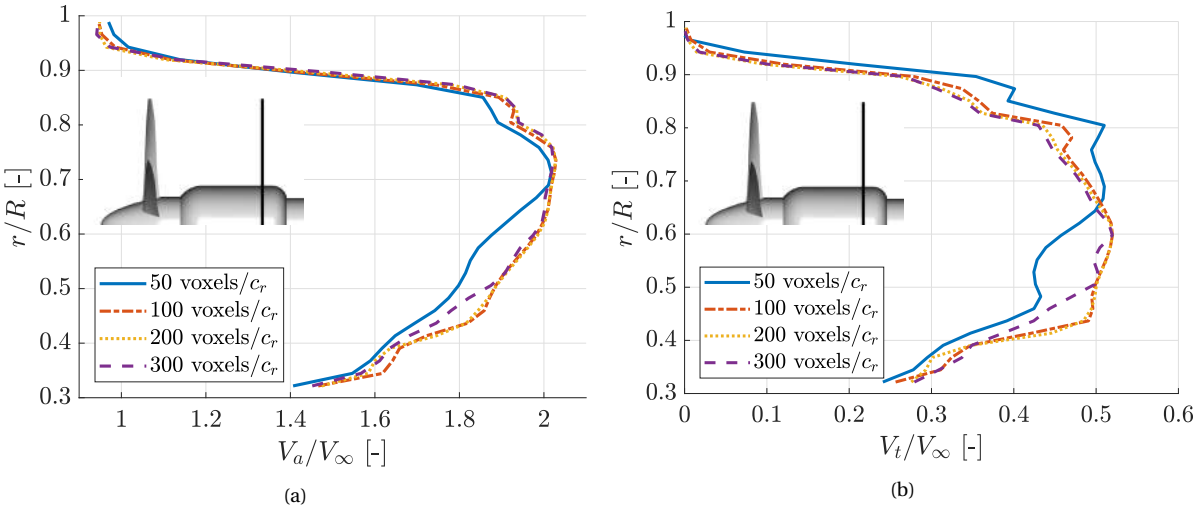

(a) (b)

Figure 4.3: Time- and spatially-averaged axial (a) and tangential velocity (b) in a plane downstream of the propeller at $x/D = 0.45$ for results obtained using grids of increasing resolution.

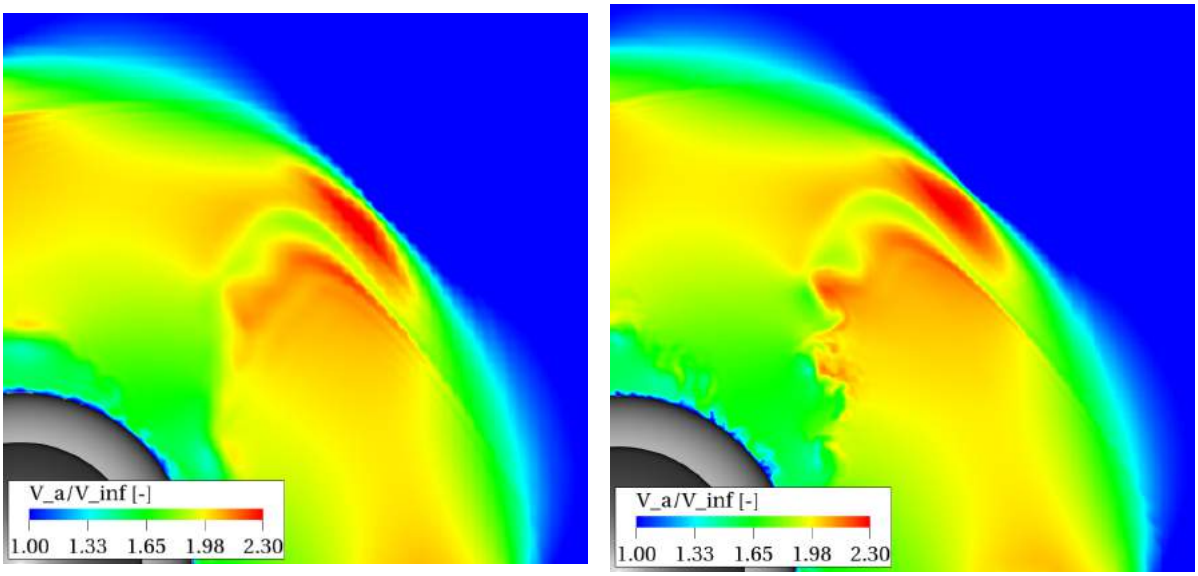

(a) (b)

Figure 4.4: Phase-averaged axial velocity in a plane downstream of the propeller at $x/D = 0.45$ for results obtained using grids with resolution of 200 voxels/c_r in (a) and 300 voxels/c_r in (b).

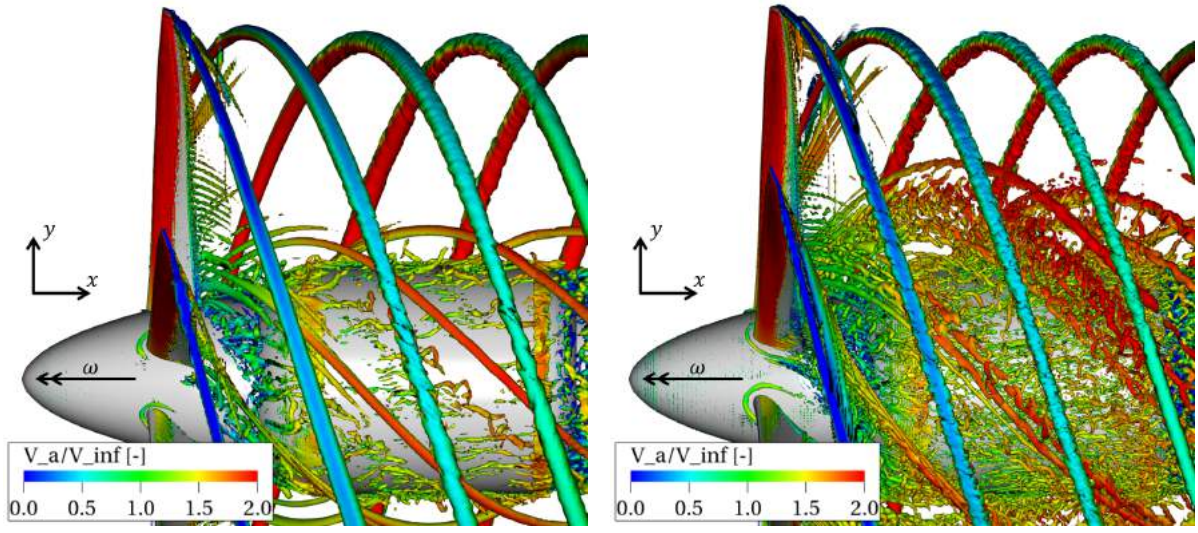

(a) (b)

Figure 4.5: Phase-averaged isosurface of $\lambda_2 = -3 \cdot 10^6$ s^{-2} coloured by the normalised axial velocity. Results are obtained using grids with resolution of 200 voxels/c_r in (a) and 300 voxels/c_r in (b). The propeller rotation direction is indicated by ω.

4.1.2. SRVs ON

Finally, convergence of the performance coefficients for the case with the SRVs installed (SRVs ON) are displayed in Figure 4.6. The $C_{T_{prop}}$ shows a similar trend as for the isolated propeller, see Figure 4.6a. The thrust produced by the SRVs for the various resolution cases is depicted in Figure 4.6b where the vane thrust is displayed with respect to the experimentally obtained propeller thrust coefficient $C_{T_{prop,exp.}}$. The vane thrust obtained from the load cells in the experiment is included as a means of comparison. The shaded area indicates the experimental error. A difference of 0.18 N (5.1%) in SRVs thrust exists between 200 and 300 voxels/c_r. The thrust distribution over a vane for the various resolution cases is presented in Figure 4.7 from which it can be concluded that the largest difference in vane loading between the grids with 200 and 300 voxels/c_r is located around $r/R = 0.5$. This corresponds to the location of maximum difference in inflow swirl angle,

shown in Figure 4.8. As concluded from Figure 4.4 and 4.5, many small-scale structure exist in this region which are better resolved by the grid with the resolution of 300 voxels/c_r.

The grid with a resolution of 200 voxels/c_r is herewith accepted and will be used in the remainder of this manuscript. It should be kept in mind that the aerodynamic slipstream small-scale structures in the region of $0.4 < r/R < 0.5$ are dependent on the grid which has an effect on the SRV thrust production at this location. The aeroacoustics and the effects around the tip of the vanes have been shown to be grid independent, which will be the areas of focus throughout this work.

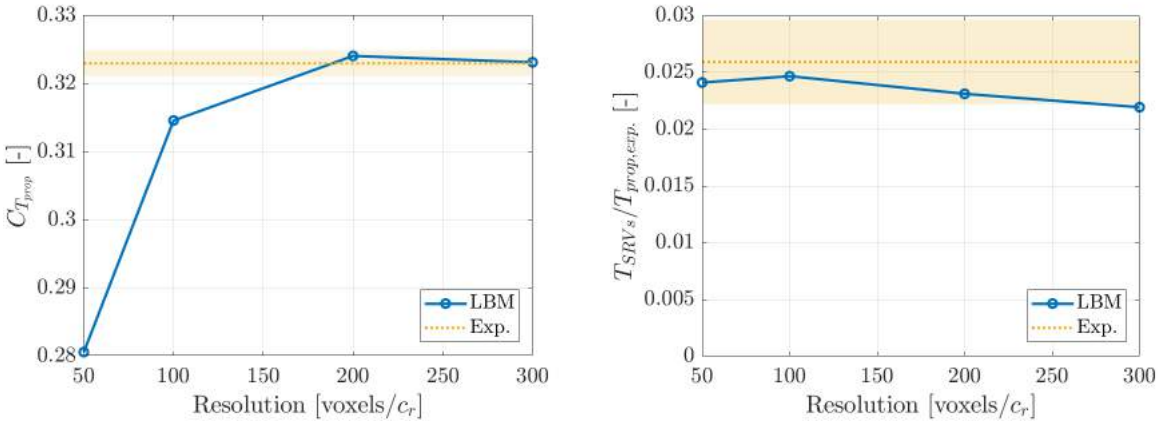

(a) (b)

Figure 4.6: Averaged propeller thrust in (a) and SRVs thrust with respect to the experimentally obtained propeller thrust $T_{prop,exp.}$ in (b). Values are obtained using grids with increasing resolution. Reference value from experiment is included together with the uncertainty error as a shaded area.

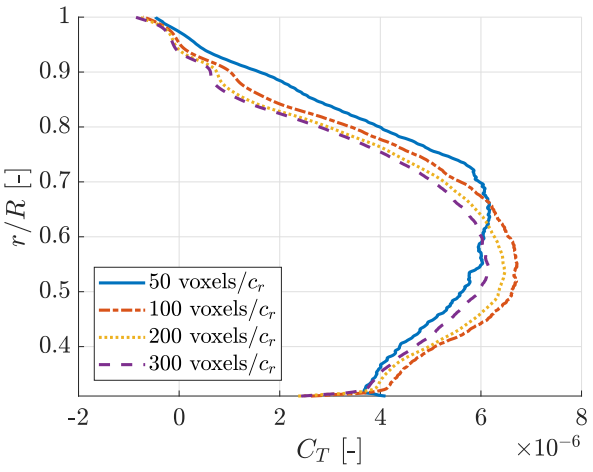

Figure 4.7: Time-averaged thrust distribution over a SRV expressed as C_T per segment for various resolution cases. 474 segments are used.

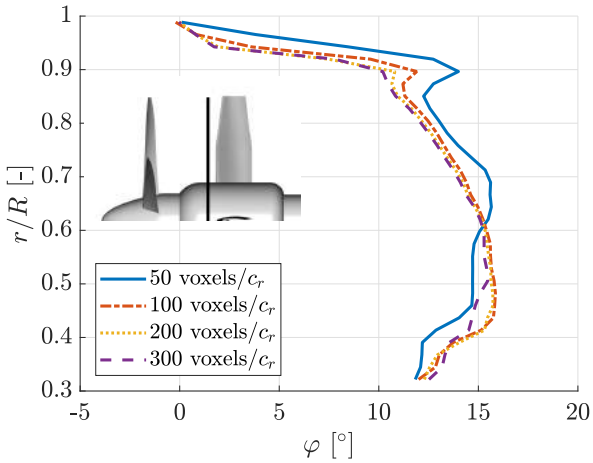

Figure 4.8: Time- and spatially-averaged swirl angle φ $0.4c_r$ upstream of the SRVs (i.e. $x/D = 0.24$) for various resolution cases.

4.2. Comparison with experimental and RANS data

4.2.1. SRVs OFF

A comparison with RANS (see Section 3.2) and experimental data, obtained using PIV as explained in Section 3.4, is performed using the axial and tangential velocity in two planes downstream of the isolated propeller. The outcome is presented in Figure 4.9 and 4.10, where the location of the measurement plane is indicated. The data has been time-averaged over three propeller revolutions and circumferentially averaged into thirty radial intervals. The uncertainty for the experimental data is indicated by a shaded yellow area. Good agreement between results obtained with the different methods is observed. A discrepancy is present between

LBM and RANS close to the fairing, i.e. $r/R < 0.4$. This is a consequence of the different implementation of the fairing radii, as explained in Section 3.3.

A local decrease in both the axial and tangential velocity is present in the LBM results around $r/R = 0.8$ in the plane at $x/D = 0.45$. The wake behind the propeller blades is deformed which causes it to be aligned with the propeller axis around $r/R = 0.8$, as is visible in Figure 4.11. The contribution of the wakes to the time-averaged results is therefore increased around that location. The local velocity dip is not visible in RANS, but is observed in the experimental results, although less distinct and at a lower radial location. A radial misalignment is also identified for the slipstream edge in the plane at $x/D = 0.45$ between experiment and LBM/RANS, visible in Figure 4.9b and 4.10b. If the slipstream edge is defined by $V_a/V_\infty = 1$, LBM predicts the edge to be at $r/R = 0.937$ whereas $r/R = 0.917$ follows from the experimental data.

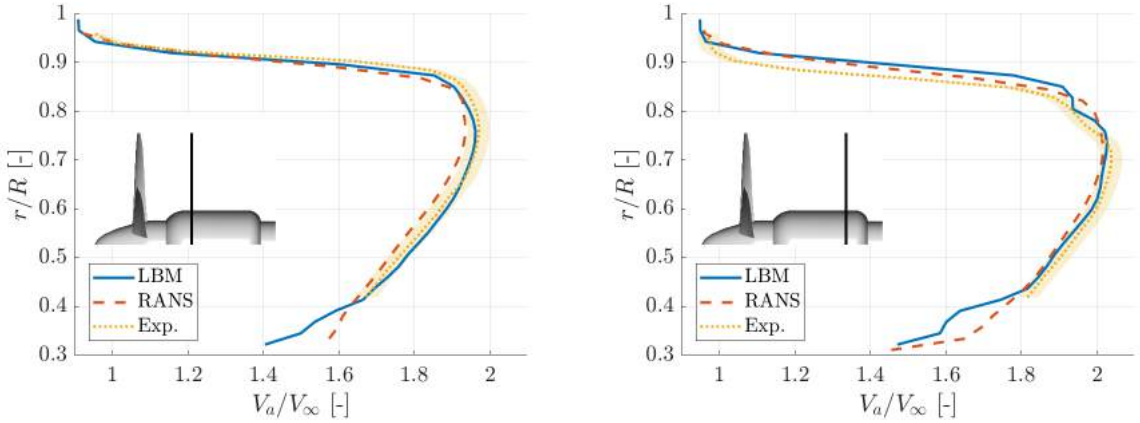

(a) (b)

Figure 4.9: Time- and spatially-averaged axial velocity in planes downstream of the propeller at $x/D = 0.24$ (a) and $x/D = 0.45$ (b) for results obtained with LBM, RANS and experiments.

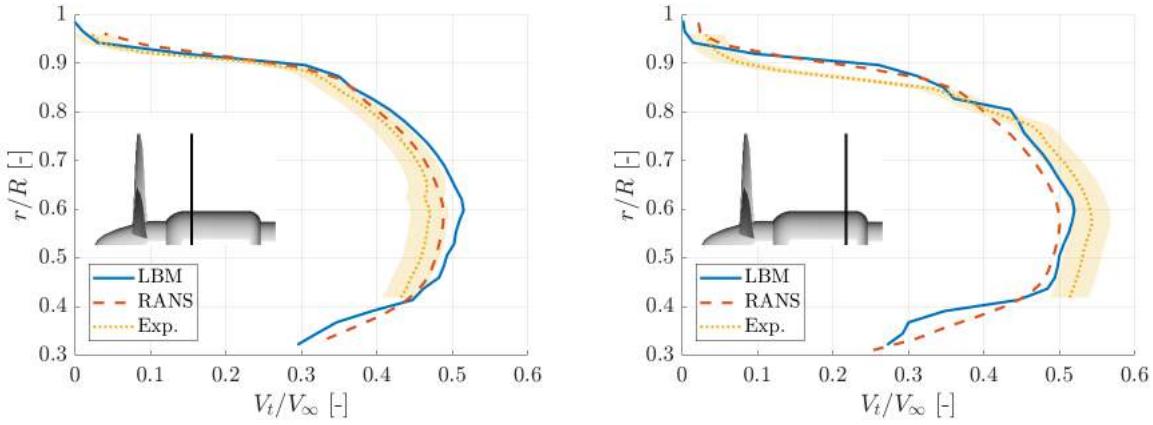

(a) (b)

Figure 4.10: Time- and spatially-averaged tangential velocity in planes downstream of the propeller at $x/D = 0.24$ (a) and $x/D = 0.45$ (b) for results obtained with LBM, RANS and experiments.

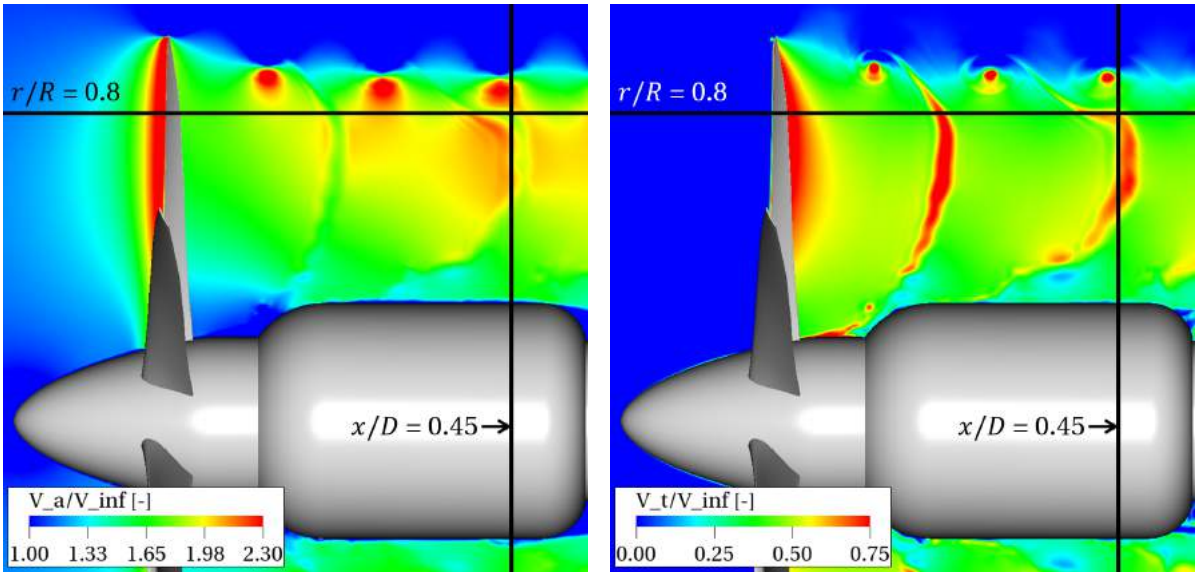

(a) (b)

Figure 4.11: Phase-averaged axial (a) and tangential (b) velocity in a plane at $z/D = 0$. The location of $r/R = 0.8$ and $x/D = 0.45$ are indicated.

A second comparison between the current LBM results and previously obtained RANS data is performed in terms of the pressure around the propeller blade. The normalised time-averaged static pressure at $r = 0.7R$ is plotted in Figure 4.12 against the location along the chord ζ, which is normalised by the local blade chord c. Good agreement is observed in the middle part. The maximum and minimum pressure are underpredicted by LBM which can be explained by a relative high y^+ ($y^+ = 30$ for VR12 in LBM at $r/R = 0.7$ compared to $y^+ = 1$ for RANS). The curvature around the leading edge is less well resolved by this coarser resolution causing the variation. The discrepancy at the trailing edge is caused by a different implementation of the geometry. The trailing edge is implemented as a smooth trailing edge in RANS and as a blunt trailing edge in LBM.

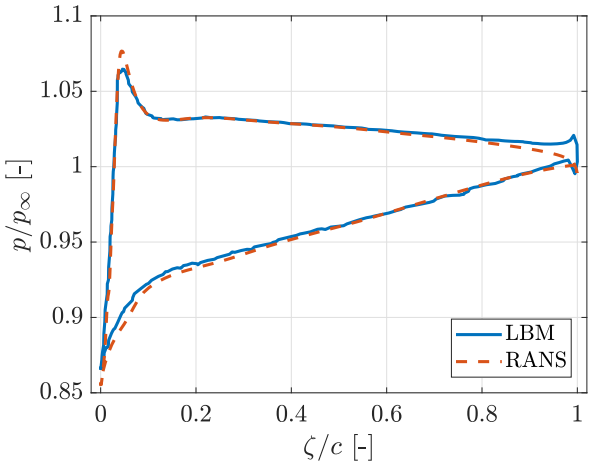

Figure 4.12: Time-averaged static pressure around a propeller blade at 70% of the radius.

4.2.2. SRVs ON

Finally, the slipstream velocity distributions are compared with experimental data for the SRVs ON case in Figure 4.13 and 4.14. The velocity distributions agree to a high degree in the plane at $x/D = 0.24$ as the LBM results are within the uncertainty margin of the experimentally obtained results. In the plane at $x/D = 0.45$, there is a clear misalignment in the location of the slipstream edge, which is slightly larger than for the SRVs OFF case. Again, defining the slipstream edge as the location where $V_a/V_\infty = 1$, the slipstream edge is located at $r/R = 0.941$ according to LBM and $r/R = 0.916$ according to the experiment.

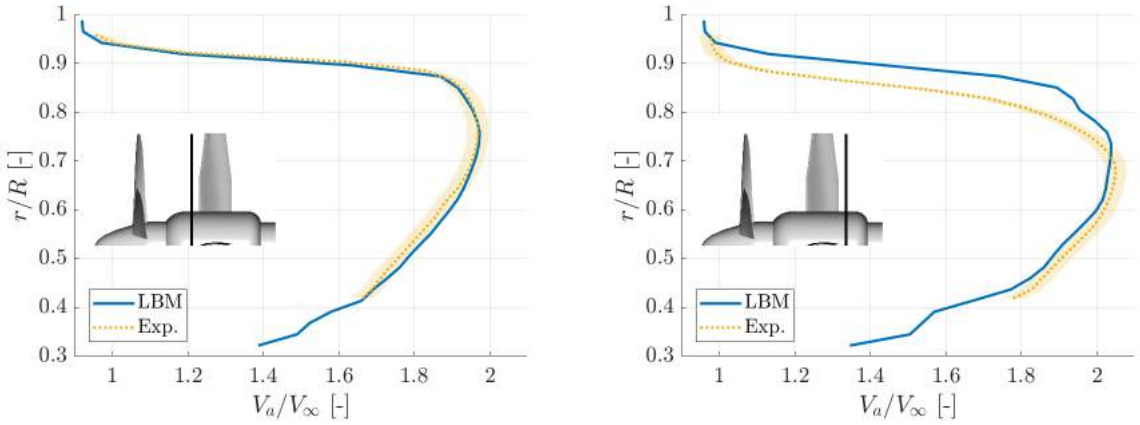

(a) (b)

Figure 4.13: Time- and spatially-averaged axial velocity in planes downstream of the propeller at $x/D = 0.24$ (a) and $x/D = 0.45$ (b) for results obtained with LBM, RANS and experiments.

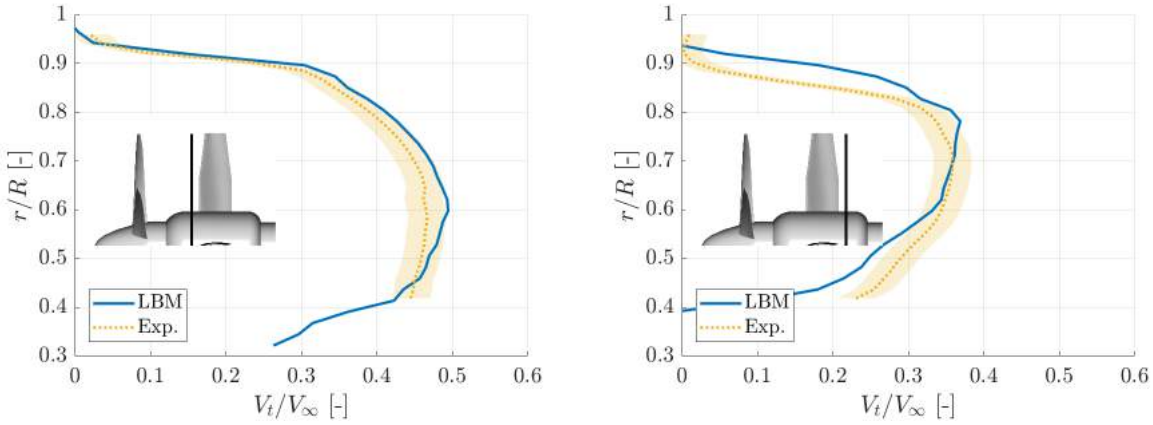

(a) (b)

Figure 4.14: Time- and spatially-averaged tangential velocity in planes downstream of the propeller at $x/D = 0.24$ (a) and $x/D = 0.45$ (b) for results obtained with LBM, RANS and experiments.

5

Results

The obtained results are split up into an aerodynamic and aeroacoustic part and are obtained for an operating condition of $V_\infty = 29$ m/s and $J = 0.6$, corresponding to take-off.

5.1. Aerodynamics

5.1.1. Performance coefficients

As the main objective of the SRVs is to produce thrust, the resultant forces acting on the propeller and SRVs are quantified by the time-averaged force coefficients. The thrust and torque coefficients, C_T and C_Q respectively, and the propulsive efficiency η are displayed in Table 5.1. The reader is referred to Section 2.2 for their definitions. The total efficiency η_{tot} is obtained using the total thrust coefficient which equals the sum of the propeller and SRVs thrust coefficients $C_{T_{tot}} = C_{T_{prop}} + C_{T_{SRVs}}$. The configuration with SRVs (SRVs ON) is compared to the isolated propeller (SRVs OFF) in Table 5.1.

Table 5.1: Time-averaged performance coefficients for the SRVs OFF and SRVs ON case.

	SRVs OFF	**SRVs ON**
$C_{T_{prop}}$	0.3235	0.3241 (+0.19%)
$C_{Q_{prop}}$	0.05459	0.05464 (+0.088%)
η_{prop}	0.5658	0.5664 (+0.10%)
$C_{T_{SRVs}}$	-	0.007464
η_{tot}	0.5658	0.5794 (+2.4%)

The SRVs produce an average thrust that equals 2.3% of the propeller thrust. Furthermore, the SRVs have a small upstream effect on the propeller, increasing the propeller loading and its efficiency. This opposes the findings of Dittmar & Hall [18] in which the propeller was seen to be unloaded with a propeller torque reduction of not more than 4%. Note that this experimental campaign was conducted using swept SRVs at distinct flight conditions.

The thrust generated by the SRVs fluctuates as can be seen from Figure 5.1a where instantaneous thrust coefficients are plotted versus time. Time is expressed as propeller rotation angle or phase angle ϕ. Although the fluctuations are small (0.24% of the propeller thrust), they could have an effect on the structural vibrations transmitted to the aircraft. A clear periodicity with a period of $\phi = 30°$ is observed. The propeller slipstream contains fluctuations with a period of 60° due to the presence of six propeller blades. Since there are four SRVs present, the slipstream fluctuations affect two of these SRVs simultaneously which causes a period of 30°. If for example five vanes would be applied, the magnitude of the vane thrust fluctuations is expected to decrease and their period would reduce to $\phi = 12°$. During every period of 30° in Figure 5.1a, the SRVs thrust shows a double peak, which will be explained in the next section.

In Figure 5.1b, a detail of Figure 5.1a is presented which is indicated by a rectangle. The propeller loading is seen to be more fluctuating when the SRVs are placed. This effect is small as the variations in thrust are 0.22 N or 0.047% for the SRVs ON case. As the SRVs are stationary, their upstream effect is likewise. The rotating propeller blades pass by the effect of the SRVs and are therefore periodically effected, causing the

observed fluctuations. This effect is periodic with a period of $\phi = 30°$, which can be recognised although the fluctuations caused by the inflow turbulence obscure the trend.

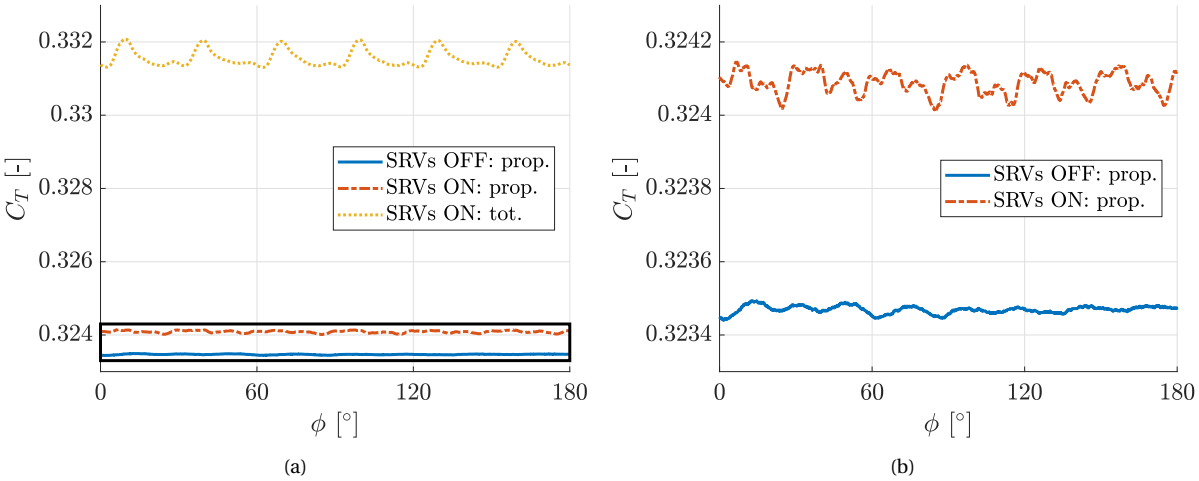

Figure 5.1: Thrust coefficient versus phase angle. Both the propeller-only and total thrust is illustrated for the SRVs ON case. (a) contains a rectangle which indicates the axis limits of (b).

The fluctuations in propeller torque are aligned with the variations in thrust, causing reduced fluctuations in propulsive efficiency of the propeller as this value is directly related to the quotient of thrust over torque. The fluctuations in η_{prop} are 0.015% for the SRVs ON case, compared to 0.047% for the variations in thrust. The instantaneous propulsive efficiency is presented in Figure 5.2 with the total efficiency for the SRVs ON case included in yellow.

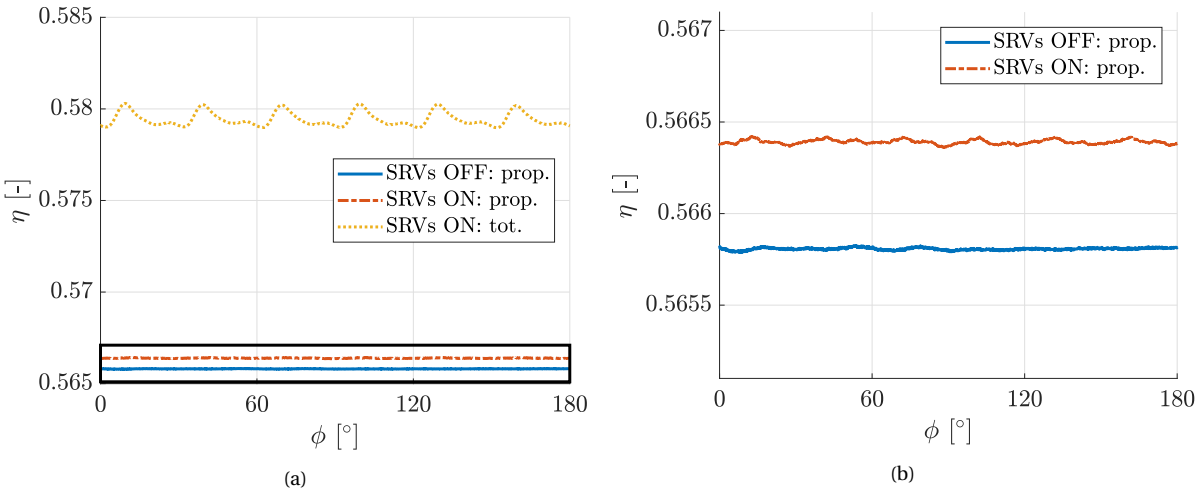

Figure 5.2: Propulsive efficiency versus phase angle. Both the propeller-only and total efficiency is illustrated for the SRVs ON case. (a) contains a rectangle which indicates the axis limits of (b).

5.1.2. Vane loading fluctuations

To investigate the fluctuating SRV thrust, the inflow angle is studied as it relates directly to the inflow angle of a SRV, as shown in Section 2.4. The instantaneous swirl angle φ is shown in two planes in Figure 5.3. Figure 5.3a contains a front view of a plane $0.4c_r$ upstream of the SRVs' LE (i.e. $x/D = 0.24$) and Figure 5.3b is a side view at $z/D = 0$. Six regions of high swirl can be identified in Figure 5.3a which are caused by the wakes behind the six propeller blades, as annotated. A reduced axial velocity and increased tangential velocity are observed in the blade wakes, which increase the swirl angle as defined in Section 2.2. The shape of these regions is dictated by the velocity distribution in the slipstream.

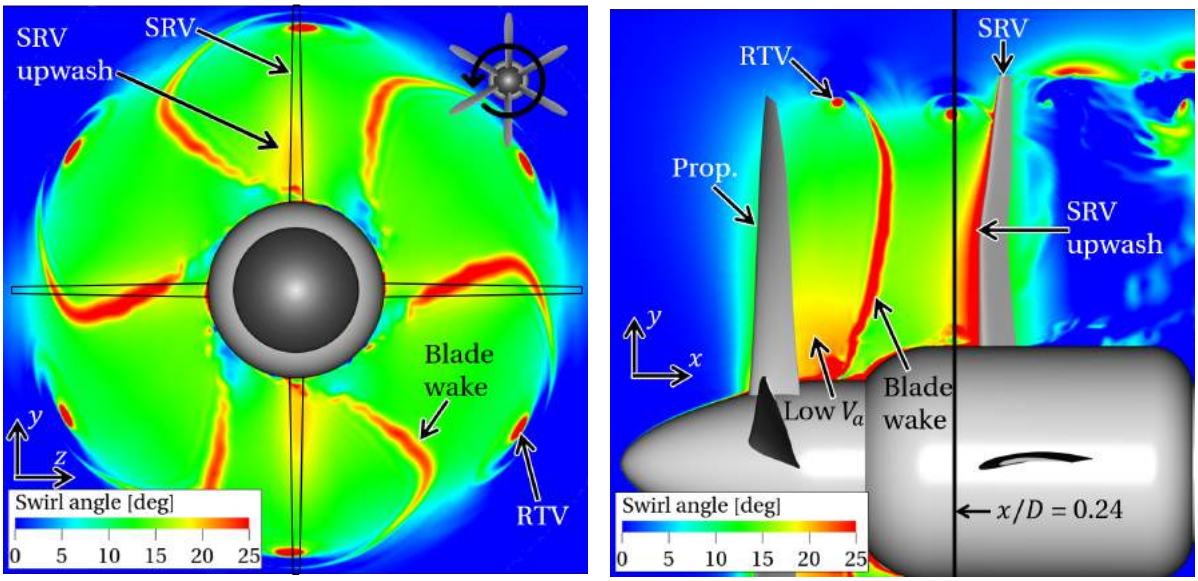

(a) (b)

Figure 5.3: Phase-averaged swirl angle φ in a plane $0.4c_r$ upstream of the SRVs (i.e. $x/D = 0.24$) in (a) and $y/D = 0$ in (b).

The presence of six propeller tip vortices or rotor tip vortices (RTVs) is indicated in Figure 5.3a. The RTVs consist of circular regions of high swirl, as a consequence of the high tangential velocity present in the vortices. As can be concluded from Figure 4.9 and 4.10, both the axial and tangential velocity reduce in the outboard slipstream region ($r/R > 0.8$). Together with the longer outboard circumference, this causes the RTVs to have travelled a reduced angular distance from the propeller plane to the current plane at $x/D = 0.24$ compared to the wake flow at mid-span. The RTV therefore trails the blade wake and together with the partly-sweeped leading edge of the SRV, this ensures that it affects the SRV just before the wake of the subsequent propeller blade.

Moreover, behind the propeller close to the spinner, a region of high swirl is present due to the low axial velocity between propeller and fairing, indicated in Figure 5.3b by "Low V_a". Finally, four regions of high swirl can be identified at the angular locations of the SRVs. As the SRVs are lifting surfaces, an upwash is present which causes a local increase of the tangential velocity and the swirl angle accordingly. As this upwash is stationary and the blade wakes are rotating with the flow, a periodic positive interference occurs. The swirl angle is increased when a blade wake overlaps with the SRV upwash as can be seen at the locations of the horizontal SRVs in Figure 5.3a.

Since the patterns of high swirl constituting of the blade wakes and RTVs presented in Figure 5.3 are rotating with the tangential velocity, the SRVs encounter a varying inflow angle. The swirl angle at $r/R = 0.7$ and $0.4c_r$ upstream of the upward-pointing vane (positive y-direction) is shown with respect to phase angle in Figure 5.4. Sharp peaks in swirl angle are present of over $\varphi = 25°$ which are caused by the periodic impingement of the blade wakes, amplified by the SRV upwash as described before. Henceforth, any analysis performed on a single vane is taken with respect to this upward vane.

The effect of the varying inflow angle on the SRVs can be derived from the time trace of the thrust coefficient of the upward vane $C_{T_{vane}}$, included in Figure 5.4 in red. Double peaks in thrust are present of which the first smaller peak is caused by the impingement of a RTV. The larger peak which is 20% higher than the average (indicated in Figure 5.4) is a result of the increased swirl angle in the wake of the subsequent propeller blade, which follows the peak in swirl angle at $r/R = 0.7$. As explained, the RTV impinges later than the wake of a blade as a result of the low velocity at the slipstream edge and the SRV shape. The point of maximum vane thrust is followed by a minimum of 9% under the average value, which corresponds to the area of moderate swirl ($\varphi = 16°$).

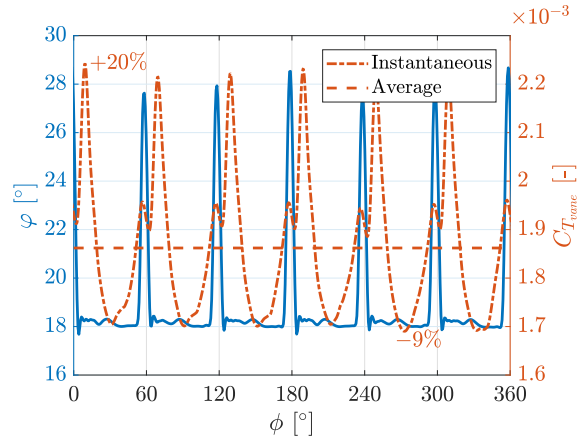

Figure 5.4: Swirl angle φ at $r/R = 0.7$ and $0.4c_r$ upstream of the upward vane (i.e. $x/D = 0.24$) shown in blue. Instantaneous thrust coefficient of the upward vane indicated as dash-dotted line in red with the average value as red dotted line.

To inspect whether stall occurs on the vane, pressure plots around the upward vane at $r/R = 0.7$ for three time instants at and after the time of maximum vane thrust are included in Figure 5.5. These traces show a continuous pressure recovery on the aft part of the suction side to a value above p_∞ without the occurrence of a pressure plateau. This proves that no static stall occurs at $r/R = 0.7$ [3]. As there is no abrupt decrease of the suction peak and no moving pressure unevenness on the suction side, which would indicate the passage of the primary and secondary vortices, it is concluded that there is also no dynamic stall present [39]. The small pressure drop at $\zeta/c = 0.17$ overlaps with the resolution transition from VR12 to VR11, which is expected to be the cause of this unevenness.

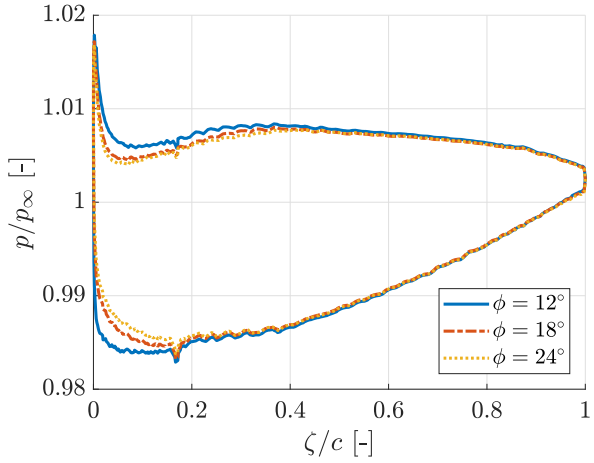

Figure 5.5: Phase-averaged static pressure around the upward vane at $r/R = 0.5$ and $r/R = 0.7$ at the time of maximum $C_{T_{vane}}$.

5.1.3. Vane loading distribution

After examining the time dependency of the total SRVs thrust, the variation of the thrust distribution with time is investigated. The thrust coefficient distribution over the upward vane is shown for six time instants in Figure 5.6 to examine. The middle region ($0.4 < r/R < 0.8$) varies with the variation in inflow angle caused by the rotating blade wakes. The location of maximum thrust moves with time as a consequence of the blade wake shape, visible in Figure 5.3a. The peak in inflow angle starts outboard and proceeds inboard which causes the location of maximum thrust to move accordingly from $r/R = 0.6$ at $\phi = 6°$ to $r/R = 0.5$ at $\phi = 18°$.

The tip region ($r/R > 0.8$) fluctuates in thrust due to impingement of the RTVs. The RTV impinges the leading edge at $\phi = 54°$ which causes a clear positive peak in the thrust distribution around $r/R = 0.91$. This peak is attenuated, after which the tip starts producing negative thrust for $\phi = 18°$ and $\phi = 30°$. The location of $r/R = 0.91$ is indicated in Figure 5.6 by a black dashed line. The tip of the vane is further analysed in Sections 5.1.6 and 5.1.7.

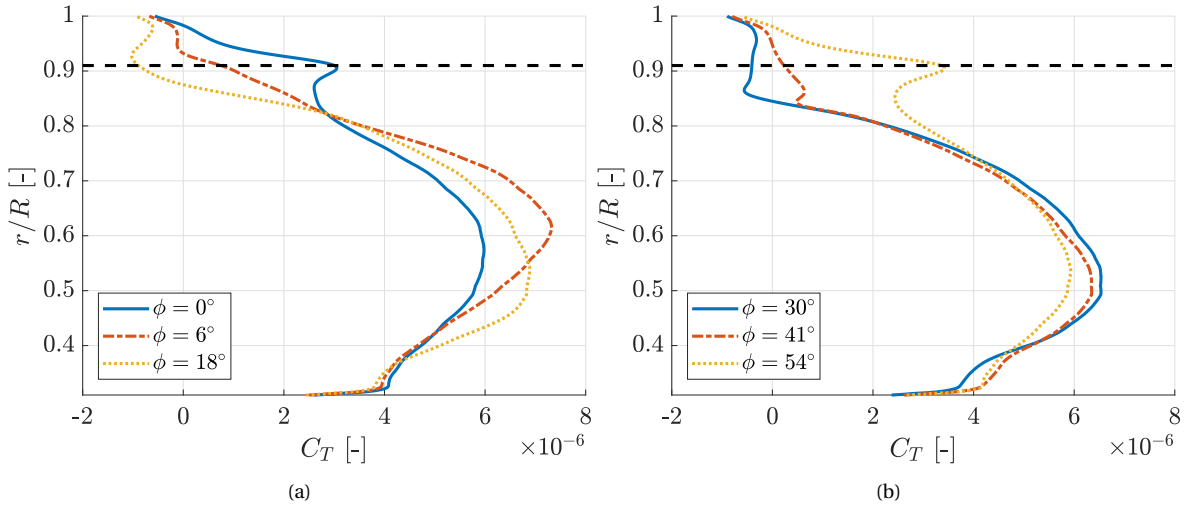

Figure 5.6: Phase-averaged thrust distribution over the upward SRV for various phase angles expressed as C_T per segment (474 segments are used). The black dashed line indicates $r/R = 0.91$.

5.1.4. Swirl reduction

Swirl recovery vanes exploit the swirl present in the propeller slipstream to generate additional thrust, thereby reducing the slipstream swirl. The axial development of the swirl angle is presented in Figure 5.7, where the swirl angle is averaged over time and over a spatial region of $0.31 < r/R < 1$. A clear reduction of 48% in swirl can be observed when the SRVs are installed, when comparing values averaged from $x/D = 0.43$ to $x/D = 1$. A swirl reduction of 42% was obtained in the experimental campaign [33]. The reduction is present in the area where the SRVs are located, indicated by the dashed black lines. The downstream effect of the SRVs is concluded to be negligible and a minor upstream effect is present. As explained in Section 5.1.2, the upwash in front of the vanes acts in the same direction as the swirl, such that an increase in swirl angle of 0.2° is observed in front of the vanes. Due to the "Low V_a" region indicated in Figure 5.3b, there is an area of high swirl present close to the propeller and spinner for both the SRVs OFF and SRVs ON case. This effect decreases with distance from the propeller which causes the averaged swirl angle to reduce for $x/D < 0.2$. There is still a substantial swirl left in the slipstream behind the vanes such that it could be beneficial to apply more vanes, as already suggested by lifting line theory [33].

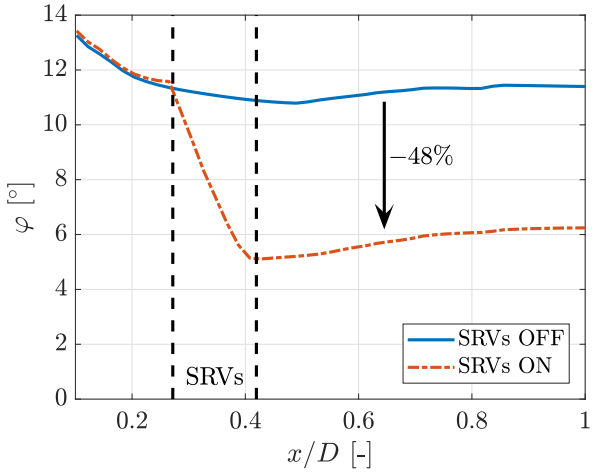

Figure 5.7: Development of the average swirl angle for the SRVs OFF and SRVs ON case. The SRV's LE and TE location are indicated by the dashed lines.

This residual swirl behind the SRVs is further examined by plotting the phase-averaged swirl angle in a plane $0.4c_r$ downstream of the SRVs at $x/D = 0.45$ in Figure 5.8a. The blade wakes and RTVs are still visible as regions of high swirl angle and also in between the blade wakes, a positive swirl angle is present. This swirl angle is quantified in Figure 5.8b at the location of the cross in Figure 5.8a, comparing the planes at $x/D =$

0.24 and $x/D = 0.45$. It can be concluded that there is a substantial residual swirl present at this location in between two SRVs at $r/R = 0.7$. Behind the SRVs however, the swirl is fully recovered with a swirl angle which fluctuates not more than 1.5° around 0° at $x/D = 0.45$ and $r/R = 0.7$, as is visible in Figure 5.8a. Furthermore, as annotated in Figure 5.7, the stator tip vortices (STVs) can be distinguished as regions of high swirl and RTV bridging occurs which will be explained further in Section 5.1.5.

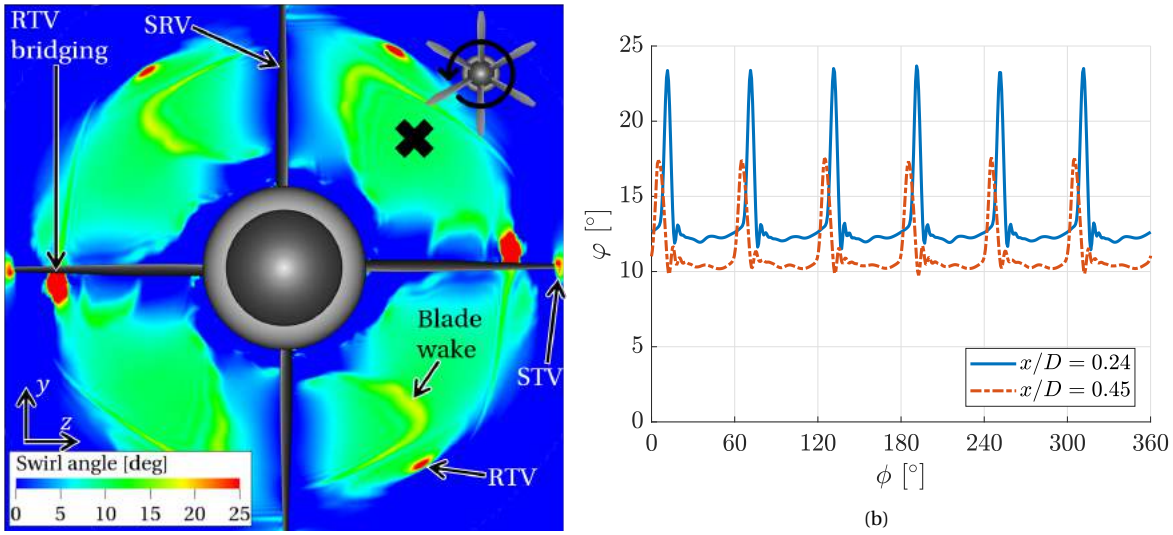

(a) (b)

Figure 5.8: Phase-averaged swirl angle φ in a plane $0.4c_r$ downstream of the SRVs (i.e. $x/D = 0.45$) in (a) where the propeller blades are hidden. Swirl angle versus phase angle in (b) for two axial locations at $r/R = 0.7$ in between two SRVs, as denoted by the cross in (a).

5.1.5. Instantaneous flow features

Vortices are visualised to increase the understanding of the slipstream behaviour when the SRVs are installed. This is done using the λ_2-method, which is based on the eigenvalues of a quadratic summation of the symmetric and antisymmetric part of the velocity gradient tensor [26]. A phase-averaged isosurface of λ_2 is presented in Figure 5.9, coloured by the normalised axial velocity. The rotor tip vortices (RTVs) can be seen to move inboard together with the contraction of the slipstream. The RTVs are located at the slipstream edge as the axial velocity drops over the λ_2 isosurfaces. Note that the small-scale structures at the root are shown to be dependent on the grid resolution in Section 4.1.1, such that the slipstream results in this region can not be trusted.

The trajectories of the RTVs over the vane are seen to be misaligned with the flow direction in Figure 5.10, where a close-up of the upward vane is presented for three time instants. The RTVs impinge on the vanes at $r/R = 0.91$ and are then sheared in spanwise direction: the RTVs at the pressure side move outboard and at the suction side inboard, as denoted in Figure 5.10 by a dashed and solid arrow, respectively. When leaving the vane, the two misaligned vortices interact and start forming bridges between them. As explained in Section 2.6, this situation relates to a configuration of a propeller with trailing wing, for which this phenomenon is investigated in detail by Johnston & Sullivan [28].

To change perspective, top views of the λ_2 isosurfaces around a region of the upward vane (i.e. $r/R > 0.65$) are shown in Figure 5.11. The RTVs are stretched on the suction side (SS) and thickened on the pressure side (PS), also explained in Section 2.6. On the SS, a second vortex is formed which starts rotating around the existing vortex. Inboard of the RTVs, a region of $\lambda_2 = -3 \cdot 10^6$ s^{-2} is visible which is attributed to the edge of the blade wakes where a high velocity gradient is present.

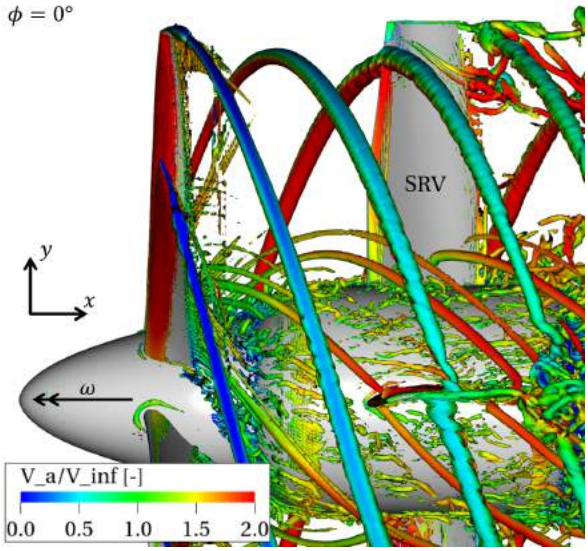

Figure 5.9: Phase-averaged isosurface of $\lambda_2 = -3 \cdot 10^6$ s^{-2} coloured by the normalised axial velocity. The propeller rotation direction is indicated by ω.

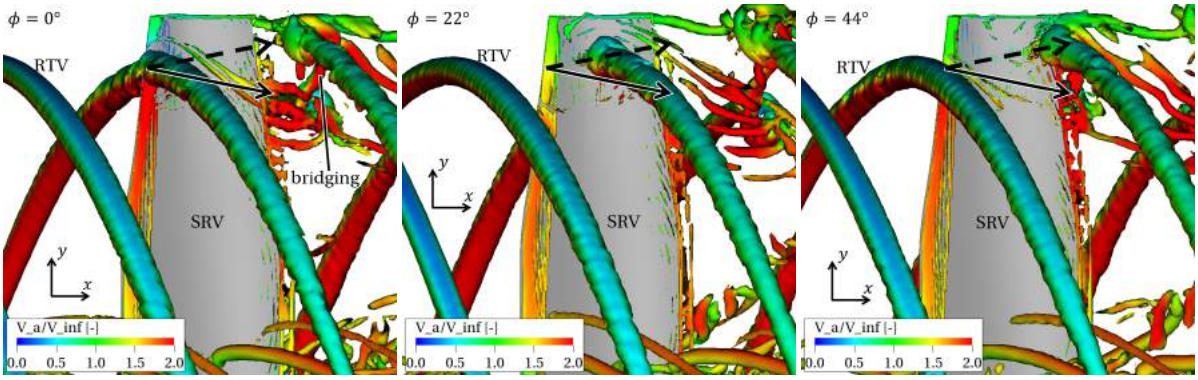

(a) (b) (c)

Figure 5.10: Close-up of the pressure side of the upward vane with the phase-averaged isosurface of $\lambda_2 = -3 \cdot 10^6$ s^{-2} for three time instants. The isosurface is coloured by the normalised axial velocity and a dashed arrow indicates the RTV direction on the pressure side and a solid arrow on the suction side.

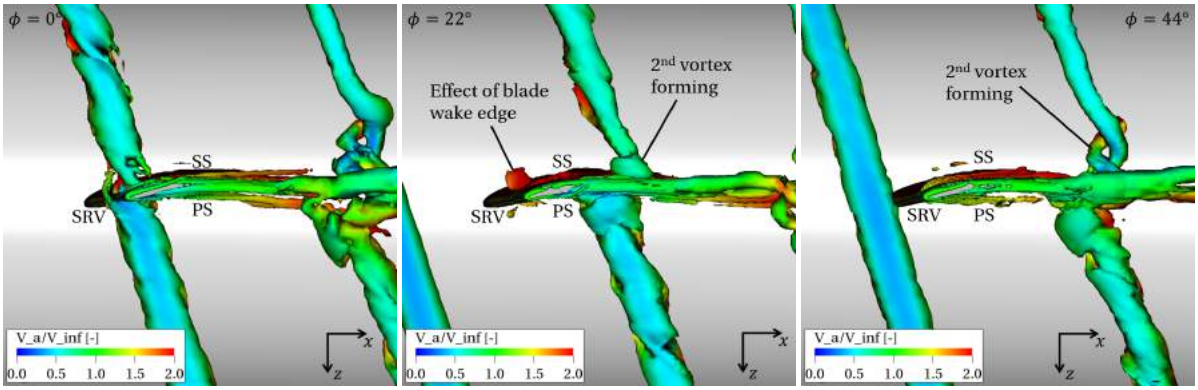

(a) (b) (c)

Figure 5.11: Top view of the phase-averaged isosurface of $\lambda_2 = -3 \cdot 10^6$ s^{-2} for three time instants. The isosurface is coloured by the normalised axial velocity and shown for the region of $r/R > 0.65$.

5.1.6. Thrust produced by the tip of the vane

As seen in Section 5.1.3, the tip region of the vane has a different behaviour compared to the rest of the vane. In order to define a region as the vane tip, the trajectories of the RTVs along the pressure side (PS) and suction side (SS) of a vane are shown in Figure 5.12. Points of minimum phase-averaged surface static pressure are located for ten time steps and linked together. The x-location is normalised by the root chord of the SRVs $c_{r,SRVs}$ where 0 indicates the location of the leading edge at the root of the SRVs. The distinctive RTV motion is clearly present from which the RTVs are concluded to affect the part of the vane where $r/R > 0.84$. This area will be denoted as the tip of the vane henceforward. $r/R = 0.84$ is indicated in Figure 5.12 together with the location where the RTVs impinge the leading edge ($r/R = 0.91$).

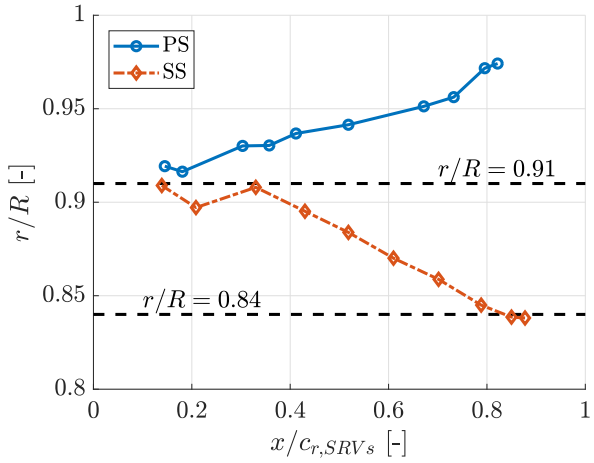

Figure 5.12: RTV trajectories along the pressure side (PS) and suction side (SS) of a vane. Determined by linking points of minimum phase-averaged pressure.

The aerodynamic effects around the vane tip will be investigated by starting with a similar analysis as performed in Section 5.1.2. The swirl angle at $r/R = 0.91$ and $0.4c_r$ upstream of the upward vane is shown with respect to phase angle in Figure 5.13. Strong peaks in swirl angle are present of over $\varphi = 50°$ which are caused by the RTVs and are double in magnitude compared to the swirl angle peaks due to the blade wakes at $r/R = 0.7$ (Figure 5.4). The swirl angle in the RTVs is therefore concluded to be higher than in the wakes of the blades. Smaller peaks of $\varphi = 17°$ are present in between the larger peaks which are caused by the propeller blade wake, visible in Figure 5.3a.

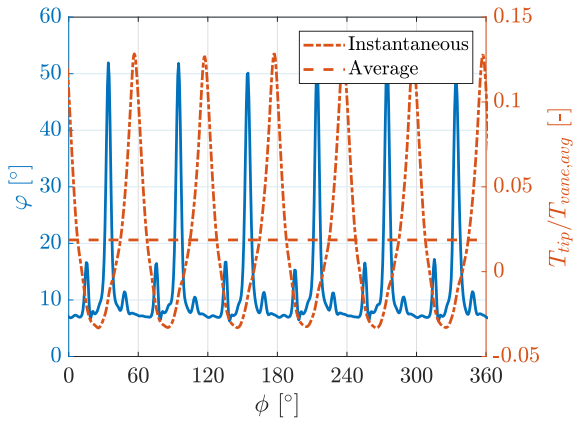

Figure 5.13: Swirl angle φ at $r/R = 0.91$ and $0.4c_r$ upstream of the upward vane (i.e. $x/D = 0.24$) shown in blue. Instantaneous thrust generated by the vane's tip ($r/R > 0.84$) T_{tip} normalised by the average thrust of the upward vane $T_{vane,avg}$ indicated as dash-dotted line in red with the average value as red dotted line.

The effect of the impingement of the RTVs on the thrust of the vane tip is included in Figure 5.13. The instantaneous thrust generated by the tip is normalised by the averaged total thrust generated by the upward vane and is displayed as a dash-dotted red line in Figure 5.13. As expected, the positive peaks in thrust overlap

with the smaller peaks in Figure 5.4. Note that the vane tip produces negative thrust and thus drag in between these positive peaks. On average, the tip contributes to 1.9% of the total thrust of the vane (dashed red line in Figure 5.13) while constituting to 19% of the vane's surface area. The relatively low velocity in the outer region of the propeller slipstream is identified as the cause of the low thrust. It should be noted that the presence of the tip can still have a substantial effect on the thrust distribution of the rest of the vane.

In order to investigate the possible occurrence of stall at the vane tip, the pressure distribution around the vane at $r/R = 0.91$ is shown in Figure 5.14 for three time instants at and after the peak in thrust generated by the vane's tip. As indicated in Figure 5.14, there is a small region of stall present at the trailing edge for $\phi = 54°$ as can be deducted from the presence of a pressure plateau with a pressure above p_∞ at the suction side [3]. It is however expected that this will have minimal effect on the SRV performance due to the small area it affects. No further indications (described in Section 5.1.2) of static or dynamic stall are noticeable, despite the high inflow angle of over 50°. This can be explained by the relatively small size of the area of high swirl within the RTV, as can be seen in Figure 5.3. The performance of the tip could be increased when the airfoil around $r/R = 0.91$ is designed to maximise the thrust from the impingement of the high swirl area, as this is neglected in the current design method using lifting line theory.

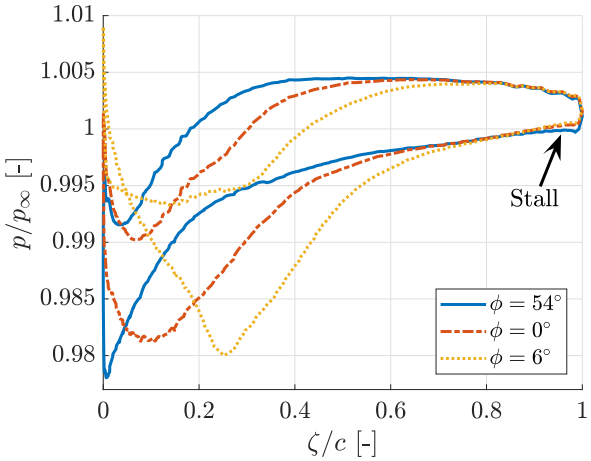

Figure 5.14: Phase-averaged pressure around the upward SRV at $r/R = 0.91$ for three phase angles.

5.1.7. Aerodynamic effects around the tip of the vane

The effect the RTVs have on the tip surface of the vanes will be investigated. The surface thrust force, combining the pressure and skin friction force, around the pressure side (PS) and suction side (SS) of the tip region of the upward vane are presented for four time instants in Figure 5.15. Static pressure contours are included where every contour indicates a pressure step equal to $0.0005 p_\infty$. The location of $r/R = 0.84$ is indicated by a purple line. The RTV can be traced such that its spanwise motion becomes apparent. The pressure contours around the RTV can be seen to expand on the PS and to condense on the SS during the development. This is caused by the thickening of the RTV on the PS and the stretching on the SS as observed in Section 5.1.5. After being stretched on the SS, a second vortex is formed which starts rotating around the existing vortex. This can be deducted from the pressure contours in Figure 5.15h and from the λ_2 isosurfaces in Figure 5.11.

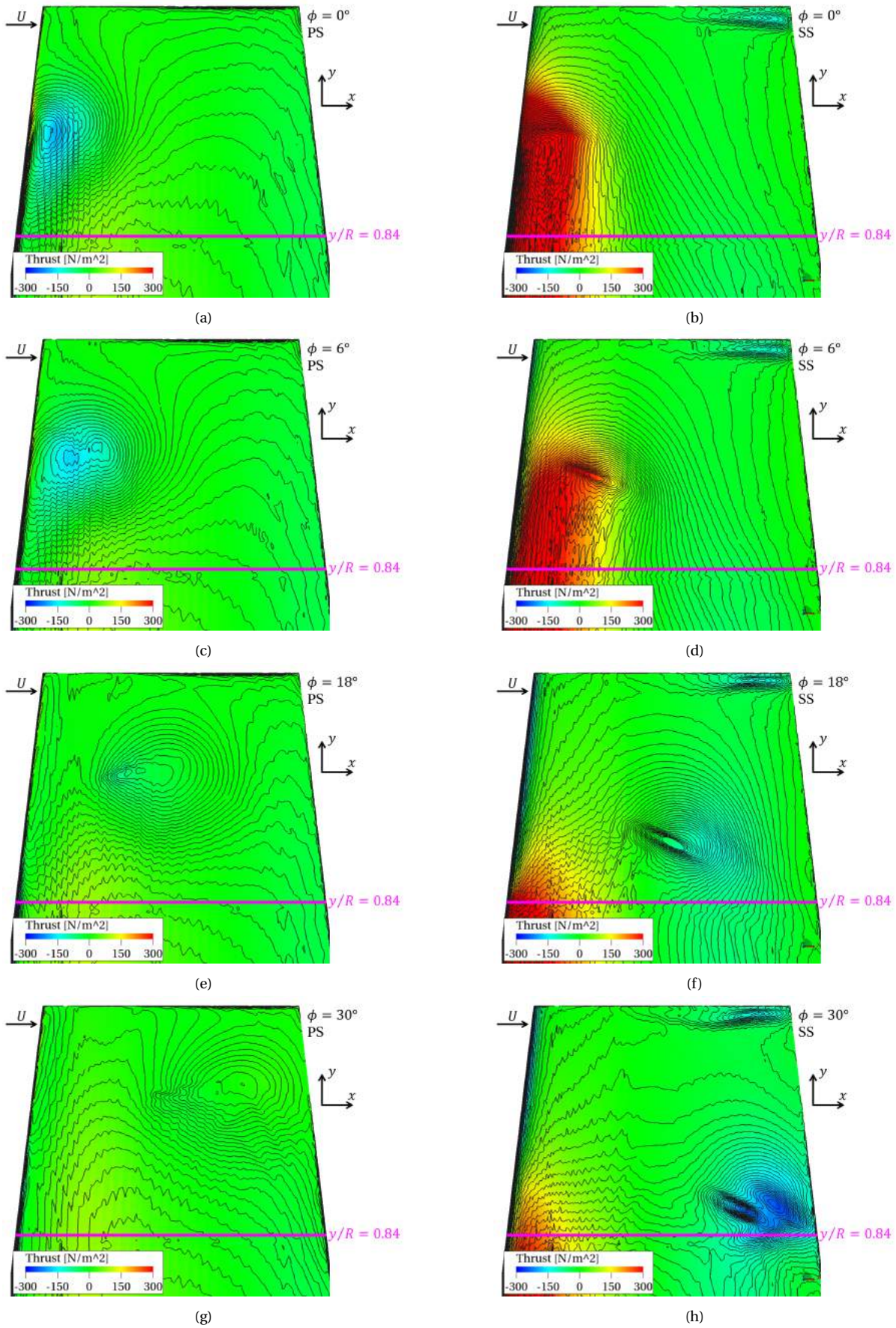

Figure 5.15: Phase-averaged surface thrust force on the pressure and suction side of the tip of the upward vane with pressure contours in black for three time instants where every contour indicates a pressure step equal to $0.0005 p_\infty$. $r/R = 0.84$ is indicated by a purple line and the direction of inflow velocity U is included (radial component of the velocity is neglected).

After the moment the RTV impinges, a large area of thrust is induced around the leading edge on the SS at $\phi = 0°$ and $\phi = 6°$ (Figure 5.15b and 5.15d). This causes the peaks in thrust in Figure 5.13 as is expected from the impingement of the area of high swirl angle associated to the RTV. The vortex core causes an area of drag for $\phi = 0°$ and $\phi = 6°$ on the PS (Figure 5.15a and 5.15c). This can be explained by the shape of the airfoil which is shown for $r/R = 0.91$ in Figure 5.16. There is a difference in surface angle at the PS and SS and as the low-pressure RTV cores cause a net outward-pointing normal force, the direction of this force also varies. This is shown by orthogonal arrows for two locations along the chord in Figure 5.16. When the RTV is situated close to the leading edge, the net normal force on the PS has a positive x-component which causes drag. On the SS, it has a negative x-component and thrust is generated. This effect is visible in Figure 5.15a and 5.15c and in Figure 5.15d by the deformation of the thrust area. As the RTV progresses, a drag force is caused on the SS, clearly visible for $\phi = 30°$ in Figure 5.15h. Due to the broadening of the RTV on the PS, no noticeable effect due to the RTV's core pressure on the surface thrust is present on the PS for $\phi = 30°$ (Figure 5.15g). Note that pressure drag originating from the stagnation point and viscous drag are continually present.

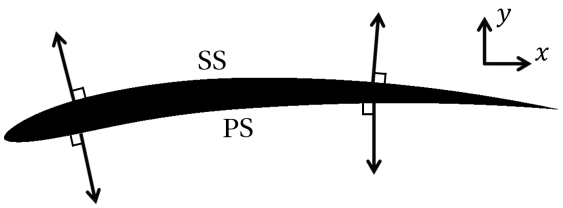

Figure 5.16: Cross section of a vane at $r/R = 0.91$ with the net forces caused by the RTVs indicated.

The axial velocity around the pressure side (PS) and suction side (SS) is presented for four time instants in Figure 5.17. The RTVs have a counterclockwise motion which increases the axial velocity at the bottom, decreasing the pressure, and reduces the axial velocity at the top, increasing the pressure. The effect on the pressure can be deducted from the shape of the pressure contours in Figure 5.17. The effect of the axial velocity on the pressure is more pronounced at the suction side due to reduced core size.

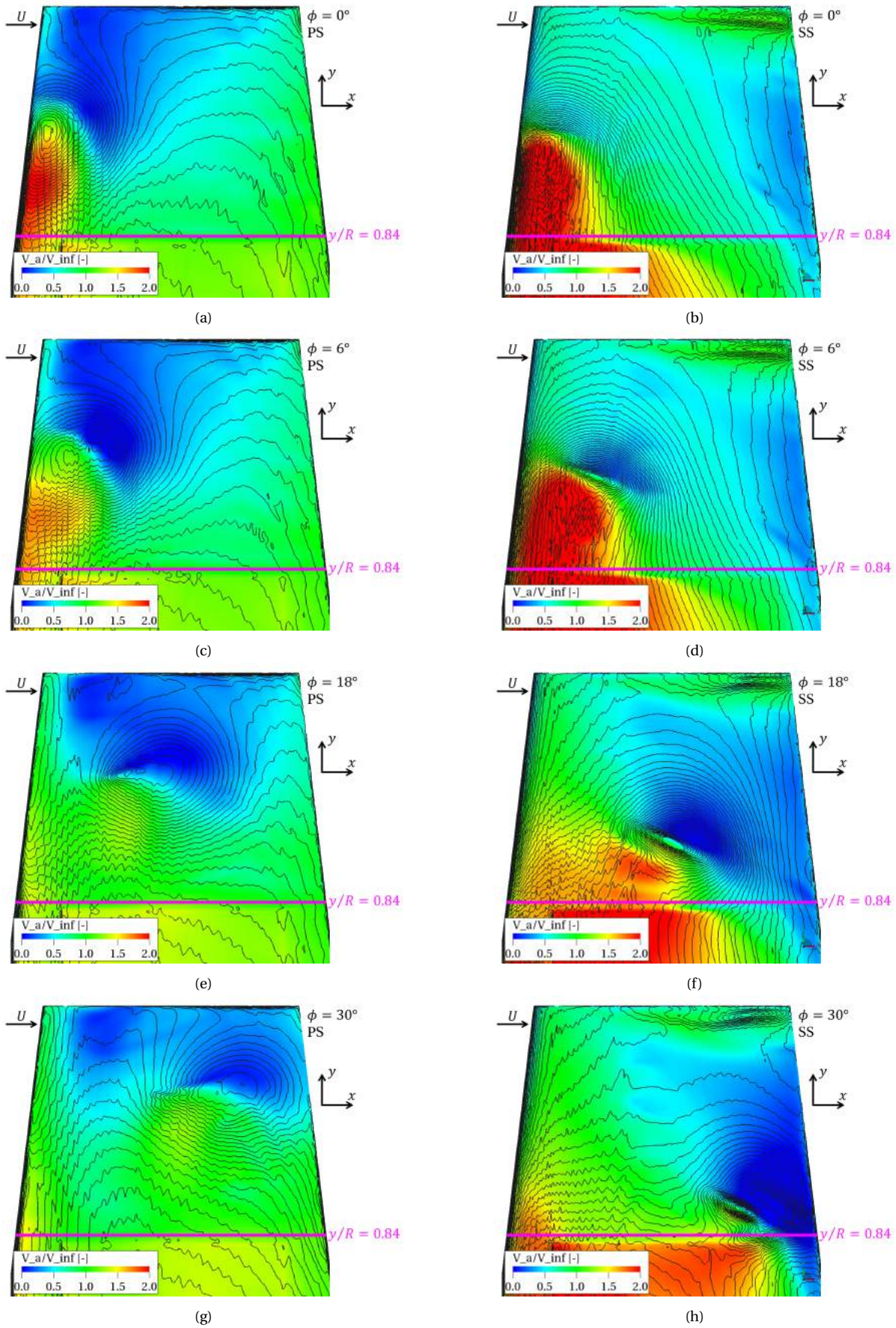

Figure 5.17: Phase-averaged axial velocity on the pressure and suction side of the tip of the upward vane with pressure contours in black for four time instants where every contour indicates a pressure step equal to $0.0005 p_\infty$.. $r/R = 0.84$ is indicated by a purple line and the direction of inflow velocity U is included (radial component of the velocity is neglected).

5.2. Aeroacoustics

5.2.1. Sound pressure in the far-field

The aeroacoustic performance of the two configurations (with and without SRVs) is analysed using the FW-H method as described in Sections 3.1.2 and 3.1.4. In Figure 5.18a the OSPL is plotted over the described ring with a radius of $10D$ and centred at the midpoint between propeller and SRVs. The sound pressure contributions of the propeller and SRVs are shown as the contributions of the spinner, fairing and nacelle are seen to be relatively small and therefore omitted. Note that the OSPL is expressed using a logarithmic scale. The propeller contribution of the SRVs OFF case shows a typical noise pattern of a propeller with two distinct side lobes slightly tilted in the downstream direction [37]. The side lobes would be tilted more downstream if the body or fluid velocity would be incorporated in the FW-H formulation. The propeller is affected by the placement of the SRVs as it emits more noise in up- and downstream direction than in the SRVs OFF case.

It can be concluded that the maximum total OSPL is unaffected due to the addition of the SRVs. The contribution of the propeller is dominant in the region of maximum OSPL and overlaps with the SRVs OFF case. The contribution of the vanes is more uniformly distributed along all directions making it a dominant noise source up- and downstream of the propeller. The total OSPL has increased upstream in a range of $\Delta\theta = 90°$ by up to 18.1 dB and downstream in a range of $\Delta\theta = 130°$ by up to 20.7 dB due to the presence of the SRVs. It should be noted that destructive interference occurs between the contributions of the various propeller blades in this idealised situation. An isolated propeller in real-life conditions with non-axial inflow of higher turbulence intensity would have an increased sound propagation in up- and downstream direction [24]. This is also the reason for the increased contribution of the propeller in the SRVs ON case in up- and downstream direction.

A deeper understanding can be created when examining the acoustic pressure traces in the frequency domain. In Figure 5.18b to 5.18f, the sound pressures are plotted in the frequency domain for five locations ($\theta = 0°$, 45°, 90°, 135° and 180°) around the ring used in Figure 5.18a. The PBL in $1/12^{th}$ octave bands is used and the frequency f is normalised by the blade passing frequency (BPF). The PBL is equal to the sound pressure level (SPL) within the specified band. At $\theta = 90°$ (Figure 5.18b), the propeller emits most noise at the first harmonic (f = BPF) for both cases. The amplitude of the first harmonic reduces in magnitude when moving away from the point of maximum noise. As can be deducted from the shape of the OSPL polar, the first harmonic is smaller at $\theta = 135°$ (Figure 5.18c) than at $\theta = 45°$ (Figure 5.18d). Up- and downstream of the propeller, the peak corresponding to the first harmonic has completely disappeared. This agrees with observations made by Deming [16] and can be explained by destructive interference between the sound pressure contributions generated by the different propeller blades. This is again a consequence of the uniform inflow experienced by the propeller and an increase of noise levels in the axial direction can be expected when the inflow is non-axial or with a larger turbulence intensity.

The PBL plots confirm that the propeller is affected by the presence of the SRVs, as can be concluded from the added noise at the higher harmonics (multiples of the BPF) with respect to the isolated propeller. As example, the propeller contribution for the sixth harmonic at $\theta = 45°$ (Figure 5.18d) is increased by 20 dB by adding the SRVs, such that it becomes a considerable harmonic. Note that the first harmonic at $\theta = 135°$ (Figure 5.18c) is decreased by the addition of the SRVs, possibly due to destructive interference. The unsteady loading of the SRVs causes a varying potential field which propagates upstream and effects the blades of the propeller [32]. Although the upstream aerodynamic effect is seen to be small in Section 5.1.1, the propeller loading is altered such that it produces substantial higher-harmonics noise. Again, this opposes the results from research by Dittmar & Hall [18].

In agreement with Sinnige et al. [49], the vanes are seen to be the cause of considerable noise at the higher harmonics. As shown in the polar plot of the OSPL, this noise is more uniformly distributed along all directions, which results in PBL peaks of roughly the same magnitude for the five locations displayed in Figure 5.18b to 5.18f. Due to the dominance of the first harmonic at $\theta = 90°$, the contribution of the vanes to the OSPL is minimal at this location. As the first harmonic caused by the propeller reduces when moving up- or downstream, the higher harmonics caused by the SRVs become dominant. It can be seen that the propeller produces noise at the same frequencies as the SRVs for the SRVs ON case, which is a consequence of the interaction effect. At $\theta = 0°$ and 180°, the SRVs produce noise at even multiples of the BPF, which can be explained by the presence of six propeller blades and four SRVs, as is done in Section 5.1.1.

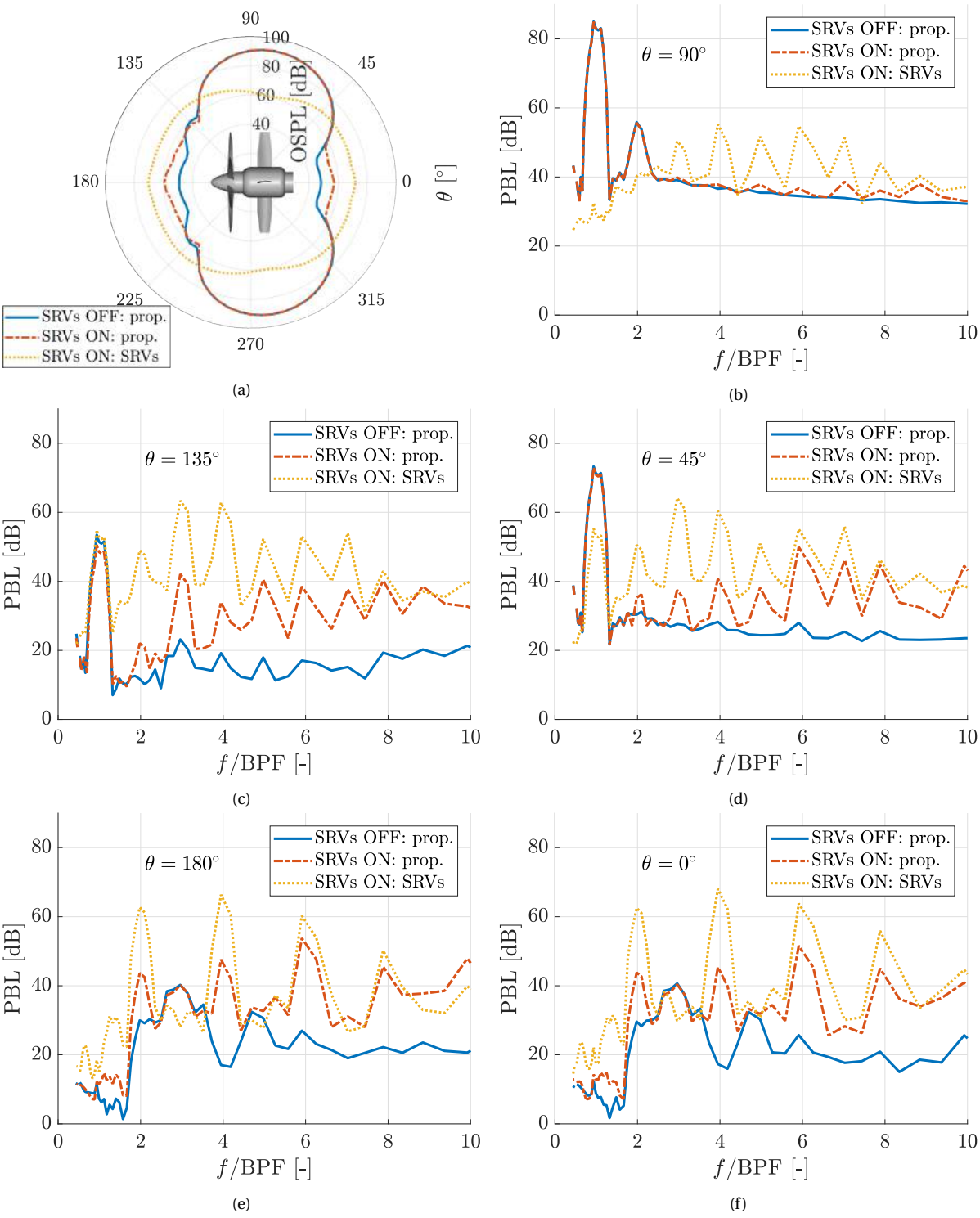

Figure 5.18: Polar plot of the overall sound pressure level (OSPL) in (a) and the pressure band level (PBL) in $1/12^{th}$ octave bands at various angles θ in (b) to (f). The contributions of the propeller and SRVs at a distance of $10D$ from the midpoint between propeller and SRVs are shown.

5.2.2. Acoustic power

A single frequency domain representation is attainable by integrating the acoustic pressure in the far-field over all angles θ to compute the power watt level (PWL) while assuming axisymmetry. The PWL is a logarithmic scale of the acoustic power emitted by a source and is presented in the frequency domain in Figure 5.19 where the contributions of all surfaces are combined. The same conclusion as in Section 5.2.1 can be drawn

that the SRVs are the cause of additional acoustic power at higher harmonics of the BPF.

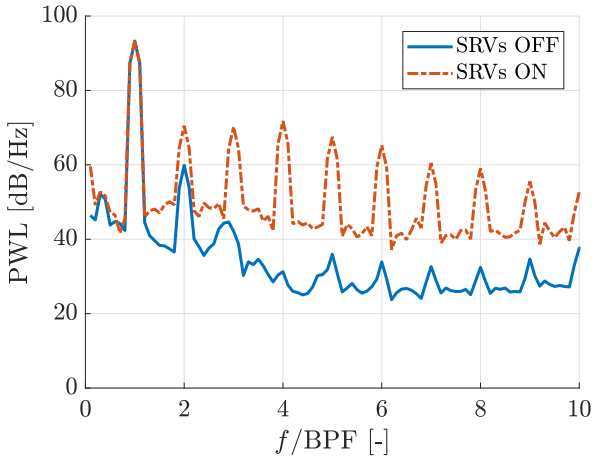

Figure 5.19: Power watt level (PWL) for the SRVs OFF and ON case where the contributions of all surfaces are combined.

5.2.3. Full-scale frequency range

As the simulations are performed on a 1:9 scaled-model, an estimation of the dominant frequency range for the full-scale model can be performed. It can be seen in Figure 5.18 and 5.19 that the dominant noise for the scaled model is emitted in a frequency range from the first to the eighth harmonic of the BPF, i.e. in a range of 0.7-5.7 kHz. The scaling can be done by keeping the advance ratio $J = \frac{V_\infty}{nD}$ constant, or equivalently, keeping the Strouhal number $St = \frac{fL}{U}$ fixed. The Strouhal number denotes the ratio of the speed of dynamic processes (frequency f times characteristic length L) to the speed of the steady processes (flow velocity U). Using the same advance ratio of 0.6, corresponding to take-off conditions, and assuming an equal free-stream velocity of 29 m/s, which occurs at some point during the take-off procedure, the ratio of nD has to stay constant. As the diameter of the full-scale propeller is 9 times the diameter of the scaled-model, the rotational velocity and hence the BPF is divided by a factor of 9. The resulting dominant frequency range for the full-scale propeller therefore becomes 80-630 Hz. As this range is well below 1000 Hz, it has a relatively low noisiness (Section 2.7.1). The perceived increase in noise caused by the SRVs is thus smaller for the full-scale propeller compared to the 1:9 scaled model.

5.2.4. Contribution of the vane tips

It is expected by Sinnige et al. [49] that the impingement of the RTVs on the SRVs is an additional source of noise. To investigate this assumption, the vanes are split up into four surfaces: LE, TE, tip and middle, see Figure 5.20a. The same definition of the LE, TE and tip are used to define VR12 in Section 3.1.3. The contribution of each of these four surfaces to the OSPL is presented in Figure 5.20b. The leading edge (LE) is the main source of noise with an OSPL of 1.7 to 7.6 dB higher than the contribution of the tip. Further research is required to confirm what the effect is of reducing the length of the vanes on the emitted noise.

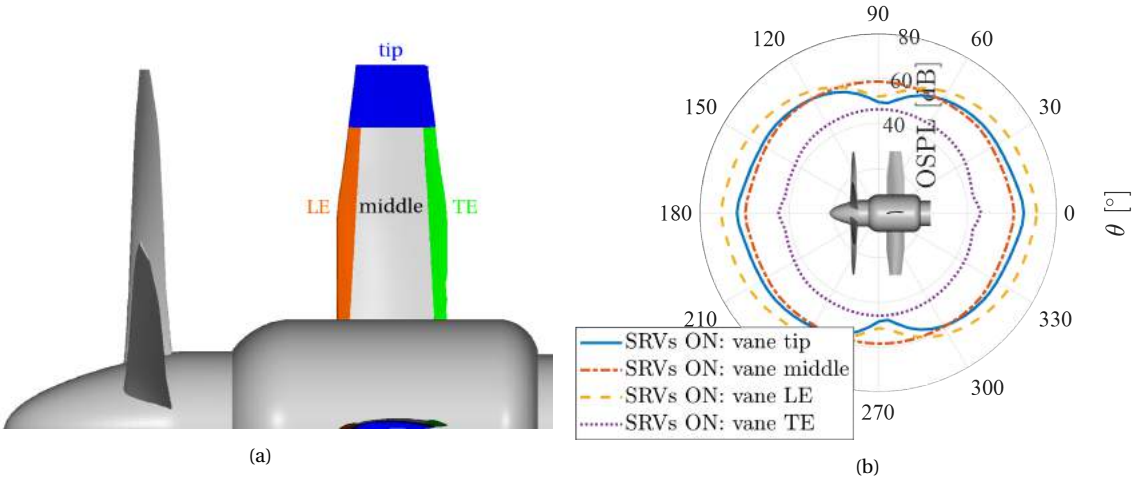

(a) (b)

Figure 5.20: The division of the vanes in various surfaces is visualised in (a). Polar plot of the overall sound pressure level (OSPL) for the contributions of these surfaces at a distance of $10D$ from the midpoint between propeller and SRVs in (b).

5.3. Shortened vanes

A second geometry has been simulated in which the length of the vanes has been reduced. This is motivated by the observation that the vane tips have a relatively low thrust production in combination with the notion in literature [49] that the RTV impingement is a source of noise. The vanes have been cut such that their outer radius equals $0.84R$. The remainder of the geometry and the flight conditions are unaltered. The grid has the same resolution and a similar definition of the VR regions is used, apart from the VR12 region around the vane tips which has been excluded. Adding another VR12 region around the tip of the shortened vanes could be beneficial in resolving the high pressure gradients at the tip accurately, which can be seen in Figure 5.24b. The simulation has been seeded with the results for the original vanes.

The change in geometry has a negligible effect on the upstream propeller with the propeller thrust coefficient being reduced by 0.01% compared to the case with the long vanes. The thrust produced by the upward vane is compared in Figure 5.21 with the original case, from which two conclusions can be drawn. Firstly, the small peaks in thrust produced by the vane have disappeared. As demonstrated in Section 5.1.2, these peaks are caused by the impingement of the rotor tip vortices (RTVs) which confirms that the vanes have been shortened sufficiently to avoid this phenomenon. Secondly, the time-averaged thrust is reduced by 13% by shortening the vanes and is now equal to 2.0% of the propeller thrust. The reduction in thrust is larger than the thrust produced by the tip region ($r/R > 0.84$) for the original vanes, which equals 1.9% of the vane's thrust. The shortened vane thrust is thus smaller than the thrust produced by the area of $r/R < 0.84$ for the original vanes. It can therefore be concluded that the thrust distribution over the vane is altered by shortening it.

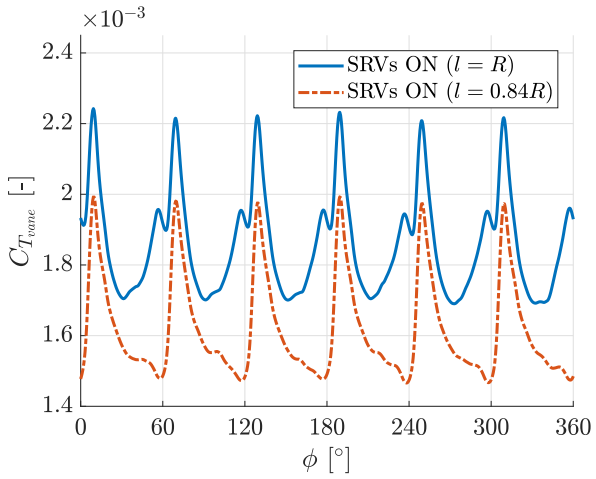

Figure 5.21: Thrust coefficient of the upward vane for the original vanes ($l = R$) and the shortened vanes ($l = 0.84R$).

To visualise the altered thrust distribution over the upward vane, a comparison is made in Figure 5.22 for two time instants. The thrust distributions are similar around the root region of the vane and increasingly deviate towards the tip of the shortened vanes. The stator tip vortex (STV) can be concluded to be stronger for the case with the short vanes, which is confirmed by Figure 5.23 in which the averaged vorticity magnitude downstream of the SRVs is plotted. The close proximity of the tip vortex to the high loading area reinforces the negative effect of the tip vortex on the thrust distribution.

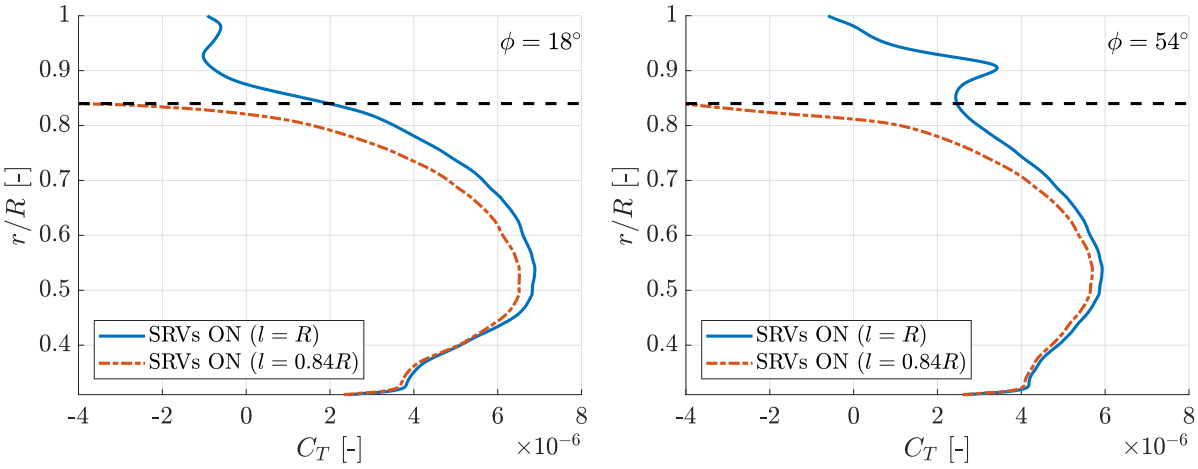

(a) (b)

Figure 5.22: Phase-averaged thrust distribution for the original SRVs ($l = R$) and the shortened vanes ($l = 0.84R$) over the upward SRV for two phase angles expressed as C_T per segment. 474 segments are used for the original vanes and 361 for the shortened vanes. The black dashed line indicates $r/R = 0.84$.

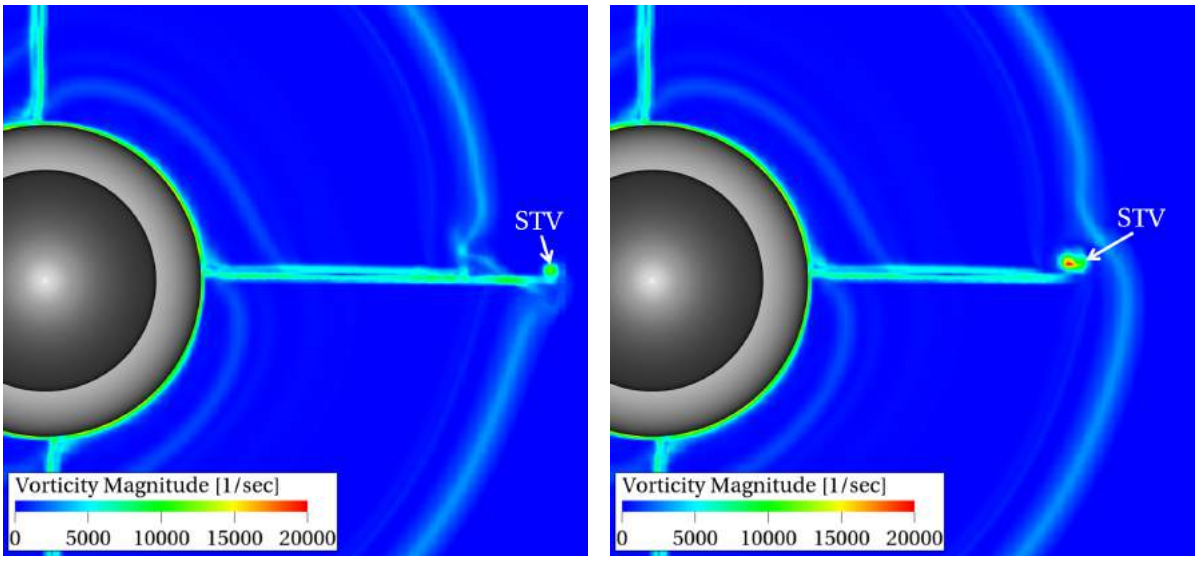

(a) (b)

Figure 5.23: Time-averaged vorticity magnitude in a plane $0.4c_r$ downstream of the SRVs (i.e. $x/D = 0.45$) for the original (a) and shortened vanes (b).

The STV causes an area of negative thrust at the tip in both cases, which is larger in magnitude for the shortened SRVs. The core of the STV is positioned on the suction side of the vane, as can be concluded from the pressure contours in Figure 5.24. The low pressure on the suction side in combination with the tangential velocity at the tip of the shortened vanes are expected to cause the STV to move to this location. The resulting low-pressure region at the aft end of the vane causes a negative thrust, visible in Figure 5.24. This can be explained by the reasoning presented in Section 5.1.7.

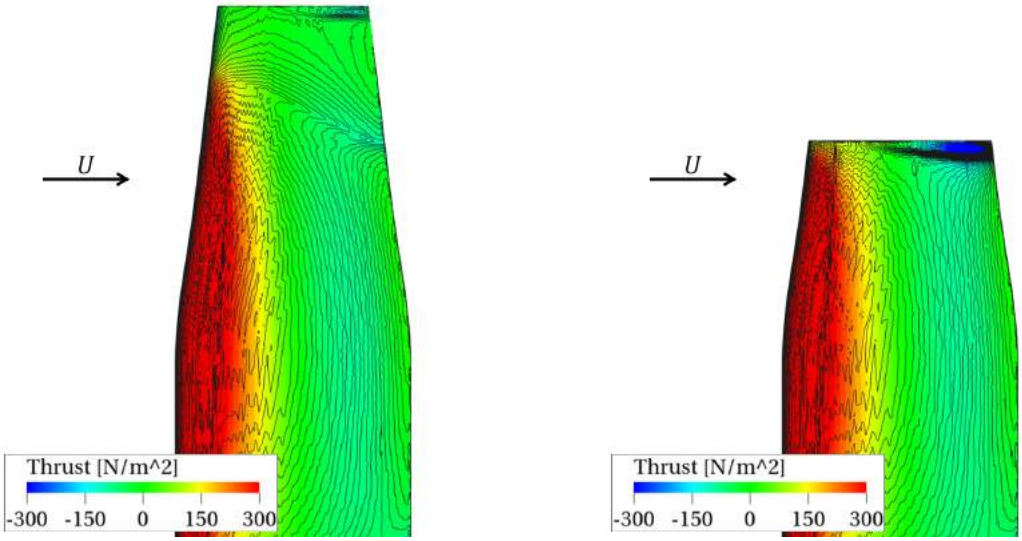

(a) (b)

Figure 5.24: Time-averaged surface thrust force on the suction side of an original (a) and shortened vane (b). Pressure contours are included in black and the direction of inflow velocity U is included (radial component of the velocity is neglected).

The reduced thrust-generating capability of the shortened vanes is also reflected in a lower swirl reduction, as is visible in Figure 5.25. When comparing the average swirl angle from $x/D = 0.43$ to $x/D = 1$ for the three cases, it can be concluded that the short SRVs recover 13% less of the swirl than the long vanes do. Interestingly, this number is equal to the reduction in average vane thrust.

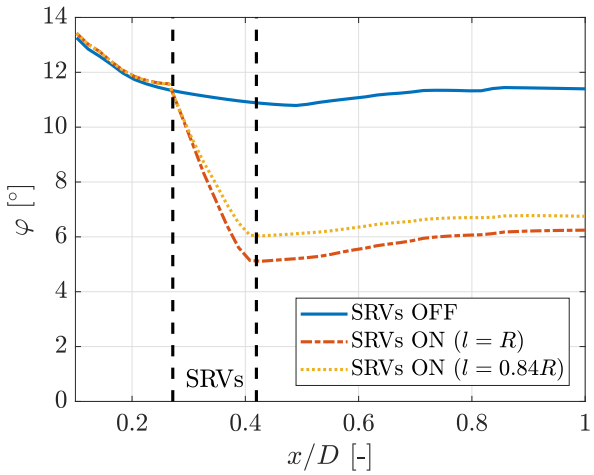

Figure 5.25: Development of the average swirl angle for the SRVs OFF, original SRVs ON and shortened SRVs ON case. The SRV's LE and TE location are indicated by the dashed lines.

To compare the swirl distributions, the swirl angle is circumferentially averaged into 30 intervals ($0.3 < r/R < 1$) in a plane upstream and downstream of the SRVs in Figure 5.26. All three configurations are included, for which similar swirl distributions are obtained upstream of the SRVs, see Figure 5.26a. A peak in swirl angle is present around $r/R = 0.9$ in Figure 5.26a which indicates the presence of the RTVs. Both sets of SRVs cause a slight upstream swirl increase at the root region, which can be explained by the upwash present in front of the SRVs.

The swirl angle is uniformly decreased by 0.7° for the SRVs OFF case when progressing from $x/D = 0.24$ to $x/D = 0.45$. A second peak is present around $r/R = 0.8$ at $x/D = 0.45$ (Figure 5.26b) which is caused by the blade wake deformation as explained in Section 4.2.

It can be seen in Figure 5.26b that the original and short vanes cause a similar reduction in swirl angle for the region of $r/R < 0.8$, despite the altered thrust loading distribution over the vanes. The swirl direction

at the root is reversed. The original vanes reduce the swirl in the outboard region with an opposite swirl direction at the tip as a consequence. The shortened vanes have a minor swirl recovery for $r/R > 0.8$ and no noticeable peak due to the RTVs. This is a consequence of vortex shearing in spanwise direction which will be explained next.

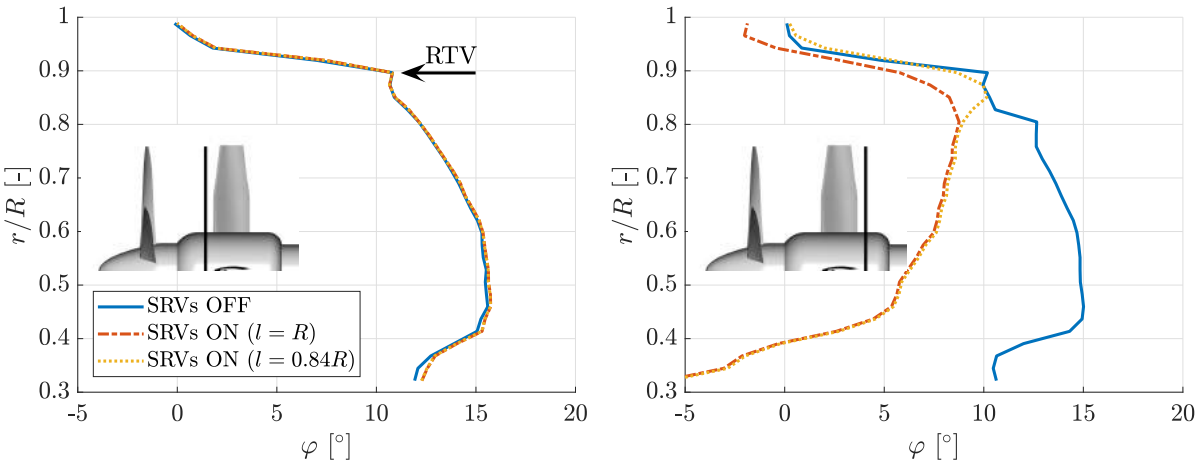

Figure 5.26: Time- and spatially-averaged (into 30 intervals) swirl angle φ downstream of the propeller at $x/D = 0.24$ (a) and $x/D = 0.45$ (b) for the SRVs OFF, original SRVs ON and shortened SRVs ON case.

The λ_2 isosurfaces in Figure 5.27 confirm that the impingement of the RTVs on the SRVs is avoided by shortening the vanes. However, there is still a spanwise motion present of the RTV on the pressure and suction side of the vane. The motion occurs in the same direction as for the original vanes, but is explained differently. The stator tip vortex (STV), indicated in Figure 5.27b, has been demonstrated to be of greater strength than for the original vanes. It consists of a rotational motion around the negative x-direction such that a velocity in the positive y-direction is induced on the pressure side and a velocity in the negative y-direction on the suction side. This is the cause of the spanwise motion of the RTVs as is confirmed by the observation that this motion is only initiated when the RTV is in close proximity to the STV.

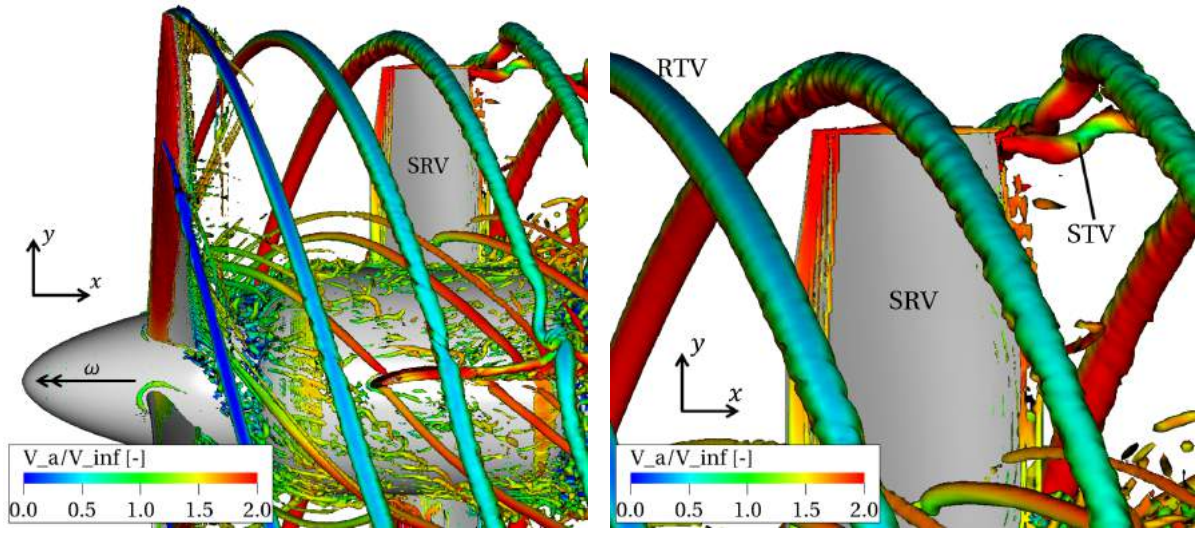

Figure 5.27: Phase-averaged isosurface of $\lambda_2 = -3 \cdot 10^6$ s^{-2} coloured by the normalised axial velocity for the shortened SRVs case. The propeller rotation direction is indicated by ω in (a). (b) shows a close-up of the pressure side of the upward vane.

The aeroacoustic performance of the shortened vanes is inspected by comparing the overall sound pres-

sure level (OSPL) around the same ring as used in Section 5.2.1. The OSPL is plotted in Figure 5.28 for the three configurations taking into account the contribution of various surfaces, which are indicated in red. In Figure 5.28a, the contribution of all solid surfaces is combined and in Figure 5.28b and 5.28c the contribution of the propeller and SRVs are displayed separately. The difference in OSPL between the original and shortened vanes can be concluded to be small, compared to the difference with the isolated propeller. The ΔOSPL, defined as $\Delta\text{OSPL} = \text{OSPL}_{\text{SRVs ON } (l=0.84R)} - \text{OSPL}_{\text{SRVs ON } (l=R)}$, is therefore displayed in Figure 5.28d. The frequency domain representation for four locations along the ring are given in Figure 5.29 and 5.30, where the location and the contributing surfaces are indicated. The results for $\theta = 180°$ are similar to $\theta = 0°$ and therefore omitted.

The difference in noise emitted by the propeller is small with a decrease at $\theta = 0°$ and $\theta = 180°$ and an increase at $\theta = 135°$, see Figure 5.28d. The decrease at $\theta = 0°$ is caused by a reduction in sound pressure in between the second, fourth and sixth harmonic of the BPF for the shortened vanes (Figure 5.29c). This reduced broadband noise could indicate a reduction in turbulence along the blades. At $\theta = 135°$, it can be concluded from Figure 5.30d that the propeller emits more noise at the fourth and sixth harmonic when the length of the SRVs is reduced. The propeller is not the dominant noise source for both $\theta = 0°$ and $\theta = 135°$ such that the effect on the total OSPL is minimal.

The shortened vanes are seen to emit less noise in sideways direction due a reduced third and fourth harmonic at $\theta = 90°$, see Figure 5.30e. However, as the contribution of the vanes is small in this direction, the total OSPL is unaltered. The SRVs emit more noise in up- and downstream direction, where the contribution of the vanes is dominant. A clear increase in the second harmonic is evident from Figure 5.29e for $\theta = 0°$. This opposes the expectation that the tonal noise would decrease by avoiding the impingement of the RTVs on the vanes, which occurs at a frequency equal to double the BPF. The shortening of the vanes therefore causes the total OSPL to increase up- and downstream of the propeller by up to 1.8 dB.

Interestingly, the first harmonic for the overall PBL at $\theta = 135°$ (Figure 5.30b) is reduced substantially, even though the propeller and SRVs contributions do not show this behaviour. Destructive interference occurs between the sound originating at the propeller and at the shortened SRVs at this specific location and frequency, enabled by the fact that both sources cause a first harmonic of similar amplitude. The total OSPL is as a consequence decreased by 1.8 dB at $\theta = 130°$ and 1.4 dB at $\theta = 135°$, see Figure 5.28d.

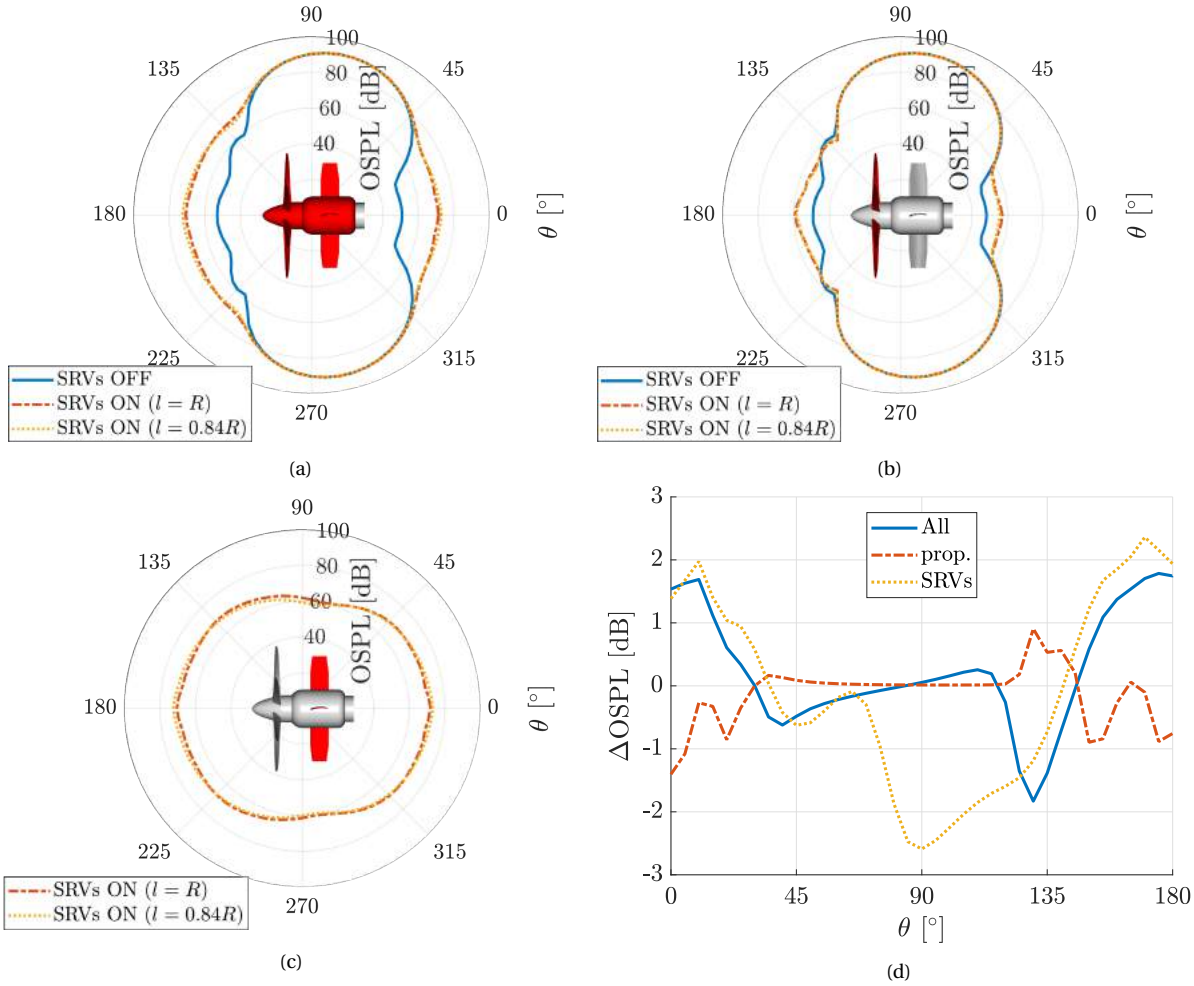

Figure 5.28: Polar plot of the overall sound pressure level (OSPL) at a distance of $10D$ from the midpoint between propeller and SRVs for the contributions of all solids (a), the propeller (b) and the SRVs (c). All three configurations are included. $\Delta\text{OSPL} = \text{OSPL}_{\text{SRVs ON } (l=0.84R)} - \text{OSPL}_{\text{SRVs ON } (l=R)}$ is presented in (b) for the same contributions of surfaces

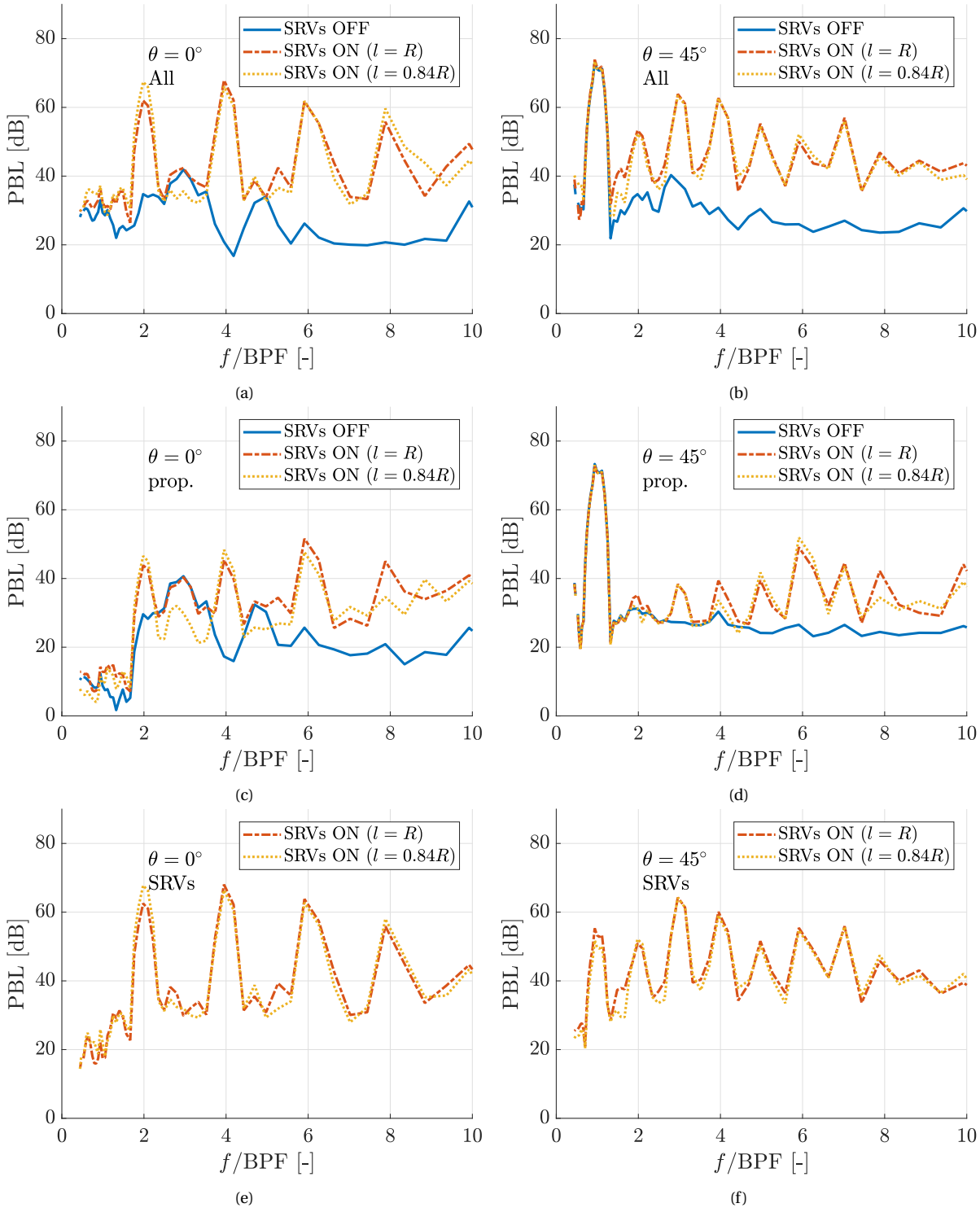

Figure 5.29: Pressure band level (PBL) in $1/12^{th}$ octave bands at $\theta = 0°$ and $\theta = 45°$ for various contributions of surfaces at a distance of $10D$ from the midpoint between propeller and SRVs.

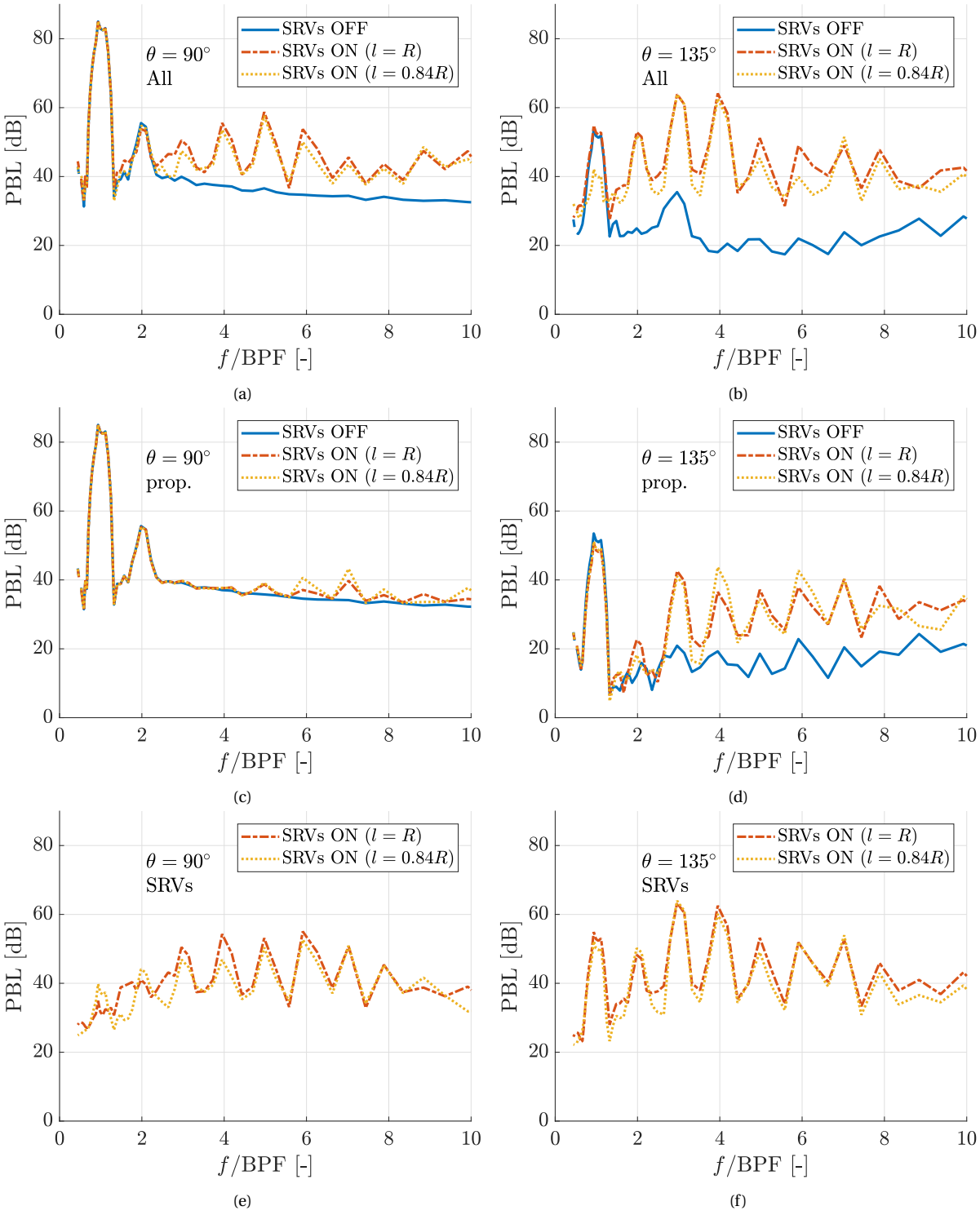

Figure 5.30: Pressure band level (PBL) in $1/12^{th}$ octave bands at $\theta = 90°$ and $\theta = 135°$ for various contributions of surfaces at a distance of $10D$ from the midpoint between propeller and SRVs.

6

Conclusion

In order to conclude this manuscript, the research questions as posed in the introduction are answered. The six sub-questions will be discussed first, followed by the main research question.

1. Is LBM a suitable method to be used in this project?
Yes. LBM is capable of delivering the desired results to answer the subsequent research questions. Apart from aeroacoustics, it is capable of resolving the unsteady aerodynamic effects. The aerodynamic validity of the presented results is demonstrated by comparison with results obtained from RANS simulations and experiments. The aeroacoustic validity has been derived from literature [4, 9, 42].

2. Do SRVs offer aerodynamic performance benefits?
Yes. The SRVs cause an increase of the time-averaged total propulsive efficiency of 2.4% for a high propeller loading at a flight condition corresponding to take-off ($J = 0.6$). This value lies within the range of values obtained in previous studies [22, 50, 54]. As the propeller loading and slipstream swirl are reduced for cruise, the efficiency increase is expected to reduce for that flight condition.

A periodically varying swirl angle is observed in the propeller slipstream caused by high swirl regions in the wakes of the propeller blades and within the RTVs. These fluctuations have an important effect on the performance of the SRVs and cause the thrust produced by the vanes to oscillate by 33% with a period of $\phi = 30^\circ$.

3. What improvements to the current configurations in terms of aerodynamic performance can be suggested?
As half of the swirl is recovered by the four vanes, half of the swirl is still present behind the vanes. Installing more vanes could therefore increase the aerodynamic performance further, which is consistent with the conclusion of Li et al. [33]. Reducing the length of the vanes is demonstrated to have a substantial negative effect on the aerodynamic performance. Vanes of length $l = 0.84R$ generate 13% less thrust and recover 13% less swirl than the original vanes of length $l = R$. This is in part due to the absence of the impingement of the high swirl regions in the RTVs but the major thrust decrease is caused by the altered thrust distribution over the vane. However, redesigning the shorter vanes could result in a higher thrust production due to an improved loading distribution. Finally, an interesting analysis would be to design SRVs for various flight conditions and to decide on an optimal configuration for the complete flight mission, possibly using a variable pitch system.

4. What are the noise effects of SRVs?
The SRVs cause noise at harmonics of the BPF, relatively uniformly emitted in all directions. As the first harmonic caused by the propeller is dominant in the region of maximum noise, the maximum OSPL is not increased. The SRVs become a dominant noise source up- and downstream of the propeller, where the OSPL is increased by more than 20 dB. Note that the contribution of the propeller at these locations would increase for real-life conditions.

Although the upstream aerodynamic effect of the SRVs on the propeller is seen to be small, the aeroacoustic behaviour of the propeller is influenced by the installation of the SRVs. The propeller in the SRVs ON case

produces noise at higher harmonics of the BPF, similar to the the SRVs.

5. Which noise sources can be identified?
The leading edge of the vanes is seen to be the main source of noise on the vanes. This is attributed to the fluctuating loading of the SRVs and can therefore be classified as loading noise. The tips of the vanes are of special interest at it is expected in literature that the impingement of the RTVs is a substantial cause of noise [49]. A configuration with shortened vanes has therefore been simulated which proved that no noise reduction is present. On the contrary, the shortening of the vanes caused a noise increase of 1.8 dB up- and downstream of the propeller due to an increase in sound pressure at the second harmonic of the BPF.

6. What improvements to the current configurations in terms of noise can be suggested?
The regions of high swirl in the propeller slipstream impinge on two vanes simultaneously due to the presence of six propeller blades and four vanes. A noise reduction is expected [32, 54] when this phenomenon is avoided by for example increasing the number of vanes to five. SRVs with a swept leading edge could also diffuse the impingement of the high swirl regions to reduce the noise, as has been done by Dittmar & Hall [18]. In general, the aeroacoustic performance could increase substantially when aeroacoustics are included in the design process.

Moreover, it would be interesting to simulate a full-scale configuration in order to have a better assessment of the frequency range of the added noise due to the SRVs. Finally, simulating a case with an inflow that approximates real-life conditions better would result in a more accurate prediction of the relative magnitude of the noise contributions of the SRVs and propeller in up- and downstream direction.

• ***Are SRVs a feasible option to enhance performance of propeller propulsion systems?***
Yes. The increase in aerodynamic performance due to the addition of SRVs is clear and substantial. This makes them economically feasible as the cost is low due to their simplicity. The added noise is acceptable as the largest increase occurs in the directions of least importance: up- and downstream of the propeller. The total sound pressure is unaltered in the direction of maximum noise such that the cabin and ground noise are largely unaltered.

A

SRV in a Tractor Propeller Configuration

A.1. Computational setup

Tractor propeller configurations are common on regional transport aircraft. A fourth configuration, consisting of a propeller, wing and SRV (Figure A.1), has been simulated for which the preliminary results are presented in this chapter. As the wing has a substantial impact on the slipstream flow, it is incorporated in the design process. The design and this simulation are performed at a flight condition relating to cruise with $V_\infty = 140$ m/s and $J = 2.4$ at an altitude of 5000 m. The propeller is rotating inboard up and is similar to the propeller used in the main part of this report with a diameter $D = 0.4064$ m. The blade pitch angle β is altered and equals 50° at 70% of the radius. The wing has zero twist and dihedral angle and a straight quarter-chord line. The halfspan of the wing has a length of $4.1D$ and a NACA 64_2-415 airfoil is adopted. The root chord equals $0.95D$ and the tip chord $0.37D$. The origin is defined as annotated in Figure A.1 at the root of the wing at quarter chord such that the propeller axis is located at $z = D$. The SRV has the same length as a propeller blade and is located at an angle of 22° from the $y = 0$-plane.

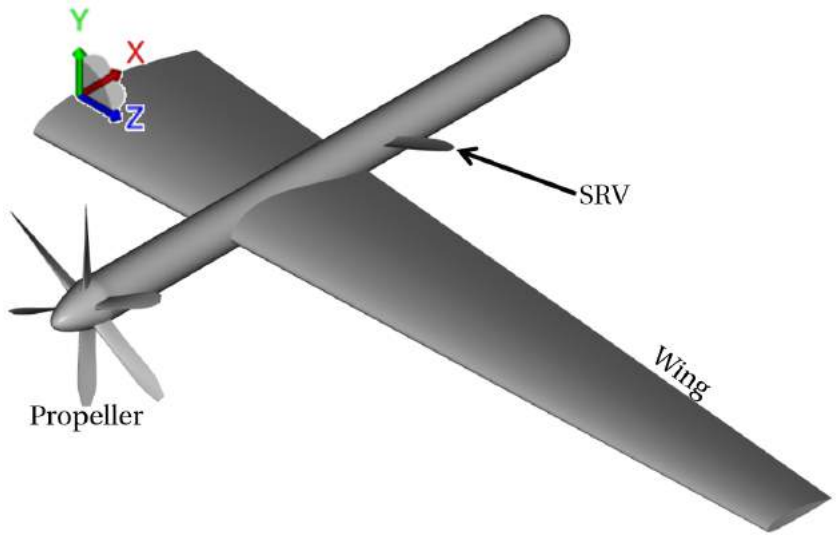

Figure A.1: Geometry of tractor propeller configuration with SRV. The adopted coordinate system is indicated.

The computational setup is similar to the setup used for the cases presented in the main body of this report. The simulation volume is defined as a rectangle with a length of $20.5D$, a width of $12.5D$ and a height of $15D$. A symmetry plane is present at the wing root at $z = 0$ and a velocity inlet is defined with a V_∞ of 140 m/s and a temperature of 266.65 K. The outlet is defined by a static pressure of 54,050 Pa and a free flow direction. No-slip boundary conditions are applied to all surfaces. A volume of revolution is generated containing the propeller and spinner with a clearance from the surfaces of 19 mm. A rotating reference frame is defined for this volume with an angular velocity $\Omega = 144$ rev/s, corresponding to the operating condition of

$J = 2.4$. Simulations are seeded with the end result of the preceding simulation with a coarser grid. Although the propeller thrust is fluctuating due to the upstream effect of the trailing wing [51], it is concluded from Figure A.2 that time convergence is reached after two propeller rotations (N_{rot}). The root mean square error (RMSE) is included which is calculated using the values from the start of the simulation to the particular time step. Results are subsequently stored for three propeller rotations. An acoustic sponge is implemented by varying the kinematic viscosity per unit temperature from 0.005 m^2/sK close to the geometry to 0.5 m^2/sK in the farfield. An exponential transition region is present between a distance of $4.6D$ and $6.2D$ from the crossing between propeller axis and the wing quarter chord line, see Figure A.3a.

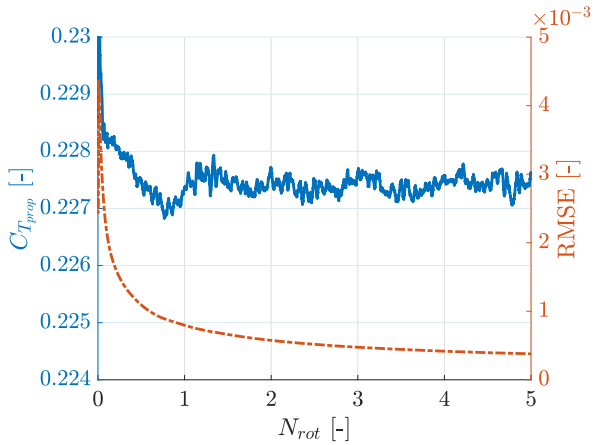

Figure A.2: Instantaneous propeller thrust coefficient on the left vertical axis and the root mean square error (RMSE) on the right. Time is expressed as number of propeller rotations N_{rot} from the start of the simulation on the horizontal axis.

12 variable resolution (VR) regions are defined which are numbered increasing with resolution, as visualised in Figure A.3 and A.4. The resolution increases with a factor of two from one VR region to the next. VR1 is the simulation volume, displayed in olive in Figure A.3a. VR9 consists, among others, of a cylinder (black in Figure A.3b) of diameter $1.15D$, ranging from $x = -D$ to $x = D$. The black cylinders in VR2 to VR8 are defined by an offset from this cylinder, sized such that there are 10 voxels present in between two cylinder boundaries. A blue cylinder is defined for VR9 around the wing tip with a diameter of $D/4$, ranging from $x = -D/8$ to $x = D/2$, see Figure A.3b. A VR8 cylinder is defined by an offset of 10 voxels from this cylinder. A polyhedron is defined for VR9 behind the wing with length of half the local chord and thickness equal to the wing thickness.

VR10 consists of a cylinder region (red in Figure A.4) aimed at capturing the propeller slipstream. This cylinder has a diameter of D and ranges from $x = -D$ to $x = D$. Two VR regions are defined around the wing surface, see Figure A.4. One for VR10 (in purple) with an offset of 0.18 times the propeller root chord c_r around the complete wing and one for VR11 (in green) with an offset of $0.061c_r$ around the part of the wing emerged in the propeller slipstream (assuming the slipstream to have a diameter D). Furthermore, two regions are defined around the other surfaces with offsets of $0.061c_r$ (VR11) and $0.18c_r$ (VR10). Finally, the finest region (VR12, green) is defined by an offset of $0.030c_r$ from regions around the leading and trailing edge of both the propeller and vane, defined to be approximately 10% of the local chord. A region of similar size has been added around the propeller tip and a region of 10% of the SRV length has been applied to the SRV tip.

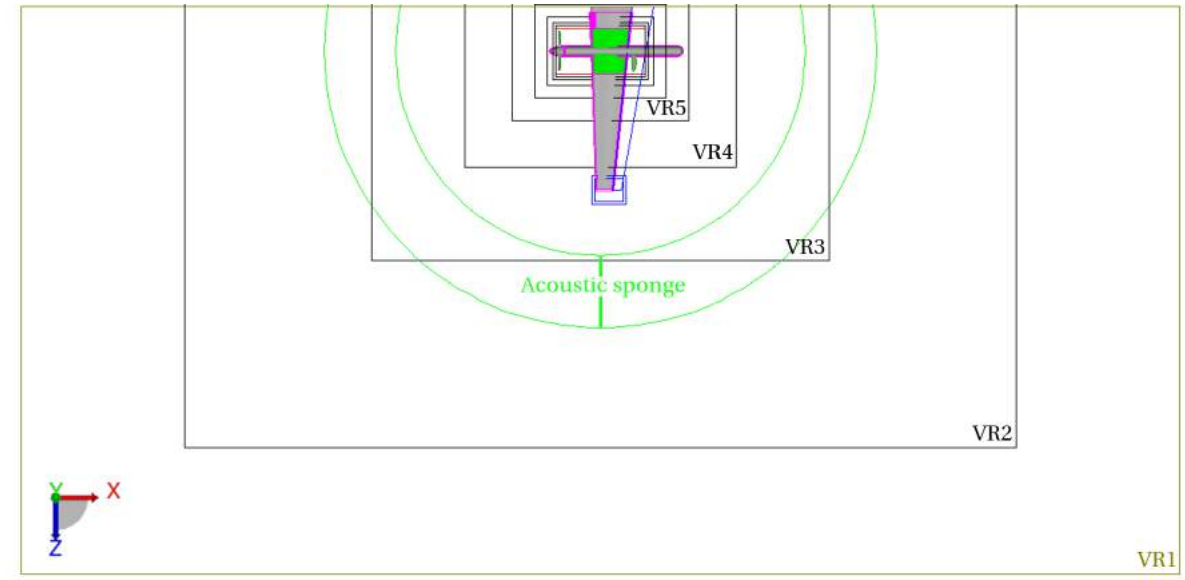

(a)

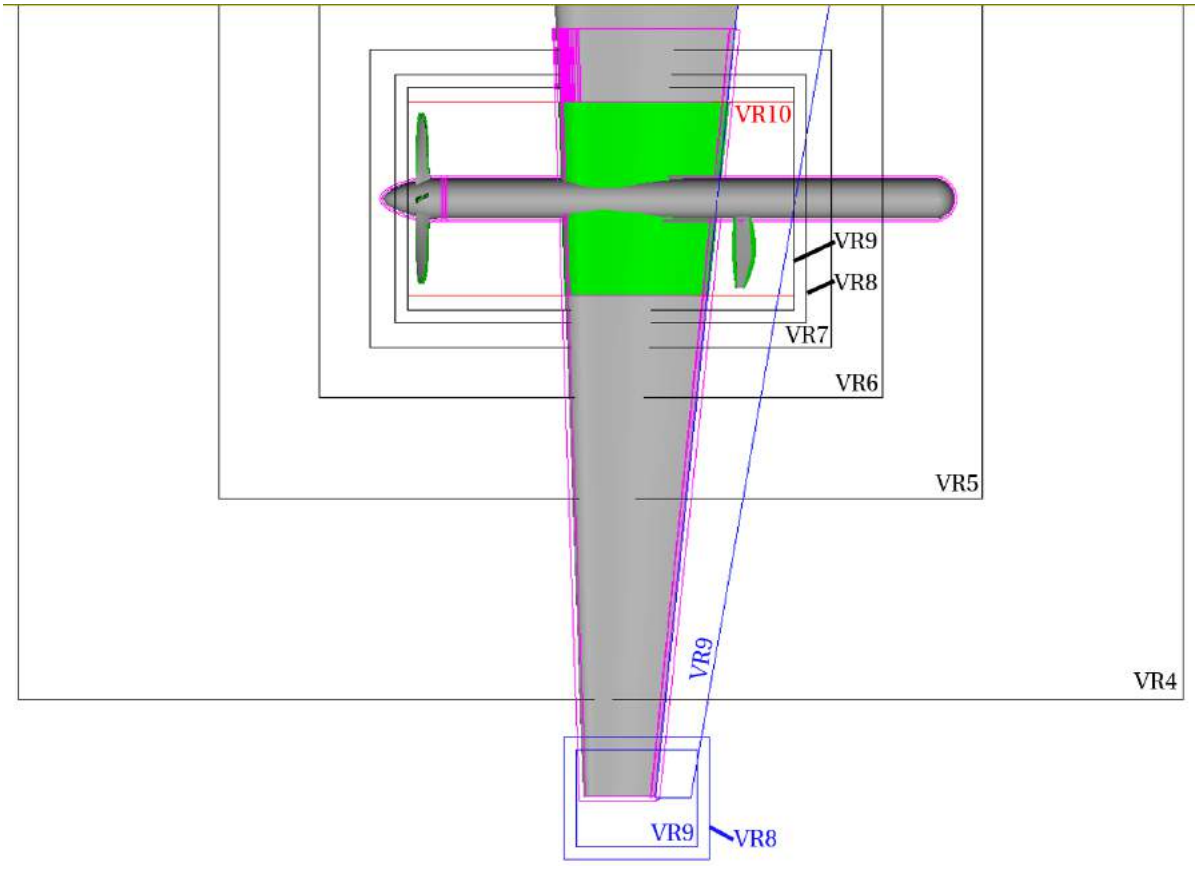

(b)

Figure A.3: Visualisation of the VR regions in the far-field (a) and around the wing (b). The adopted axis system and the acoustic sponge are indicated in (a).

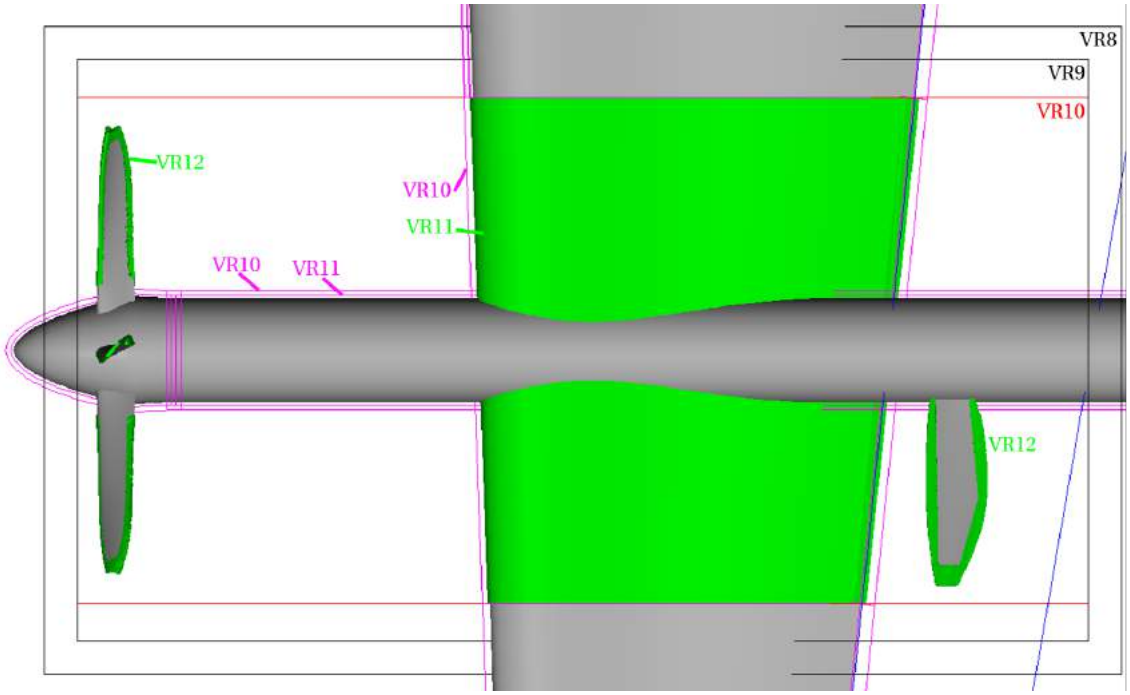

Figure A.4: Visualisation of the VR regions around the propeller slipstream.

A.2. Grid independence study & Validation

The time-averaged propeller and SRV thrust coefficients obtained with a coarse (50 voxels/c_r for VR12), medium (100 voxels/c_r for VR12) and fine (200 voxels/c_r for VR12) grid are displayed in Figure A.5 and A.6, respectively. A RANS simulation has been performed prior to this study for which the results are included. The propeller thrust is converging towards the value obtained with RANS, although no perfect agreement is obtained. RANS predicts a propeller thrust coefficient of 0.238 where LBM with the 200 voxels/c_r grid results in a $C_{T_{prop}}$ of 0.228 (4.5% lower).

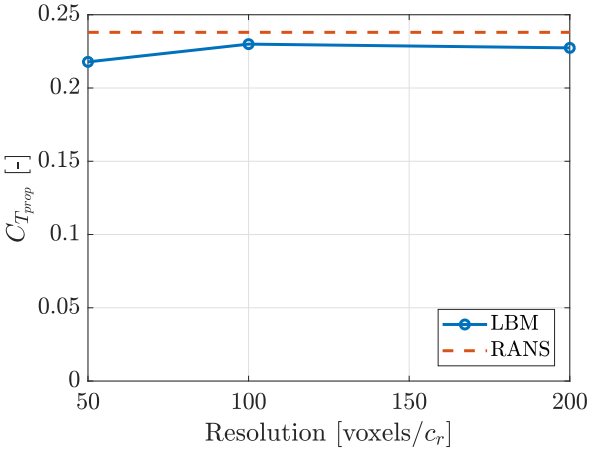

Figure A.5: Averaged propeller thrust coefficient obtained using grids with increasing resolution. Value obtained with RANS is included.

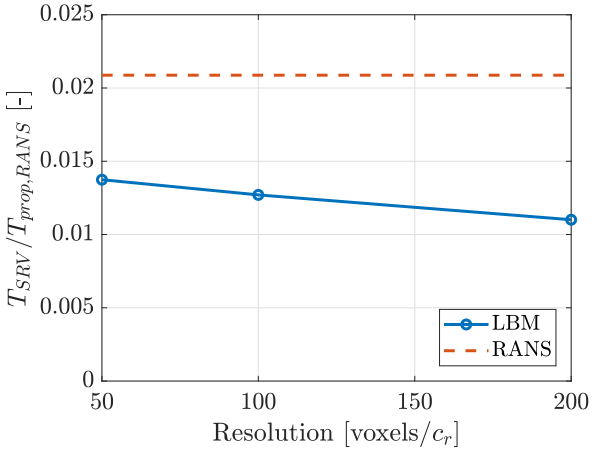

Figure A.6: Averaged SRV thrust with respect to the propeller thrust obtained with RANS. SRV thrust obtained with RANS is included.

The SRV thrust T_{SRV} is diverging away from the RANS value, as is visible in Figure A.6 where the SRV thrust is normalised by the propeller thrust as obtained from RANS $T_{prop,RANS}$. The T_{SRV} obtained with the grid with 200 voxels/c_r is 0.17 N or 13% lower than the value obtained with the grid of 100 voxels/c_r. As for the configuration without a wing, the cause is looked for in an incomplete grid convergence of the propeller slipstream, causing an unconverged SRV inflow. To test this hypothesis, the time-averaged swirl angle up-

stream of the SRV, relating directly to the SRV inflow, is displayed in Figure A.7. As the SRV is located behind the downgoing propeller blade, only half of the slipstream behind the downgoing blade is incorporated when averaging the swirl angle into thirty intervals between $0.21 < r/R < 1$. The slipstream is indeed seen to be unconverged with grid resolution with a maximum difference in averaged swirl angle between 100 and 200 voxels/c_r of $\varphi = 0.22°$ or 7.5%. Further simulations with higher resolution grids are required to obtain grid independent results. It is therefore decided to display the results for all three grids together where possible in this Chapter. Otherwise, the results for the fine grid (200 voxels/c_r) are used.

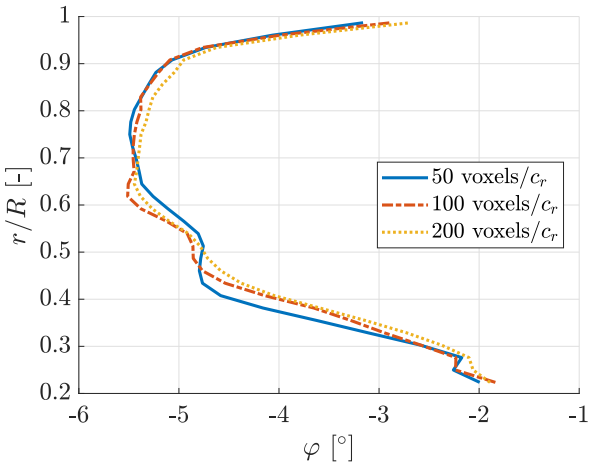

Figure A.7: Time- and spatially-averaged swirl angle φ $0.4c_r$ behind the wing trailing edge (i.e. $x/D = 0.64$) for various resolution cases. See Figure A.16a for visualisation of the plane's location.

When comparing the axial and tangential velocity distributions over the full slipstream at $x/D = 0.64$ to results obtained with RANS, Figure A.8 is obtained. Good agreement is observed between LBM and RANS with the largest deviations at the root ($r/R < 0.4$) and tip ($r/R > 0.7$) region. These regions include the most turbulence caused by viscous effects over the fairing and the rotor tip vortices. A high resolution is required in LBM to resolve these smaller-scale structures accurately, as was noticed in Section 4.1.1.

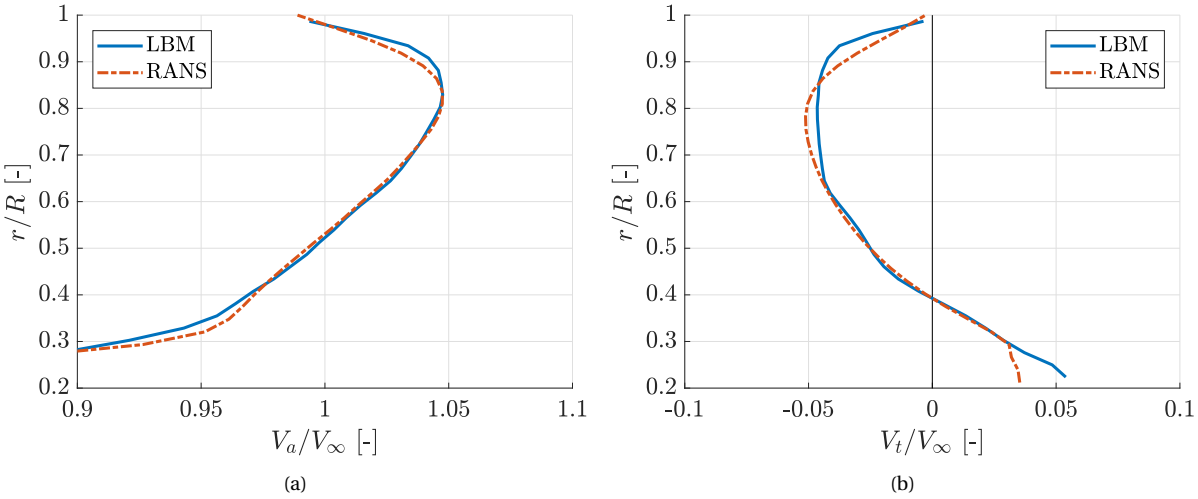

Figure A.8: Time- and spatially-averaged axial (a) and tangential velocity (b) in a plane $0.4c_r$ behind the wing trailing edge (i.e. $x/D = 0.64$) for results obtained with LBM (200 voxels/c_r) and RANS. See Figure A.16a for visualisation of the plane's location.

To inspect the grid independence of the wing's resultant force, the lift and drag coefficient of the wing are defined as:

$$C_L = \frac{F_L}{\frac{1}{2}\rho V_\infty^2 S} \qquad C_D = \frac{F_D}{\frac{1}{2}\rho V_\infty^2 S} \tag{A.1}$$

where F_L and F_D are the lift and drag of the wing, respectively. ρ is the air density, V_∞ the free-stream velocity and S the surface area of the wing. The time-averaged C_L and C_D are presented in Figure A.9 for the three resolution cases. The C_L value is converging towards the value obtained by RANS with a difference of 1.4% in lift when comparing the fine resolution LBM to RANS. The C_D value obtained with LBM is fairly constant with a difference of 0.7% between the value obtained with the grid of 100 and 200 voxels/c_r. It can therefore be concluded that the wing force is more independent of the grid resolution than the SRV force at these resolutions and with the adopted VR strategy.

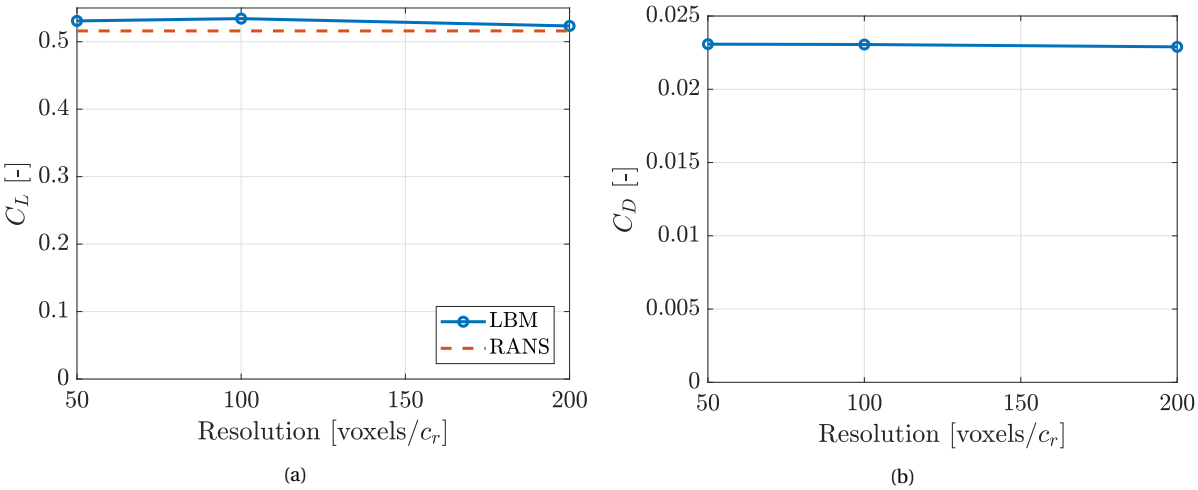

Figure A.9: Averaged lift (a) and drag (b) coefficient of the wing obtained using grids with increasing resolution. The value obtained with RANS is included in (a).

Finally, the grid independence of the aeroacoustic results is demonstrated in Figure A.10 by displaying the polar plot of the overall sound pressure level (OSPL) in Figure A.10a and the OSPL value at $\theta = 90°$ in Figure A.10b for the three grid resolution cases. A converging trend is obtained with grid independence reached at $\theta = 90°$. The maximum difference in OSPL between 100 and 200 voxels/c_r is 2.3 dB at $\theta = 185°$, such that it can be concluded that the OSPL is not completely converged at every angular location.

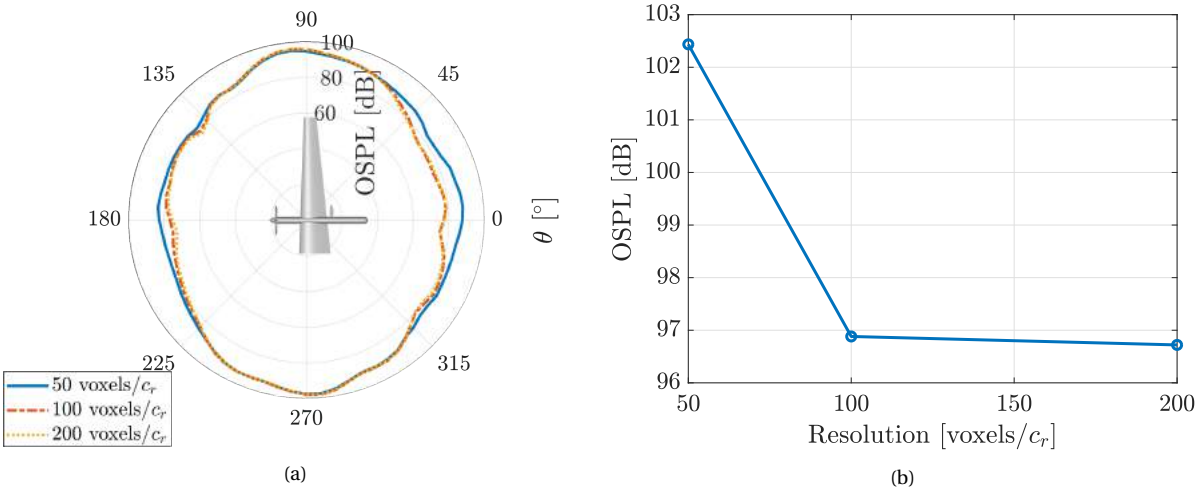

Figure A.10: Polar plot of the overall sound pressure level (OSPL) at a distance of 10D from the wing quarter chord point on the propeller axis in (a) and the OSPL at $\theta = 90°$ in (b). Obtained using grids with increasing resolution.

A.3. Aerodynamic results

Starting of with a general description of the flow, the time-averaged axial velocity is shown in two planes in Figure A.11. The location of the two planes is visualised in Figure A.11c. A high velocity area is present over the top side of the wing, see Figure A.11a. The low pressure on the suction side of the wing causes an region of low

pressure, and low density as a consequence. Together with the slipstream radius, the axial velocity is therefore increased to sustain the mass flow of air over the wing. As expected from the results of the configuration with no wing, the propeller slipstream contracts in front of the wing, visible in Figure A.11b. This contracting trend is however disturbed by the presence of the wing, as concluded from the slipstream shape at the top side of the wing in Figure A.11a. Directly in front and behind the wing, the axial velocity is low, see Figure A.11b. The stagnation point of the wing is the cause of this effect at the leading edge. The low axial velocity at the wing's trailing edge can be explained by the friction over the surface of the wing which decelerates the flow. Finally, the axial velocity is increased by the SRV (see Figure A.11b). As explained in Section 5.1.4, SRVs recover the swirling motion by transforming tangential velocity into axial velocity, thereby increasing the axial velocity. Additional thrust is produced in this process, which is seen to be the case here, as can be concluded from the positive SRV thrust (Figure A.6).

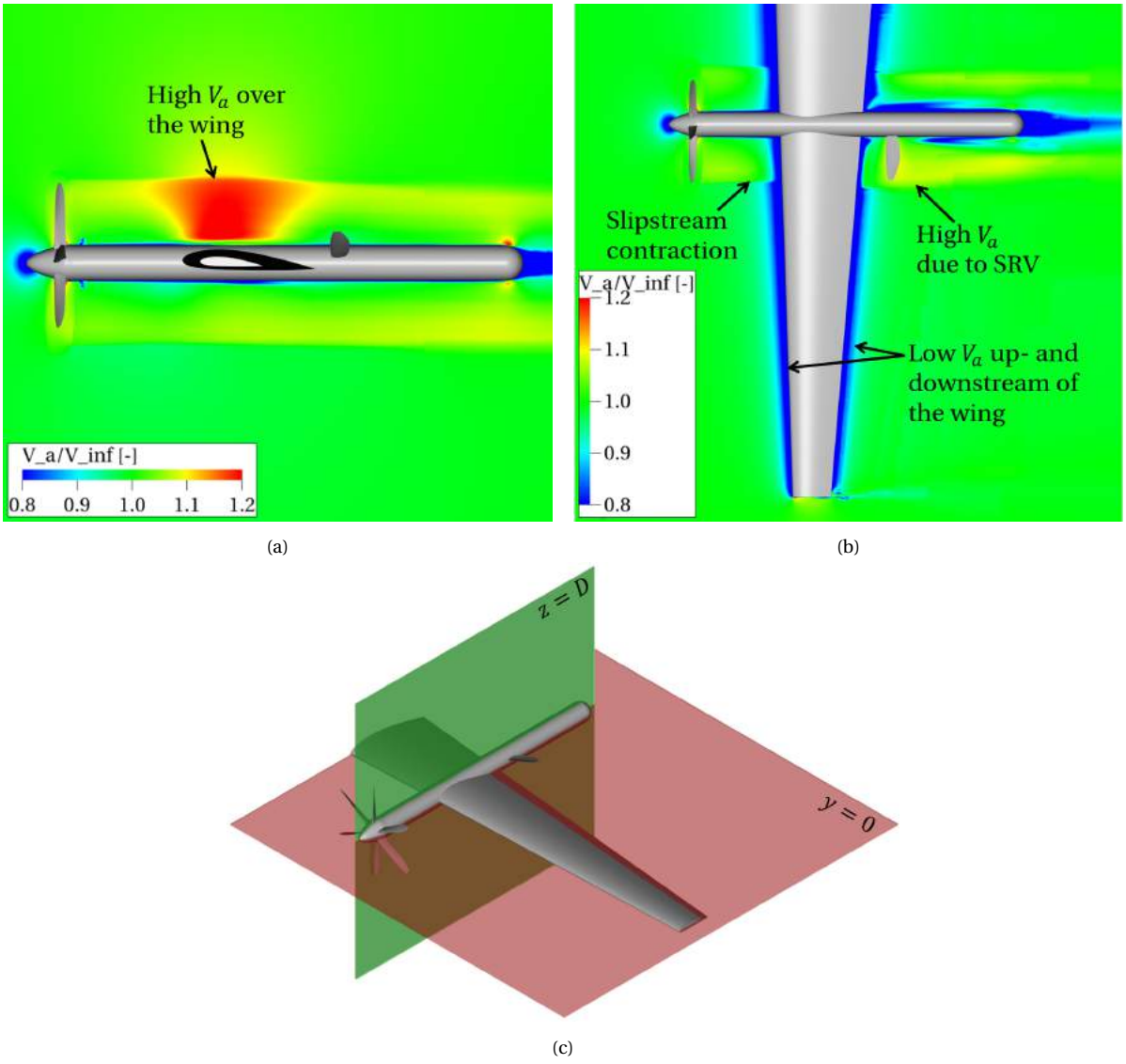

Figure A.11: Time-averaged normalised axial velocity in a plane containing the propeller axis at $z = D$ (a) and a plane containing the wing at $y = 0$ (b). Visualisation of the $z = D$ (green) and $y = 0$ (red) planes in (c).

To inspect the wing performance, the lift and drag distribution over the wing are displayed in Figure A.12. The lift distribution obtained from RANS is included for comparison. 5047 segments are placed along the wing on which the lift and drag coefficients are calculated to obtain the distributions. The location of the propeller and its fairing and axis are indicated in Figure A.12 by solid, dashed and dash-dotted black lines, respectively. The results obtained with the coarse, medium and fine grid are displayed. In agreement with

Figure A.9a, the lift distribution converges towards the value obtained with RANS. The lift is overpredicted in the propeller slipstream due to an insufficiently fine grid as was also concluded from Figure A.7. The drag distributions in Figure A.12b overlap such that it can be concluded that the grid is refined enough to predict the drag, as was done from Figure A.9b.

Behind the upgoing blade (inboard of the fairing), a higher lift and lower drag are obtained. This can be explained by an increased inflow angle $\Delta\varphi$ due to the slipstream swirl which contains an upward tangential velocity V_t behind the upgoing blade, as visualised in green in Figure A.13. This increased effective angle of attack causes the resultant force F_R to increase in size and to tilt forward, reducing the induced drag at that location [51]. The opposite is true behind the downgoing blade where V_t is directed downwards and the resultant force is titled backwards and decreased in magnitude, as shown in red in Figure A.13.

In the region where the fairing is present, no lift and drag are created. This can be explained by the shape of the fairing, which is not integrated with the wing, see Figure A.1. It is therefore a simple cylinder at zero angle of attack, which generates no lift and only minimal drag, consiting of friction drag over the sides of the cylinder. Finally, the lift deteriorates close to the wing tip and a peak in drag is obtained, both caused by the presence of the tip vortex.

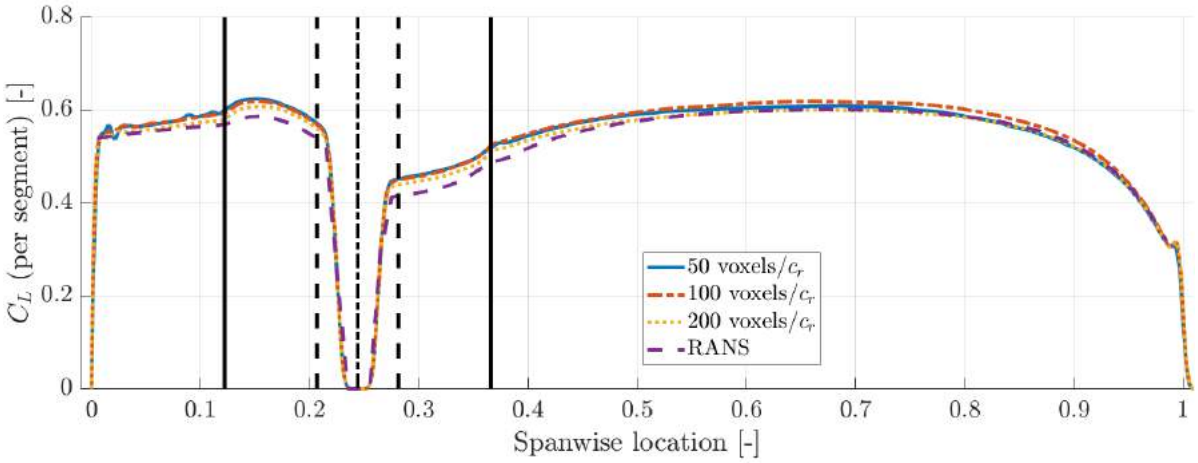

(a)

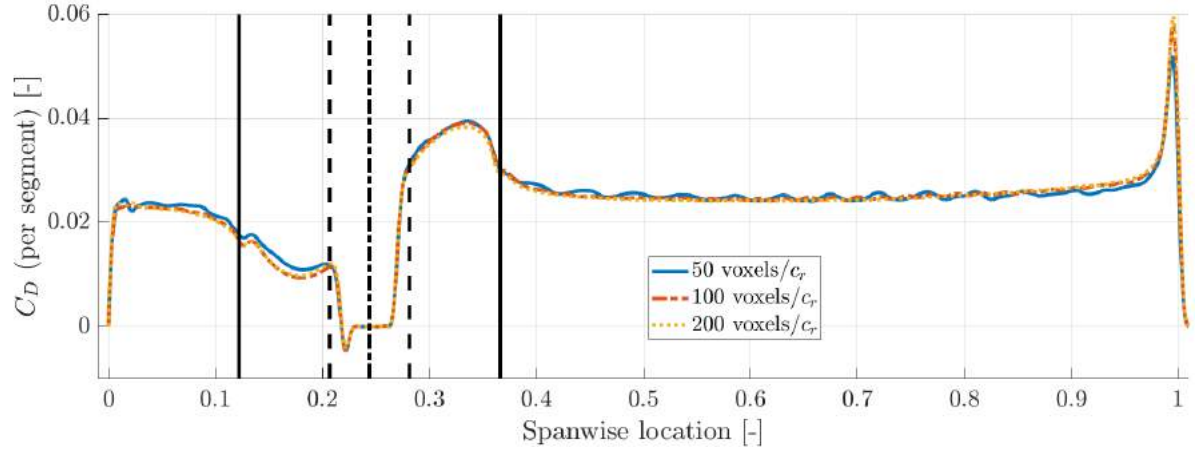

(b)

Figure A.12: Time-averaged lift (a) and drag (b) distribution over the wing obtained using the coarse, medium and fine grid. 5047 segments are used on which the lift and drag coefficient are calculated. The value obtained with RANS is included in (a).

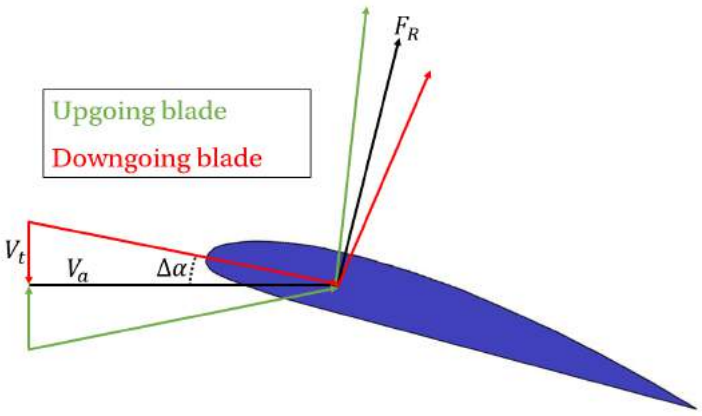

Figure A.13: Cross section of the wing with the effect behind the upgoing and downgoing propeller blades displayed in green and red, respectively.

Shifting focus to the performance of the SRV, the SRV thrust is shown with respect to time in red in Figure A.14a, including the average value. The swirl angle in front of the SRV at $x/D = 0.64$ and $r/R = 0.7$ is shown in blue and relates directly to the SRV inflow angle (Section 2.4). The reader is referred to Figure A.16a for a visualisation of the plane's location. The propeller causes a negative swirl angle as the propeller rotation direction is opposite to the propeller in the geometry without wing. The inflow or swirl angle at $r/R = 0.7$ has a variation of $\varphi = 2.4°$ and a period of $\phi = 60°$ due to the periodic effect of the six propeller blade wakes. Due to the high tangential and low axial velocity in the blade wakes they include a high swirl angle, which causes the negative peaks in swirl angle $r/R = 0.7$ in Figure A.14a. Due to the impingement of the blade wakes, the SRV thrust is observed to fluctuate with a period of $\phi = 60°$. When comparing to the thrust of a vane in the configuration without a wing (Figure 5.4), the fluctuations are seen to be larger in relative magnitude. The maximum thrust is 75% larger than the minimum in Figure A.14a, compared to 33% for the upward vane in the configuration with no wing.

The tip of the SRV is subject to the impingement of the rotor tip vortices (RTVs), as will be confirmed later. The RTVs impinge the SRV at $r/R = 0.965$ for which the swirl angle is shown in blue in Figure A.14b at $x/D = 0.64$. A variation of $\varphi = 9.4°$ is observed, where the large negative peaks are caused by the high negative swirl angle in the RTVs. The smaller peaks are caused by turbulence preceding the RTVs, as will be shown later. The thrust of the SRV tip, defined as 10% of the SRV length, is included in Figure A.14b in red. The tip thrust is seen to have positive peaks due to the impingement of the RTVs, which are aligned with the peaks in thrust of the entire SRV. Although the contribution of the tip is small, it does contribute to the maximum level of vane thrust. The average tip thrust is seen to be negative, but the tip can have a substantial effect on the thrust distribution of the rest of the vane, as was seen in Section 5.3.

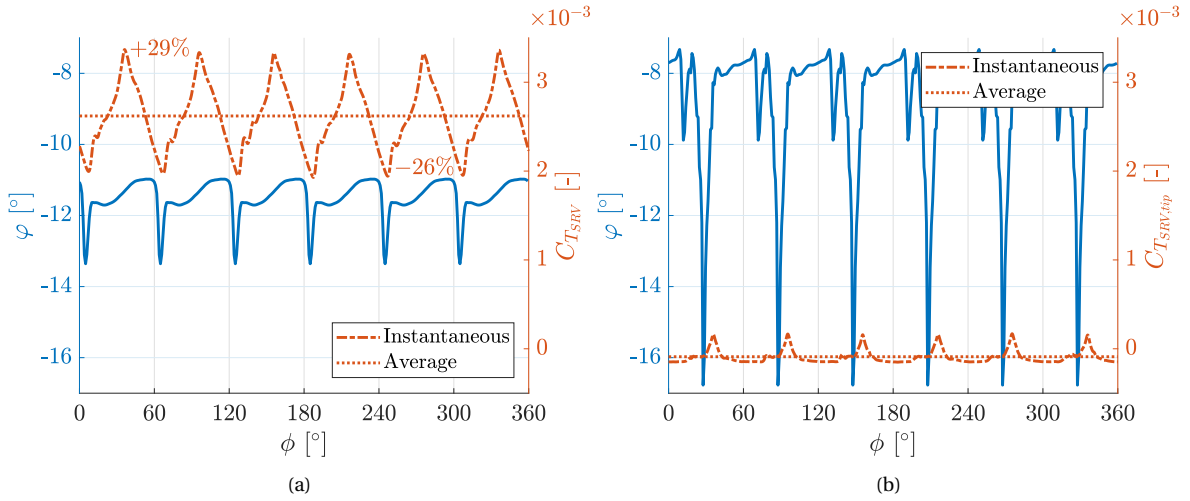

Figure A.14: Swirl angle in blue for $x/D = 0.64$ and $r/R = 0.7$ in (a) and $r/R = 0.965$ in (b). Instantaneous and average SRV thrust in red for the complete SRV in (a) and the SRV tip, defined as 10% of the SRV length, in (b).

To invigorate these observations, the thrust distribution over the vane is displayed in Figure A.15 for various phase angles. The thrust increases from $\phi = 10°$ to $\phi = 29°$ around $r/R = 0.65$ due to the influence of a propeller blade wake. Following, the maximum level of thrust is obtained at $\phi = 39°$ due to the RTV impingement which increases the thrust around $r/R = 0.9$. A region of negative thrust is present for all time steps at the tip of the vane. This confirms that the tip ($r/R > 0.9$) produces negative time-averaged thrust while it does increase the maximum thrust level.

A drag region is also present for $\phi = 20°$ to $\phi = 49°$ in Figure A.15 at the root of the vane. Viscous effects accumulate over the fairing which causes the flow at the root region to deviate from the flow as predicted by lifting line theory, which is used to design the SRV. When these effects are included in the design, an improved performance might be attainable.

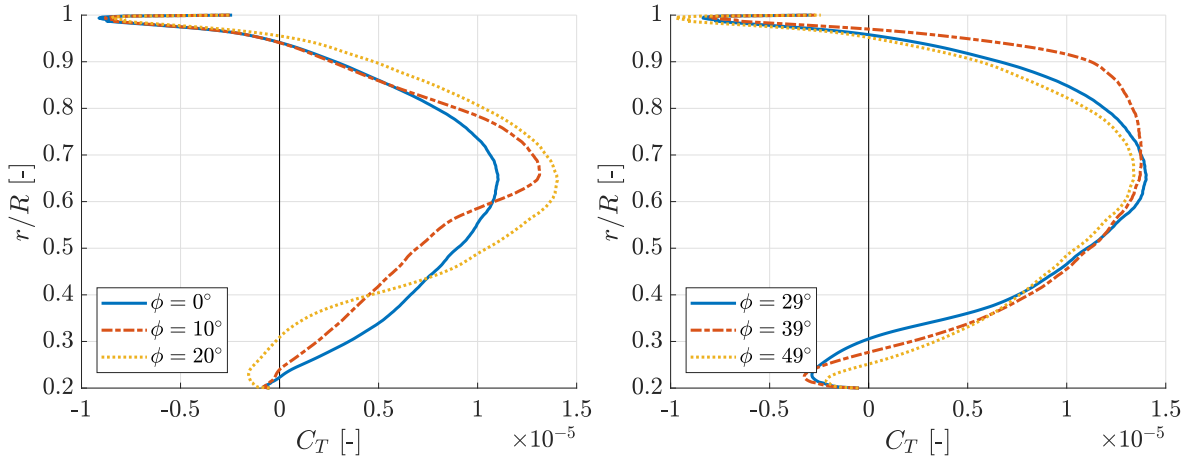

Figure A.15: Phase-averaged thrust distribution over the SRV for various phase angles expressed as C_T per segment (376 segments are used).

To study the SRV inflow fluctuations further, the phase-averaged swirl angle is depicted in various planes for a certain time instant in Figure A.16. The planes used in Figure A.16b, c and d are displayed in Figure A.16a. The periodic regions of negative swirl observed are caused by the propeller blade wakes and the RTVs, as seen in Section 5.1.2. These phenomena are denoted in Figure A.16 and become less distinct when moving downstream.

Due to the upwash in front of the wing, the swirl is strengthened at the inboard side and reduced at the outboard side of the fairing, see Figure A.16a and A.16b. Behind the wing, the downwash causes the swirl to have an opposing direction at the in- and outboard side behind the wing, see Figure A.16a and A.16c. The SRV is located in the region which is strongly influenced by the wing downwash. An area of high swirl is present behind the SRV in Figure A.16d due to its downwash.

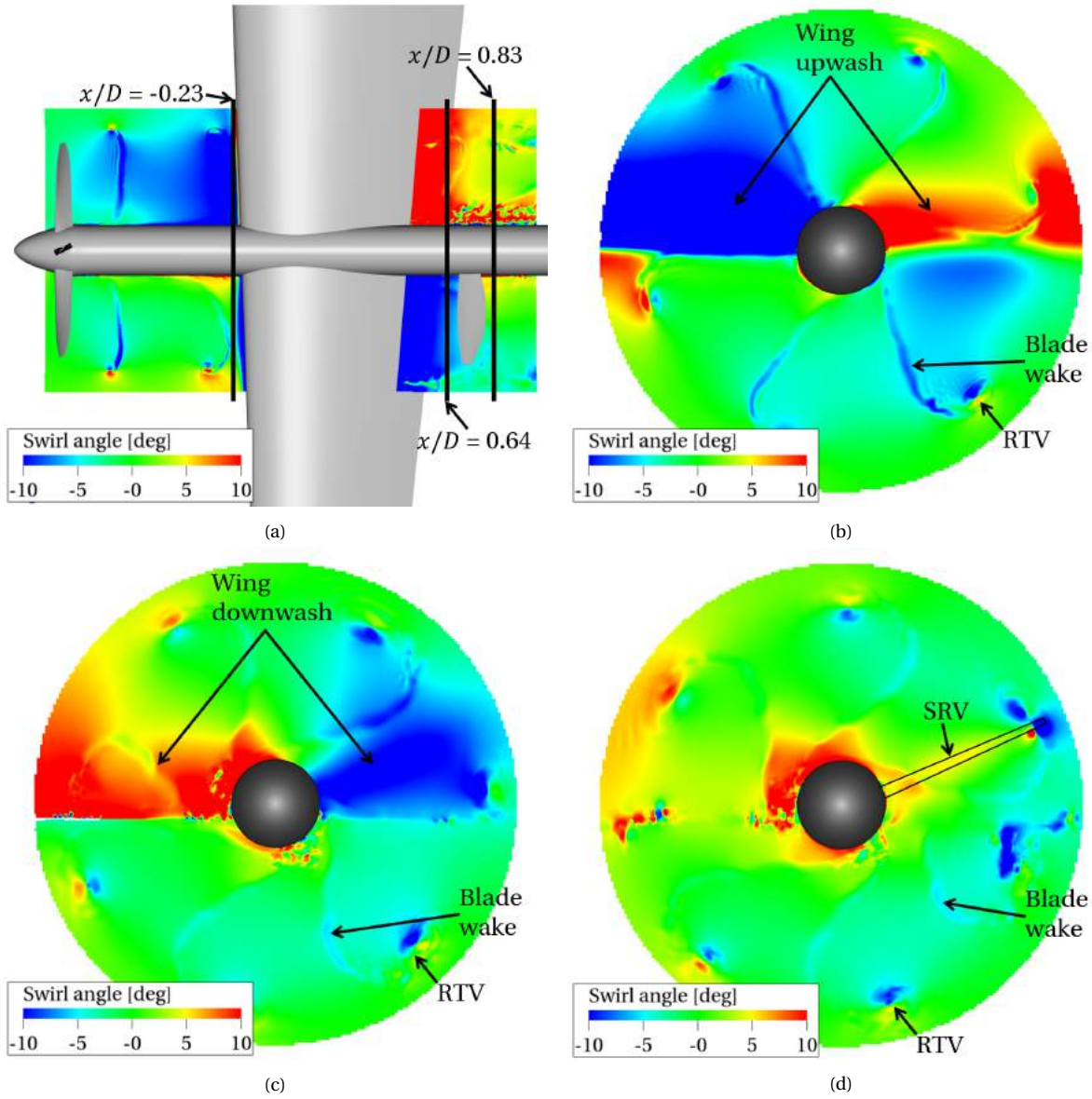

Figure A.16: Phase-averaged swirl angle in $y = 0$ in (a), upstream of the wing ($x/D = -0.23$) in (b), downstream of the wing ($x/D = 0.64$) in (c) and downstream of the SRV ($x/D = 0.83$) in (d). (b), (c) an (d) are obtained by looking into downstream direction and the three planes are indicated in (a).

The radial distributions of swirl in the same three planes as used before are presented in Figure A.17 to quantify the swirl angles. The complete slipstream is averaged to obtain Figure A.17a, whereas half of the slipstream is used to obtain Figure A.17b and A.17c. Figure A.17b averages the swirl behind the upgoing blade (inboard) and Figure A.17c behind the downgoing blade (outboard). It can be seen in Figure A.17a that the wing causes a swirl reduction such that the swirl direction is inverted for $r/R < 0.4$. The SRV causes this area to increase to $r/R < 0.6$.

It can be concluded from the swirl distribution at $x/D = -0.23$ in Figure A.17b that the swirl magnitude is increased in front of the wing at the upgoing blade side due to the wing upwash acting in the same direction as the propeller swirl. The wing seems to have a large swirl-reducing capability behind the upgoing propeller blades as a consequence of the downwash behind the wing acting against the swirl, reducing the swirl magnitude at $x/D = 0.64$ in Figure A.17b. The SRV has minimal effect since it is positioned behind the downgoing blade.

The swirl magnitude is decreased in front of the wing at the downgoing blade side as the upwash acts against the swirl, resulting in a moderate swirl at $x/D = -0.23$ in Figure A.17c. The wing therefore has a swirl recovering effect before the flow actually hits the wing's surface. Behind the wing, the downwash acts in the

direction of the swirl, therefore increasing the swirl magnitude at $x/D = 0.64$ in Figure A.17c. This explains the positioning of the SRV, which decreases the swirl effectively for $r/R > 0.5$ and even inverts the swirl direction at the root.

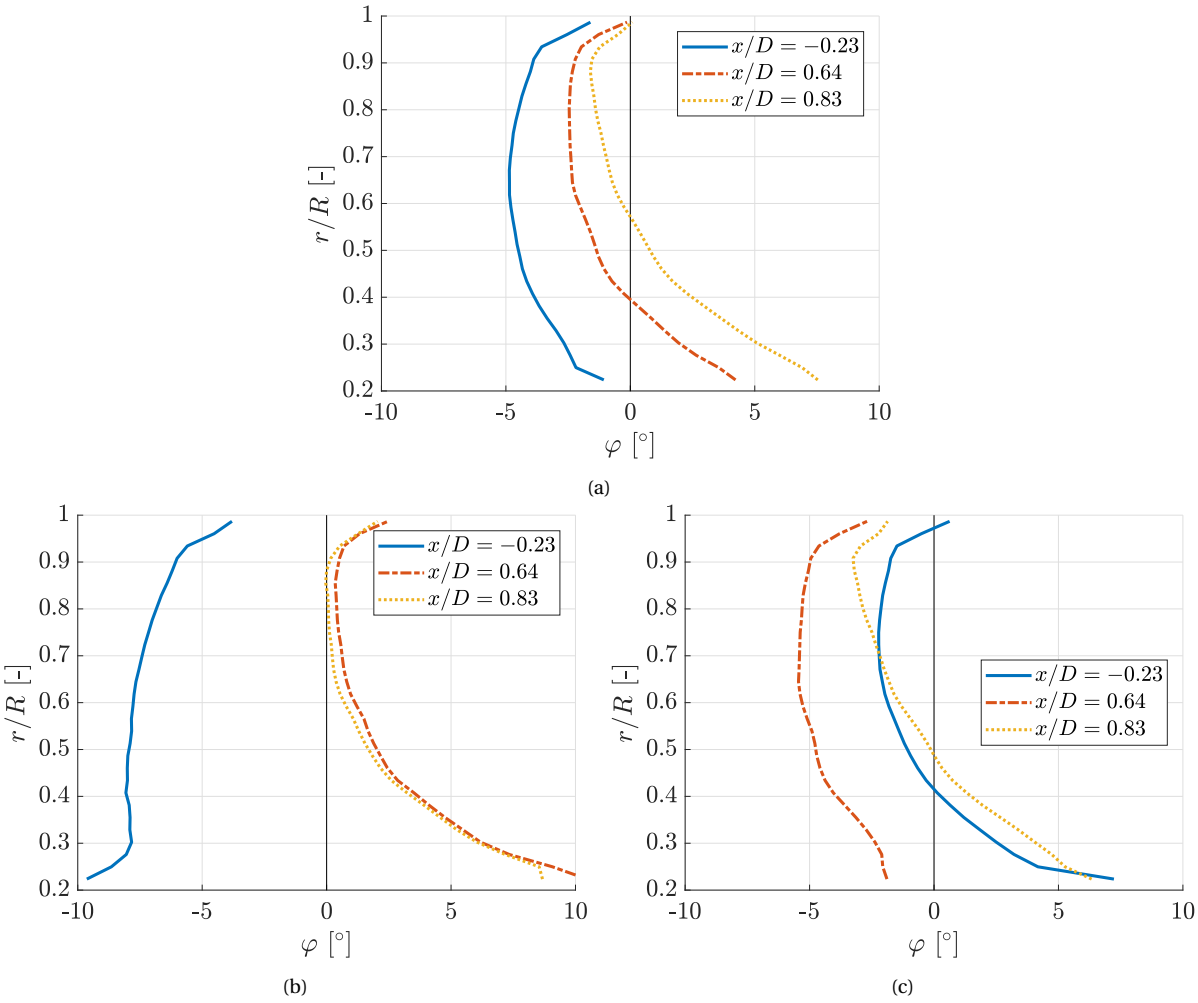

Figure A.17: Time- and spatially-averaged (into 30 intervals) swirl angle φ at three planes. The complete slipstream is averaged in (a), half of the slipstream behind the upgoing blade (inboard) is averaged in (b) and half of the slipstream behind the downgoing blade (outboard) is averaged in (c).

To conclude on the topic of swirl angle, a summarising picture is shown in Figure A.18, where the axial swirl angle development is plotted. The three resolution cases and an aligned image of the geometry are included. The results are shown to be grid independent as the lines overlap to a high degree with a maximum difference between 100 and 200 voxels/c_r of $\phi = 0.25°$. The initial drop in swirl occurs further downstream for the 50 voxels/c_r case, which is a result of the volume of revolution to be defined with a clearance of 40 mm rather than 19 mm. This is done in order to avoid errors caused by the boundary rings of the volume of revolution crossing through more than two VR regions. A negative swirl angle of $\phi = -4.0°$ is created by the propeller. The wing recovers 63% of the propeller swirl in a region between the location of the wing leading edge and its quarter chord line. The SRV recovers the remaining swirl such that the swirl recovery of the combination of wing and SRV sums up to 100%. The SRV is therefore concluded to be very effective in recovering swirl.

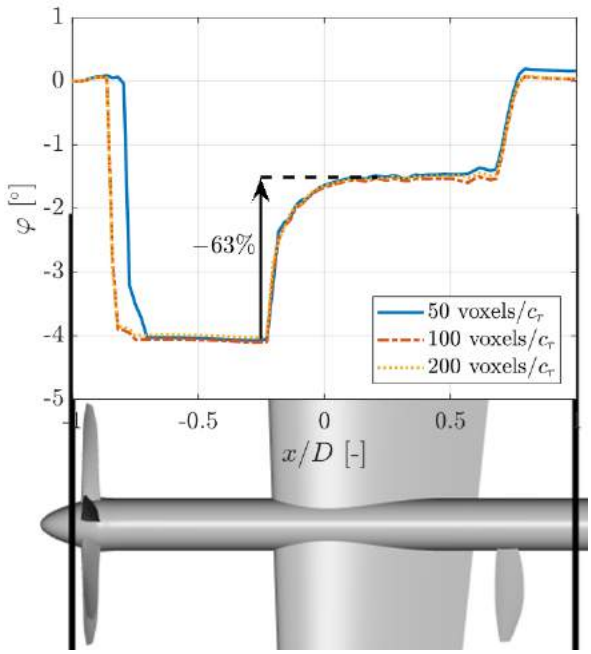

Figure A.18: Development of the average swirl angle for $r/R < 1$. The attached geometry denotes the location.

To get a better feel for the behaviour of the rotor tip vortices (RTVs), λ_2 isosurfaces are presented in Figure A.19. A top view is presented in Figure A.19a and a view of the lower side is shown in Figure A.19b. The RTVs have a spanwise motion over the wing, as was demonstrated by Johnston & Sullivan [28]. This can be explained by mirror vortices, as is done in Section 2.6, in combination with the effect of the wing trailing vortices caused by the wing loading distribution. The spanwise motion is illustrated in Figure A.19 by arrows. Behind the upgoing blade (inboard side), the RTVs have an inboard motion on the upper surface and no spanwise motion on the lower surface, conform the observations made by Johnston & Sullivan which are shown in Figure A.20a. Behind the downgoing blade (outboard side), the RTVs move inboard on the lower surface in agreement with Figure A.20b. However, the RTVs have an outboard motion on the upper surface behind the downgoing blade, which opposes the findings of Johnston & Sullivan [28], for which the reason is unknown. Despite the spanwise motion over the wing, the RTVs are seen to impinge on the tip of the SRV at $r/R = 0.965$. In Figure A.19a the turbulence is denoted which precedes the RTVs as was discussed regarding Figure A.14a.

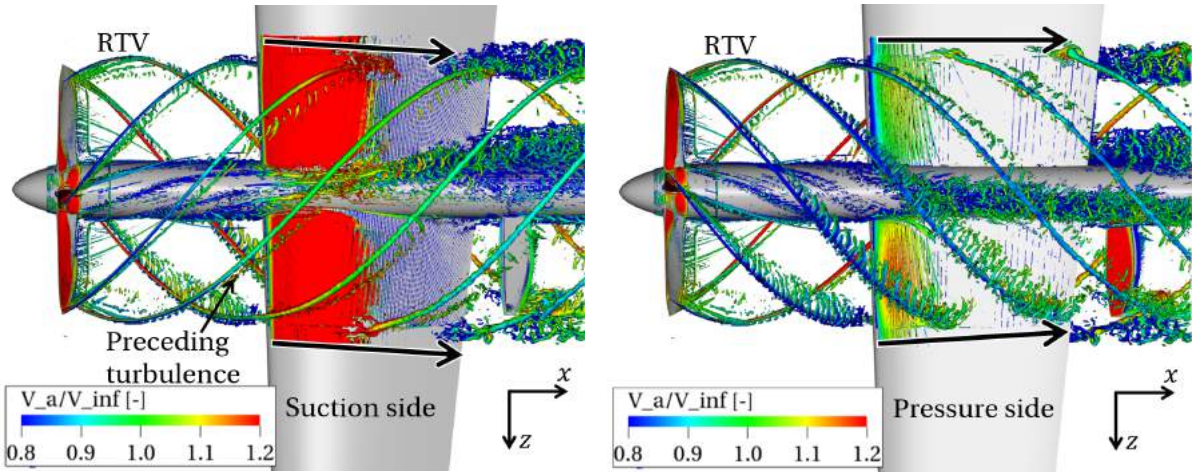

(a) (b)

Figure A.19: Phase-averaged isosurface of $\lambda_2 = -3 \cdot 10^6$ s^{-2} coloured by the normalised axial velocity. Top view in (a) and bottom view in (b). Note that the bottom view has been mirrored. Arrows indicate the direction of motion of the RTVs.

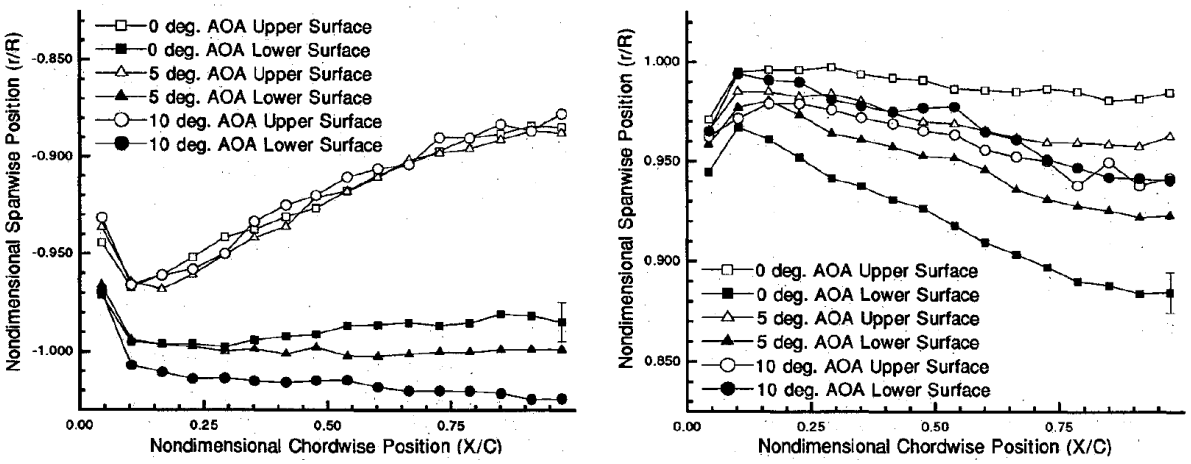

Figure A.20: Upgoing (a) and downgoing (b) blade vortex position at the upper and lower surface of the trailing wing at various angles of attack. Results from Johnston & Sullivan [28].

A.4. Aeroacoustic results

The aeroacoustic results are presented in terms of a far-field analysis around a ring in the $y = 0$-plane of radius $10D$, centred at the crossing between the wing quarter chord line and the propeller axis. The same method is applied as used to obtain the results in Section 5.2.1, which is explained in Section 3.1.4. The overall sound pressure level (OSPL) over the ring is displayed in Figure A.21a, where the contribution of the propeller, wing and SRV are shown separately. A visual of the geometry is included to illustrate the direction of θ. From Figure A.21a the propeller is seen to emit most noise in sideways directions whereas the SRV has a more uniform emission pattern. This agrees with the results obtained from the configuration without wing. The wing shows similar behaviour in Figure A.21a as the SRV which is plausible as both are stationary trailing surfaces. The wing emits substantially less noise in the direction of $\theta = 90°$ and $\theta = 270°$ however. Finally, wing and SRV have no axisymmetric emission pattern, as the configuration is not axisymmetric, such that no power watt level can be calculated.

Pressure band level (PBL) curves in $1/12^{th}$ octave bands are presented in Figure A.21b to A.21f for various locations around the ring used in Figure A.21a. Similar to the case of the configuration with no wing, the propeller emits a large first harmonic at $\theta = 90°$ (Figure A.21b) which diminishes when moving up- and downstream. Apart for $\theta = 90°$, the propeller does not show distinct higher harmonics as was the case for the configuration without wing (Figure 5.18). The broadband level of the propeller contribution is substantially higher. This can be caused by the altered flight conditions as well as by the fluctuating propeller loading due the upstream effect of the wing as shown in Figure A.2.

The wing and SRV emit noise at multiples of the BPF, apart from the wing at $\theta = 90°$ (Figure A.21b). Despite the small relative size of the SRV compared to the wing, the SRV has a similar or larger contribution than the wing, depending on the circumferential location. It is therefore concluded that the SRV is a substantial noise source.

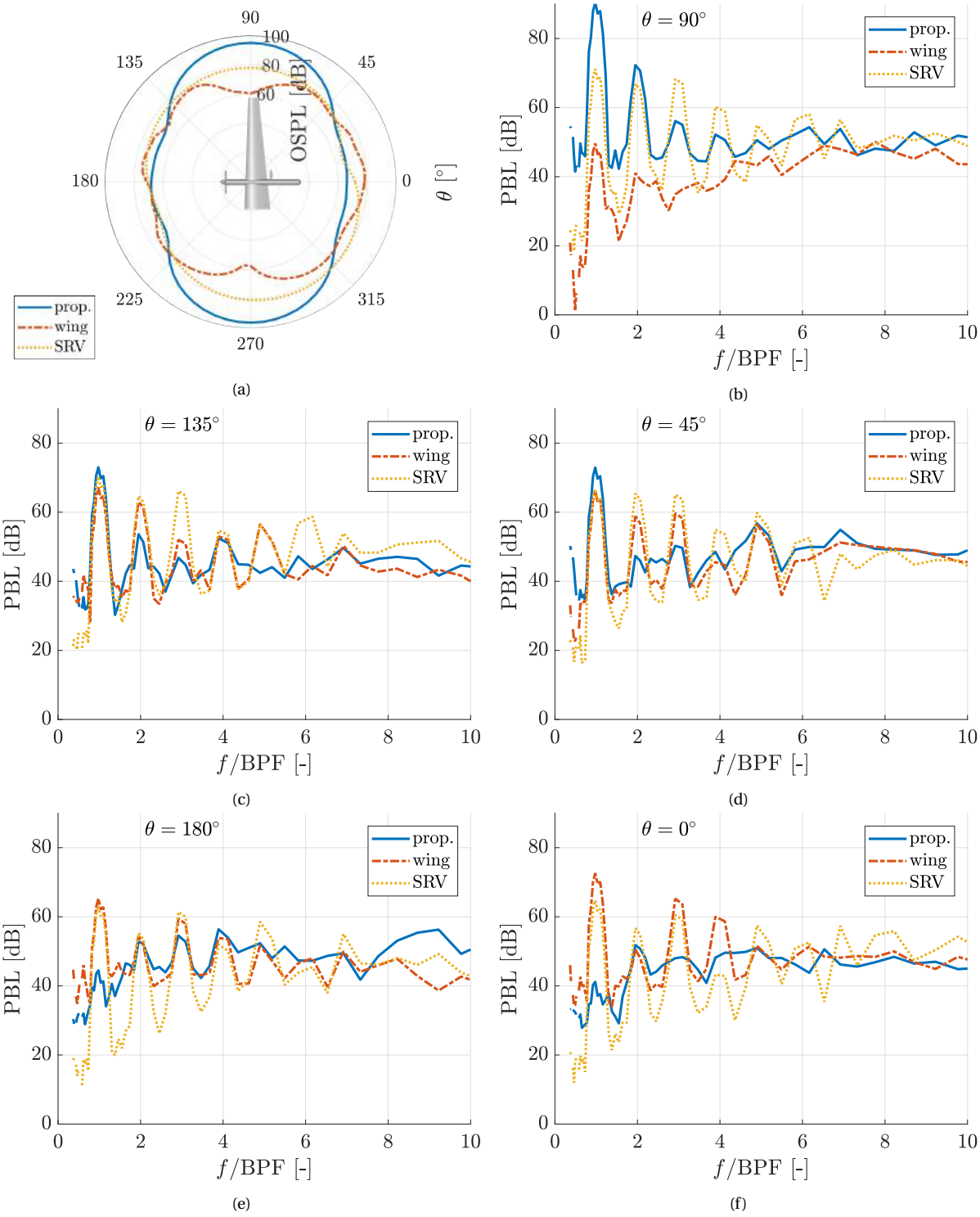

Figure A.21: Polar plot of the overall sound pressure level (OSPL) in (a) and the pressure band level (PBL) in $1/12^{th}$ octave bands at various angles θ in (b) to (f). The contributions of the propeller, wing and SRV at a distance of $10D$ from the wing quarter chord point on the propeller axis are shown.

To investigate the added noise due to the installation of the SRV, a comparison is made in Figure A.22 between the full configuration and the full configuration without the contribution of the SRV. Reductions in OSPL are observed around $\theta = 135°$ and $\theta = 315°$ in Figure A.22a with the largest decrease in OSPL of 7.4 dB at $\theta = 330°$. The higher harmonics are reduced in all directions when removing the SRV, see Figure A.22b to A.22f, such that the SRV can be concluded to increase the perceived noisiness of the sound in all directions.

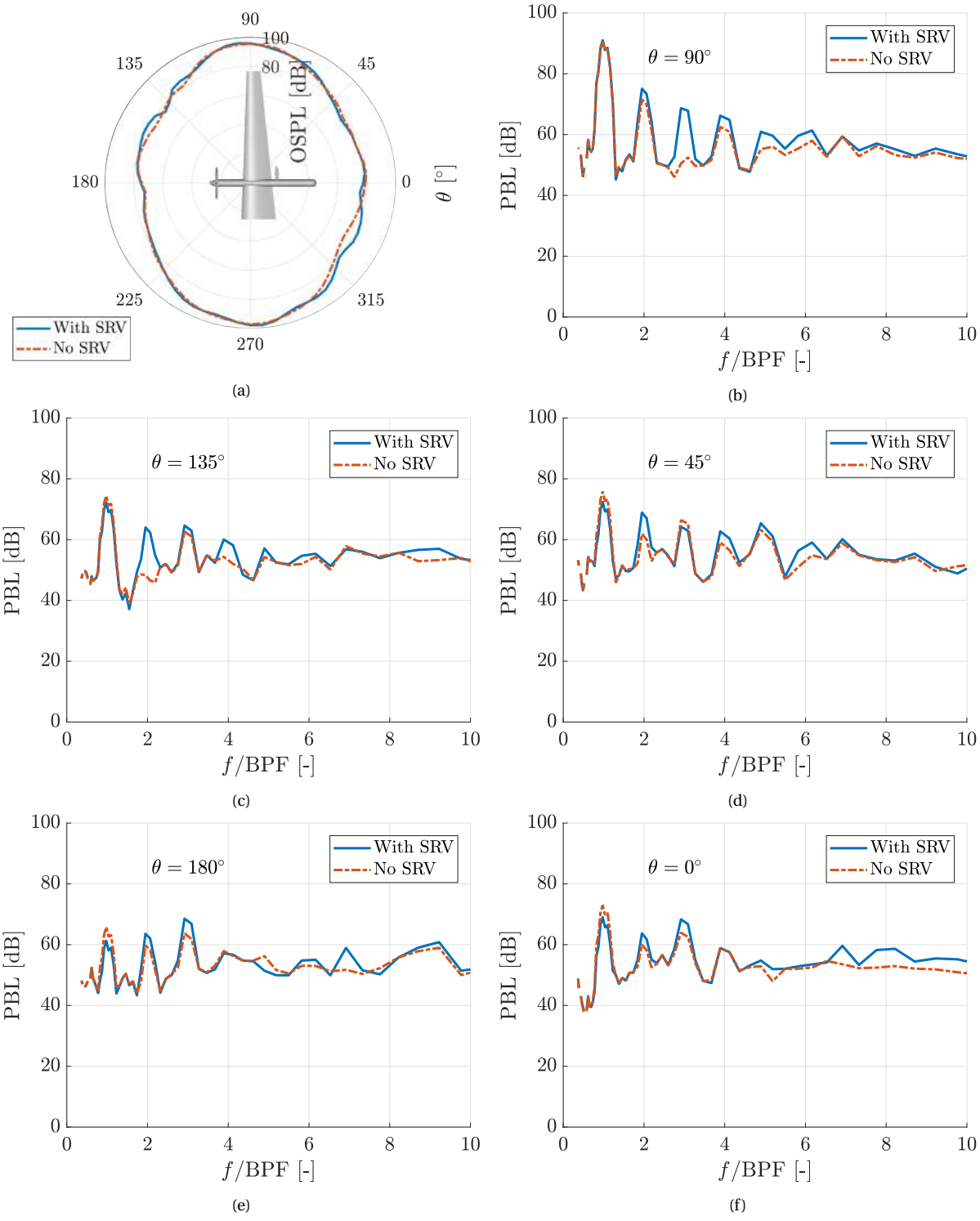

Figure A.22: Polar plot of the overall sound pressure level (OSPL) in (a) and the pressure band level (PBL) in $1/12^{th}$ octave bands at various angles θ in (b) to (f). The contribution of all surfaces (With SRV) and all surfaces apart from the SRV (No SRV) are shown.

Bibliography

[1] AC 36-1H: Noise Levels for U.S. Certificated and Foreign Aircraft. Technical report, Federal Aviation Administration, 2012. URL http://www.faa.gov/regulations_policies/advisory_circulars/.

[2] Airliners.net. IPTN N-250, 2017. URL http://www.airliners.net/aircraft-data/iptn-n-250/257.

[3] J. D. Anderson Jr. *Introduction to Flight*. McGraw-Hill Education, 2012. ISBN 978-007-108605-9.

[4] F. Avallone, W.C.P. van der Velden, D. Ragni, and D. Casalino. Noise reduction mechanisms of sawtooth and combed-sawtooth trailing-edge serrations. *Journal of Fluid Mechanics*, 848:560–591, 2018. URL https://doi.org/10.1017/jfm.2018.377.

[5] M.D. Bowles. The "Apollo" of Aeronautics: NASA's Aircraft Energy Efficiency Program, 1973-1987. Technical report, National Aeronautics and Space Administration, 2010.

[6] J. Brandt and M. Selig. Propeller Performance Data at Low Reynolds Numbers. In *49th AIAA Aerospace Sciences Meeting including the New Horizons Forum and Aerospace Exposition*, Reston, Virigina, 2011. American Institute of Aeronautics and Astronautics. doi: 10.2514/6.2011-1255. URL http://arc.aiaa.org/doi/10.2514/6.2011-1255.

[7] G. Brès, F. Pérot, and D. Freed. A Ffowcs Williams - Hawkings Solver for Lattice-Boltzmann Based Computational Aeroacoustics. In *16th AIAA/CEAS Aeroacoustics Conference*, Reston, Virigina, jun 2010. American Institute of Aeronautics and Astronautics. ISBN 978-1-60086-955-6. doi: 10.2514/6.2010-3711. URL http://arc.aiaa.org/doi/10.2514/6.2010-3711.

[8] G. A. Brès, F. Pérot, and D. Freed. Properties of the lattice-Boltzmann method for acoustics. In *15th AIAA/CEAS Aeroacoustics Conference (30th AIAA Aeroacoustics Conference)*, 2009. doi: https://doi.org/10.2514/6.2009-3395. URL http://arc.aiaa.org/doi/pdf/10.2514/6.2009-3395.

[9] D. Casalino, A. Hazir, and A. Mann. Turbofan Broadband Noise Prediction Using the Lattice Boltzmann Method. *AIAA Journal*, 56(2):609–628, 2018. doi: 10.2514/1.J055674. URL https://arc.aiaa.org/doi/10.2514/1.J055674.

[10] J.J. Cassidy and H.T. Falvey. Observations of unsteady flow arising after vortex breakdown. *Journal of Fluid Mechanics*, 41(4):727–736, 1970. doi: 10.1017/S0022112070000873. URL http://www.journals.cambridge.org/abstract_S0022112070000873.

[11] F. Çelik and M. Güner. Energy saving device of stator for marine propellers. *Ocean Engineering*, 34 (5-6):850–855, 2007. doi: 10.1016/j.oceaneng.2006.03.016. URL http://linkinghub.elsevier.com/retrieve/pii/S0029801806001600.

[12] H. Chen, S.A Orszag, I. Staroselsky, and S. Succi. Expanded analogy between Boltzmann kinetic theory of fluids and turbulence. *Journal of Fluid Mechanics*, 519:301–314, nov 2004. doi: 10.1017/S0022112004001211. URL http://www.journals.cambridge.org/abstract_S0022112004001211.

[13] S. Chen and G.D. Doolen. Lattice Boltzmann Method for Fluid Flows. *Annual Review of Fluid Mechanics*, 30(1):329–364, 1998. doi: 10.1146/annurev.fluid.30.1.329. URL http://annualreviews.org/doi/pdf/10.1146/annurev.fluid.30.1.329.

[14] W.B. Coney. *A Method for the Design of a Class of Optimum Marine Propulsors*. PhD thesis, Massachusetts Institute of Technology, 1989. URL https://dspace.mit.edu/bitstream/handle/1721.1/14207/22269941-MIT.pdf?sequence=2.

[15] N. Curle. The influence of solid boundaries upon aerodynamics sound. *Proceedings of the Royal Society of London. Series A, Mathematical and Physical Sciences*, 231(1187):505–514, 1955. URL http://www.jstor.org/stable/99804.

[16] A.F. Deming. Propeller Rotation Noise Due to Torque and Thrust. *The Journal of the Acoustical Society of America*, 12(1):173–182, 1940. doi: 10.1121/1.1916089. URL http://asa.scitation.org/doi/10.1121/1.1916089.

[17] R.W. Deters, G.K. Ananda, and M.S. Selig. Reynolds Number Effects on the Performance of Small-Scale Propellers. In *32nd AIAA Applied Aerodynamics Conference*, pages 1–43, Reston, Virginia, 2014. American Institute of Aeronautics and Astronautics. doi: 10.2514/6.2014-2151. URL http://arc.aiaa.org/doi/10.2514/6.2014-2151.

[18] J.H. Dittmar and G.H. Hall. The Effect of Swirl Recovery Vanes on the Cruise Noise of an Advanced Propeller. In *13th Aeroacoustics Conference*, Reston, Virigina, 1990. American Institute of Aeronautics and Astronautics. doi: 10.2514/6.1990-3932. URL http://arc.aiaa.org/doi/10.2514/6.1990-3932.

[19] M. Drela. XFOIL: An Analysis and Design System for Low Reynolds Number Airfoils. In *Low Reynolds Number Aerodynamics*, pages 1–12. Springer-Verlag, 1989. URL http://web.mit.edu/drela/Public/papers/xfoil_sv.pdf.

[20] B. Epps, J. Chalfant, R. Kimball, A. Techet, K. Flood, and C. Chryssostomidis. OpenProp: An Open-source Parametric Design and Analysis Tool for Propellers. In *Proceedings of the 2009 grand challenges in modeling & simulation conference*, pages 104–111, 2009.

[21] Exa. The Technology Behind PowerFLOW: Exa's Lattice Boltzmann-based Physics, 2018. URL http://exa.com/en/company/exa-lattice-boltzmann-technology.

[22] J.A. Gazzaniga and G.E. Rose. Wind Tunnel Performance Results of Swiri Recovery Vanes as Tested with an Advanced High Speed Propeller. In *28th Joint Propulsion Conference and Exhibit*, Reston, Virigina, 1992. American Institute of Aeronautics and Astronautics. doi: 10.2514/6.1992-3770. URL http://arc.aiaa.org/doi/10.2514/6.1992-3770.

[23] J.F. Groeneweg and L.J. Bober. NASA Advanced Propeller Research. In *Advanced Propellers and Their Installation on Aircraft*, 1988.

[24] D.B. Hanson. Sound from a Propeller at Angle of Attack: A New Theoretical Viewpoint. *Proceedings of the Royal Society of London Series A - Mathematical and Physical Sciences*, 449(1936):315–328, 1995. URL https://www.jstor.org/stable/pdf/52699.pdf.

[25] S. Hickel. AE4202 CFD for Aerospace Engineers Lecture 6: LES, 2016.

[26] J. Jeong and F. Hussain. On the identification of a vortex. *Journal of Fluid Mechanics*, 285(1):69–94, 1995. doi: 10.1017/S0022112095000462. URL http://www.journals.cambridge.org/abstract_S0022112095000462.

[27] R.T. Johnston and J.P. Sullivan. Propeller Tip Vortex Interactions. In *28th Aerospace Sciences Meeting*, Reston, Virigina, 1990. American Institute of Aeronautics and Astronautics. doi: 10.2514/6.1990-437. URL http://arc.aiaa.org/doi/10.2514/6.1990-437.

[28] R.T. Johnston and J.P. Sullivan. Unsteady Wing Surface Pressures in the Wake of a Propeller. *Journal of aircraft*, 30(5):644–651, 1993.

[29] T. Kajishima and K. Taira. Reynolds-Averaged Navier–Stokes Equations. In *Computational Fluid Dynamics*, pages 237–268. Springer International Publishing, 2017. ISBN 978-3-319-45302-6. URL http://link.springer.com/10.1007/978-3-319-45304-0_7.

[30] T. Krüger, H. Kusumaatmaja, A. Kuzmin, O. Shardt, G. Silva, and E.M. Viggen. *The Lattice Boltzmann Method*. Graduate Texts in Physics. Springer International Publishing, 2017. ISBN 978-3-319-44647-9. URL http://link.springer.com/10.1007/978-3-319-44649-3.

[31] K.D. Kryter. The Meaning and Measurement of Perceived Noise Level. *Noise Control*, 6(5):12–27, 1960. ISSN 0549-5865. doi: 10.1121/1.2369423. URL https://doi.org/10.1121/1.2369423.

[32] Q. Li, Y. Wang, and G. Eitelberg. An investigation of tip vortices unsteady interaction for Fokker 29 propeller with swirl recovery vane. *Chinese Journal of Aeronautics*, 29(1):117–128, 2016. doi: 10.1016/j.cja.2015.12.004. URL https://doi.org/10.1016/j.cja.2015.12.004.

[33] Q. Li, K. Öztürk, T. Sinnige, D. Ragni, Y. Wang, G. Eitelberg, and L.L.M. Veldhuis. Design and Experimental Validation of Swirl Recovery Vanes for Propeller Propulsion Systems. In *35th AIAA Applied Aerodynamics Conference*, Denver, Colorado, 2017. American Institute of Aeronautics and Astronautics. doi: 10.2514/6.2017-3571. URL https://arc.aiaa.org/doi/pdf/10.2514/6.2017-3571.

[34] L.E.M. Lignarolo, D. Ragni, C. Krishnaswami, Q. Chen, C.J. Simão Ferreira, and G.J.W. van Bussel. Experimental analysis of the wake of a horizontal-axis wind-turbine model. *Renewable Energy*, 70:31–46, 2014. ISSN 481. doi: 10.1016/j.renene.2014.01.020. URL https://doi.org/10.1016/j.renene.2014.01.020.

[35] D.P. Lockard, L.-S. Luo, S.D. Milder, and B.A. Singer. Evaluation of PowerFLOW for Aerodynamic Applications. *Journal of Statistical Physics*, 107(1/2):423–478, 2002. doi: 10.1023/A:1014539411062. URL http://link.springer.com/10.1023/A:1014539411062.

[36] B. Magliozzi, D.B. Hanson, and R.K. Amit. Propeller and Propfan Noise. In *Aeroacoustics of Flight Vehicles: Theory and Practice*, volume 1, pages 1–64. National Aeronautics and Space Administration, 1991.

[37] J.E. Marte and D.W. Kurtz. A Review of Aerodynamic Noise From Propellers, Rotors, and Lift Fans. Technical report, NASA, 1970. URL https://ntrs.nasa.gov/archive/nasa/casi.ntrs.nasa.gov/19700005920.pdf.

[38] B.W. McCormick. *Aerodynamics, Aeronautics, and Flight Mechanics*. John Wiley & Sons, New York, NY, 1979. ISBN 0-471-03032-5.

[39] W.J. McCroskey. The Phenomenon of Dynamic Stall. Technical report, National Aeronautics and Space Administration, Moffett Field, California, 1981. URL http://www.dtic.mil/dtic/tr/fulltext/u2/a098191.pdf.

[40] D.C. Mikkelson, G.A. Mitchell, and L.J. Bober. Summary of Recent NASA Propeller Research. Technical report, National Aeronautics and Space Administration, 1984. URL https://ntrs.nasa.gov/search.jsp?R=19840024274.

[41] R. Nahuis and T. Sinnige. Design, manufacture and commissioning of a new NLR six-component rotating shaft balance for Delft University of Technology. In *10th International Symposium on Strain-Gauge Balances*, Mianyang, China, 2016.

[42] F. Pérot, M.-S. Kim, S. Moreau, M. Henner, and D. Neal. Direct aeroacoustics predictions of a low speed axial fan. In *16th AIAA/CEAS Aeroacoustics Conference*, Reston, Virigina, 2010. American Institute of Aeronautics and Astronautics. doi: 10.2514/6.2010-3887. URL http://arc.aiaa.org/doi/10.2514/6.2010-3887.

[43] S.B. Pope. *Turbulent Flows*. Cambridge University Press, Cambridge ; New York, 2000. ISBN 0521591252.

[44] A.K. Prasad. Particle Image Velocimetry. *Current Science*, 79(1):51–60, 2000.

[45] J. Ramon. No Title, 2018. URL http://www.airliners.net/photos/airliners/7/0/4/2285407.jpg.

[46] E.W.M. Roosenboom, A. Heider, and A. Schröder. Investigation of the Propeller Slipstream with Particle Image Velocimetry. *Journal of Aircraft*, 46(2):442–449, 2009. doi: 10.2514/1.33917. URL http://arc.aiaa.org/doi/10.2514/1.33917.

[47] F. Russo and N.T. Basse. Scaling of turbulence intensity for low-speed flow in smooth pipes. *Flow Measurement and Instrumentation*, 52:101–114, 2016. doi: 10.1016/j.flowmeasinst.2016.09.012. URL http://linkinghub.elsevier.com/retrieve/pii/S095559861630173X.

[48] D.G. Simons. Lecture AE4445: Introduction to Aircraft Noise, 2016.

[49] T. Sinnige, J.J. van Kuijk, K.P. Lynch, D. Ragni, G. Eitelberg, and L.L.M. Veldhuis. The Effects of Swirl Recovery Vanes on Single-Rotation Propeller Aerodynamics and Aeroacoustics. In *21st AIAA/CEAS Aeroacoustics Conference*, Reston, Virginia, 2015. American Institute of Aeronautics and Astronautics. doi: 10.2514/6.2015-2358. URL http://arc.aiaa.org/doi/10.2514/6.2015-2358.

[50] T.C.A. Stokkermans. *Design and Analysis of Swirl Recovery Vanes for an Isolated and a Wing Mounted Tractor Propeller*. PhD thesis, Delft University of Technology, 2015.

[51] L.L.M. Veldhuis. *Propeller Wing Aerodynamic Interference*. PhD thesis, Delft University of Technology, 2005. URL https://repository.tudelft.nl/islandora/object/uuid:8ffbde9c-b483-40de-90e0-97095202fbe3/datastream/OBJhttp://www.narcis.nl/publication/RecordID/oai:tudelft.nl:uuid:8ffbde9c-b483-40de-90e0-97095202fbe3.

[52] T. von Kármán. Mechanische Ähnlichkeit und Turbulenz. *Nachrichten von der Gesellschaft der Wissenschaften zu Göttingen, Fachgruppe 1 (Mathematik)*, 5:58–76, 1930.

[53] Y. Wang, Q. Li, G. Eitelberg, L.L.M. Veldhuis, and M. Kotsonis. Design and numerical investigation of swirl recovery vanes for the Fokker 29 propeller. *Chinese Journal of Aeronautics*, 27(5):1128–1136, 2014. doi: 10.1016/j.cja.2014.03.009.

[54] Y. Wang, N. Chen, Q. Li, and G. Eitelberg. An Optimization of Swirl Recovery Vane for Fokker 29 Propeller Using Design of Experiment Method. In *ASME Turbo Expo 2016: Turbomachinery Technical Conference and Exposition*, 2016. doi: 10.1115/GT2016-57691. URL http://proceedings.asmedigitalcollection.asme.org/proceeding.aspx?doi=10.1115/GT2016-57691.

[55] P. Welch. The Use of Fast Fourier Transform for the Estimation of Power Spectra: A Method Based on Time Averaging Over Short, Modified Periodograms. *IEEE Transactions on audio and electroacoustics*, 15 (2):70–73, 1967.

[56] V. Yakhot and S.A. Orszag. Renormalization group analysis of turbulence. I. Basic theory. *Journal of Scientific Computing*, 1(1):3–51, 1986. doi: 10.1007/BF01061452. URL http://link.springer.com/10.1007/BF01061452.